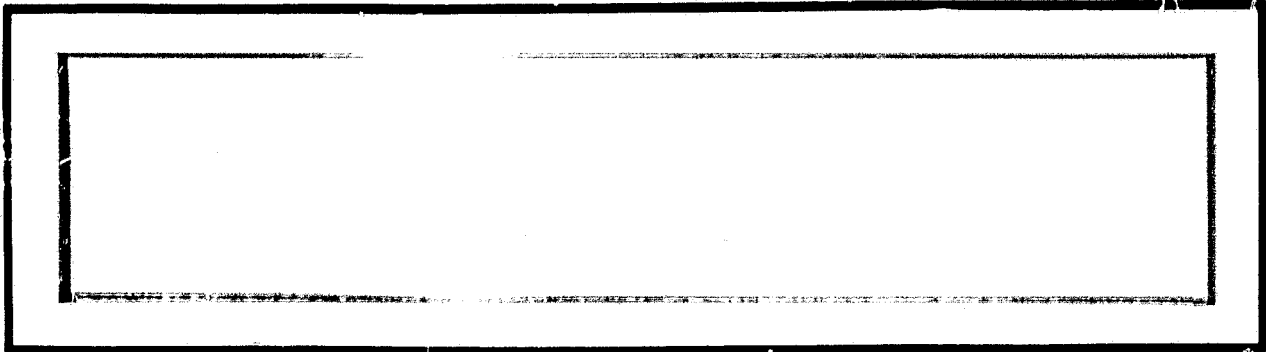# N O T I C E

THIS DOCUMENT HAS BEEN REPRODUCED FROM MICROFICHE. ALTHOUGH IT IS RECOGNIZED THAT CERTAIN PORTIONS ARE ILLEGIBLE, IT IS BEING RELEASED IN THE INTEREST OF MAKING AVAILABLE AS MUCH INFORMATION AS POSSIBLE

(NASA-CR-167394)   SOLAR POWER SATELLITE
ANTENNA PHASE CONTROL SYSTEM HARDWARE   HC A05/MF A01   N81-33613
SIMULATION, PHASE 4.   VOLUME 2:   ANALYTICAL
SIMULATION OF SPS SYSTEM PERFORMANCE Final   Unclas
Report (LinCom Corp., Pasadena, Calif.)   G3/44   27697

OCT 81
RECEIVED
NASA STI FACILITY
ACCESS DEPT.
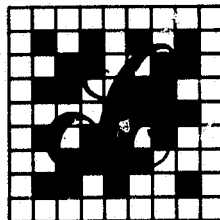
LinCom Corporation

P.O. Box 2793D, Pasadena, Calif. 91105

LinCom

SOLAR POWER SATELLITE ANTENNA PHASE CONTROL SYSTEM

HARDWARE SIMULATION PHASE IV

VOLUME II. ANALYTICAL SIMULATION OF SPS SYSTEM PERFORMANCE

PREPARED FOR

NASA LYNDON B. JOHNSON SPACE CENTER
HOUSTON, TX   77058

TECHNICAL MONITOR: JACK SEYL EE 7

CONTRACT NO. NAS9-16097

PREPARED BY

W. C. LINDSEY
A. V. KANTAK
C. M. CHIE

LINCOM CORPORATION
P.O. BOX 2793D
PASADENA, CA 91105

MARCH 1981

LinCom

TABLE OF CONTENTS

TABLE OF CONTENTS (continued)

1.0 INTRODUCTION

A critical requirement for the proposed Solar Power Satellite (SPS) concept is the ability of the satellite to beam and focus microwave energy to a predetermined spot located on the Earth's surface from a geosynchronous orbit of 37,000 km. In Reference 1 a SPS transmission system incorporating automatic beam forming steering and phase control was presented. The phase control concept which centers around the notion of an <u>active retrodirective phased-array</u> is described in detail in Reference 1. Figure 1.1 illustrates the major elements necessary in the operation of an SPS system which employs retrodirectivity as a means of automatically pointing the beam to the appropriate spot on the Earth. From Figure 1.1 we see that these include:

(1) The pilot beam transmitter.

(2) The power transmitter antenna, hereafter called the spacetenna.

(3) The receiving antenna called rectenna.

The rectenna and the pilot signal transmitter are located on the Earth with pilot transmitter located at the center of the rectenna. The purpose of the spacetenna is to direct the high power beam so that it comes into focus at the center of the rectenna. The rectenna is to be circular with approximately 10 km 'diameter', beamwidth of the high power beam has to be extremely narrow, in fact, on the order of one half minute of arc. The pilot signal transmitted from the center of the rectenna to the spacetenna provides the signal needed at the SPS to focus and steer the power beam.

The SPS phase control system is faced with several key problems. They are:

(1) Path delay variations due to imperfect circular orbits of SPS.

SOLAR POWER SATELLITE

SPACETENNA

UPLINK PILOT
REFERENCE BEAM

IONOSPHERE

DOWNLINK
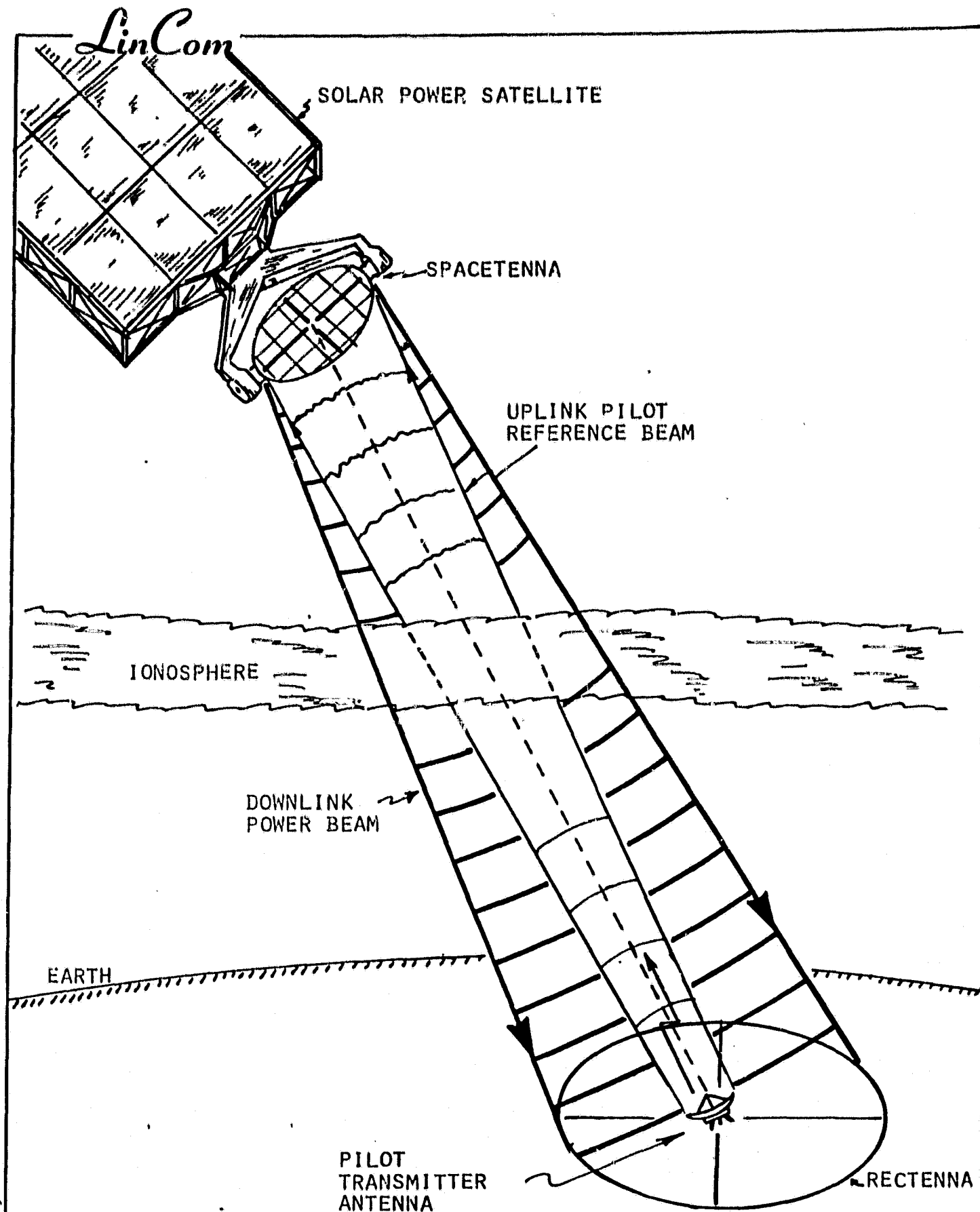POWER BEAM

EARTH

PILOT
TRANSMITTER
ANTENNA

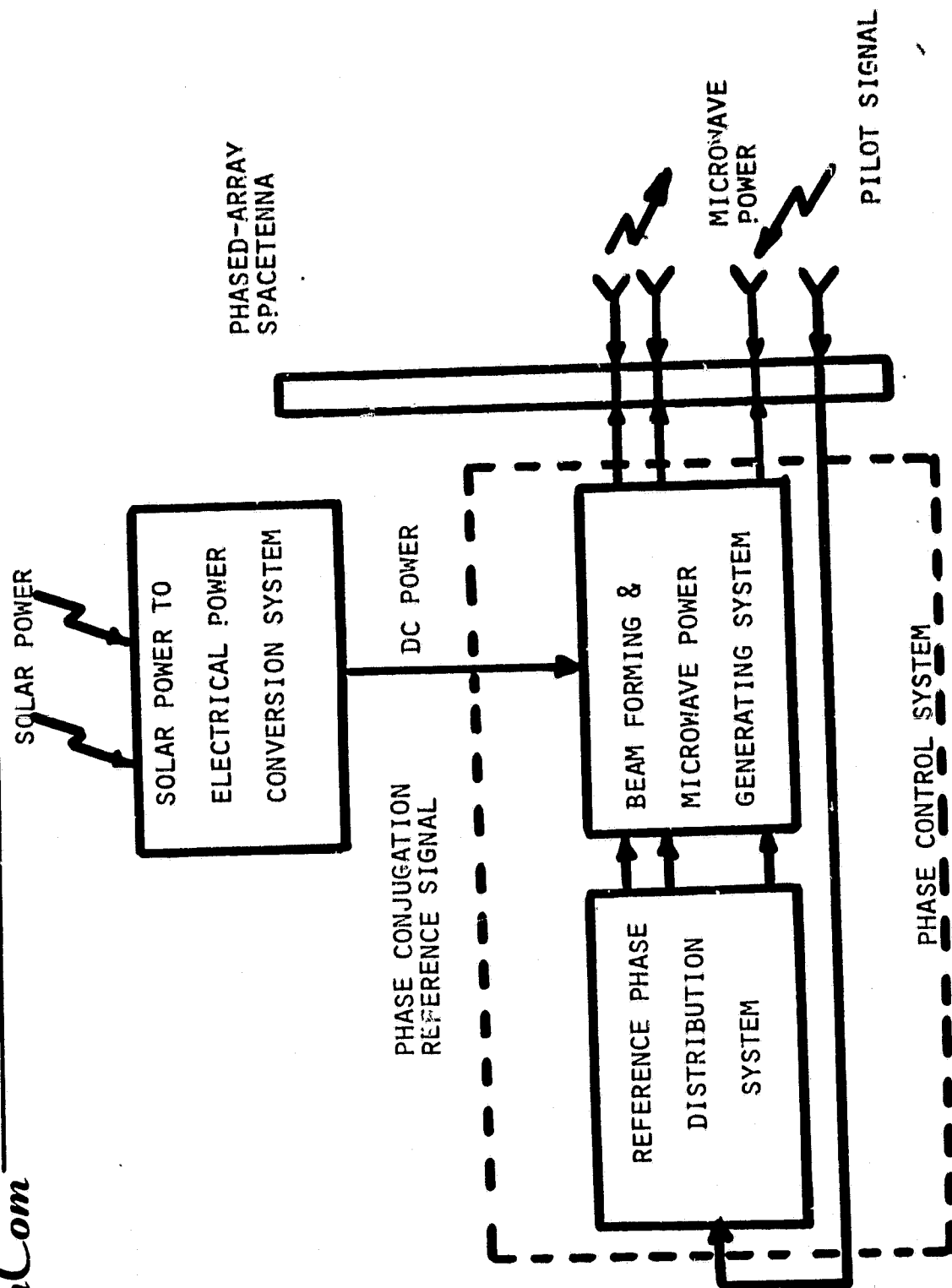RECTENNA

Fig. 1.1. ELEMENTS OF SOLAR POWER SATELLITE SYSTEM

Fig. 1.2. SOLAR POWER SATELLITE (SPS) TRANSMISSION SYSTEM.

(2) Ionospheric effects.

(3) Initial beam forming.

(4) Beam pointing.

(5) Beam safing.

(6) High power amplifier noise effects.

(7) Interference.

1.1 SPS Transmitting System Concept

From the system engineering viewpoint, the SPS transmitting system which incorporates retrodirectivity is depicted in Figure 1.2. A central feature of the SPS transmitting system is the 101552 element retrodirective active phased array (spacetenna) [2], [3] of 1 km diameter designed to focus and point the phase coherent microwave beam to a ground based microwave antenna (rectenna) which is approximately 10 km in diameter. As seen from Figure 1.2 the SPS transmission system consists of three major distinct systems:

(1) The reference phase distribution system.

(2) The beam forming and microwave power generating system.

(3) The solar power to electrical power conversion system.

This report serves to document results from the pilot signal parameter optimization analysis, the power transponder analysis, modeling of the SPS antenna phase control system and from hardware simulation study. This study can be divided up into:

(1) Pilot signal parameter optimization.

(2) Ionospheric effects.

(3) Phase distribution system phase error effect.

(4) Parameter optimization of the spread spectrum receiver consisting of the carrier tracking loop and the code tracking loop parameter optimization.
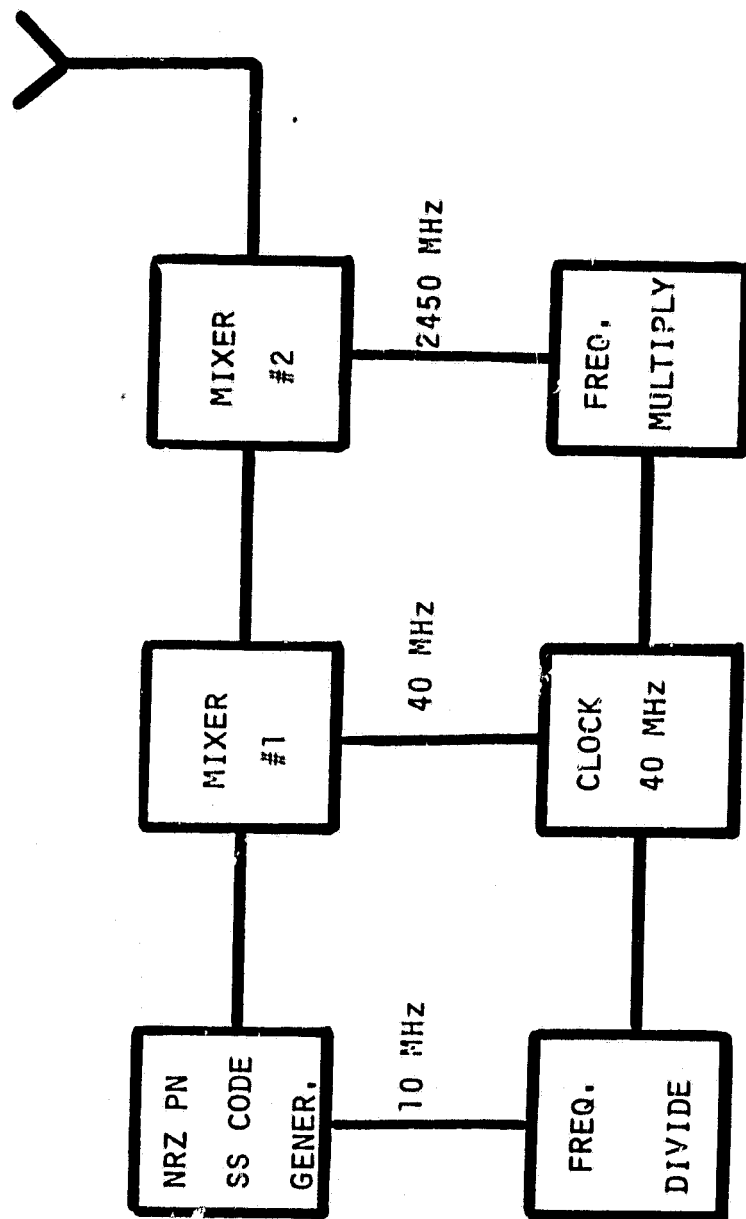
Fig. 2.1. REFERENCE SYSTEM PILOT SIGNAL TRANSMITTER FUNCTIONAL DIAGRAM.

(5) Effects of high power amplifier phase and amplitude jitters.

The subsequent chapters document the mathematical modeling and the resulting parameter optimization of each of the above.

2.0 SPS PILOT SIGNAL DESIGN OPTIMIZATION

The spacetenna is rated to radiate 6.5 G watts of power and at the same time it is deemed to be operating on retrofire principle. This creates the well known frequency isolation problem between uplink and the downlink signal. Penalty for neglecting this problem is too high, hence a special shaping of pilot spectrum becomes necessary. We wish to design the pilot signal communications system to operate reliably in the face of several types of interference:

(1) The downlink power beam signal.

(2) Noise in the spacetenna receiver.

(3) Unintentional and intentional RFI.

(4) Intelligent beam stealing signals.

Figure 2.1 illustrates the proposed pilot signal transmitter in block diagram form. As it is shown in the figure the pilot waveform will be a NRZ pseudo noise code of chip rate 10 MHz amplitude modulated on the subcarrier of 40 MHz. This subcarrier then amplitude modulates the carrier at 2.45 GHz. This signal is then amplified by a high power amplifier and then radiated from the center of the rectenna to the spacetenna.

2.1 Pilot Signal Format and Spectrum

The NRZ pseudo noise modulation $c(u,t)$ on the pilot is assumed to be of the form

$$c(t) = \sum_i a_i P(t - iT_c) \qquad (2.1\text{-}1)$$
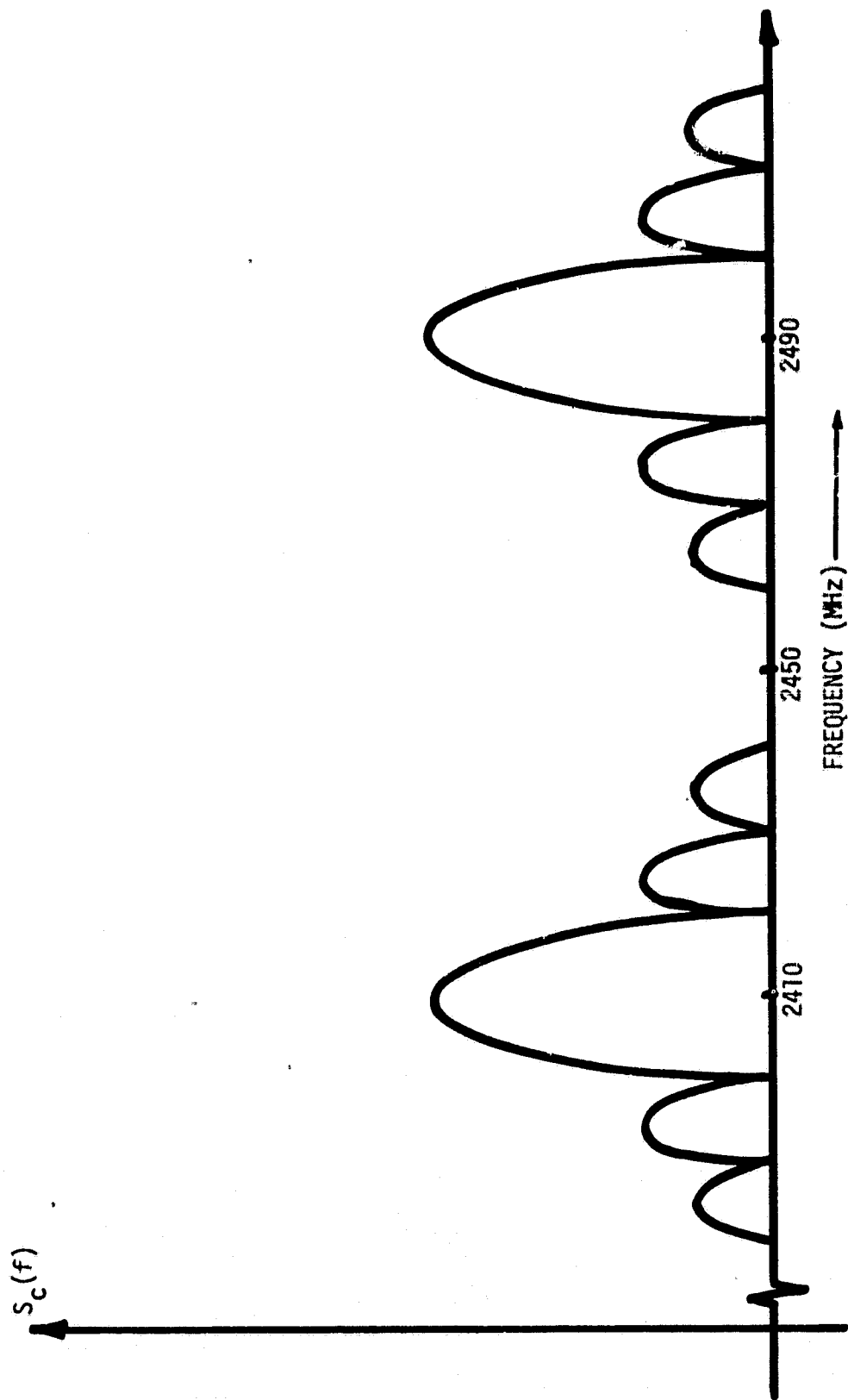
Figure 2.2. Power Spectrum of the Suppressed Carrier Pseudo Noise Pilot Signal.

where

$$a_i = \pm 1 \text{ with } P[a_i = 1] = P[a_i = -1] = 1/2$$

$$P(t) = \begin{cases} 1 & -T_c/2 < t < T_c/2 \\ 0 & \text{elsewhere} \end{cases}$$

with T_c = chip time of 0.1 μsec, and E_b equals energy in a bit.
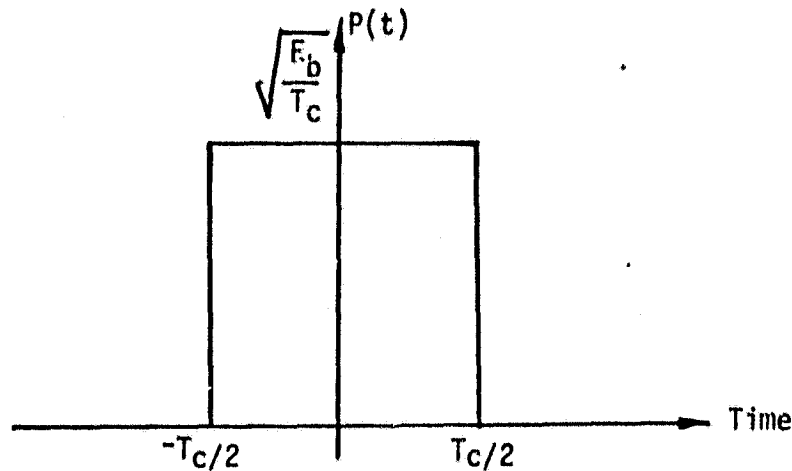
Figure 2.2 shows the power spectrum associated with the received pilot signal at the subarray terminal (noise is assumed to be absent at the moment). The pilot signal shall be assumed to be of the form

$$s_p(t) = Re\{[c(u,t)a(u,t)]e^{j\omega_c t}e^{j\omega_{c_1} t}\} \qquad (2.1-2)$$

where u is a sample space parameter introducing randomness

MSRTS PHASE DISTRIBUTION SYSTEM

SIGNAL PROCESSOR #1

• • • •

SIGNAL PROCESSOR #N

X M I T #1

R C V R #1

$n_1(t)$

X M I T #N

R C V R #N

$n_N(t)$

• • • •

P O W E R B E A M

MUTUAL COUPLING

P O W E R B E A M

SELF COUPLING

PILOT SIGNAL WAVE FRONT

INTENTIONAL AND UNINTENTIONAL INTERFERENCE
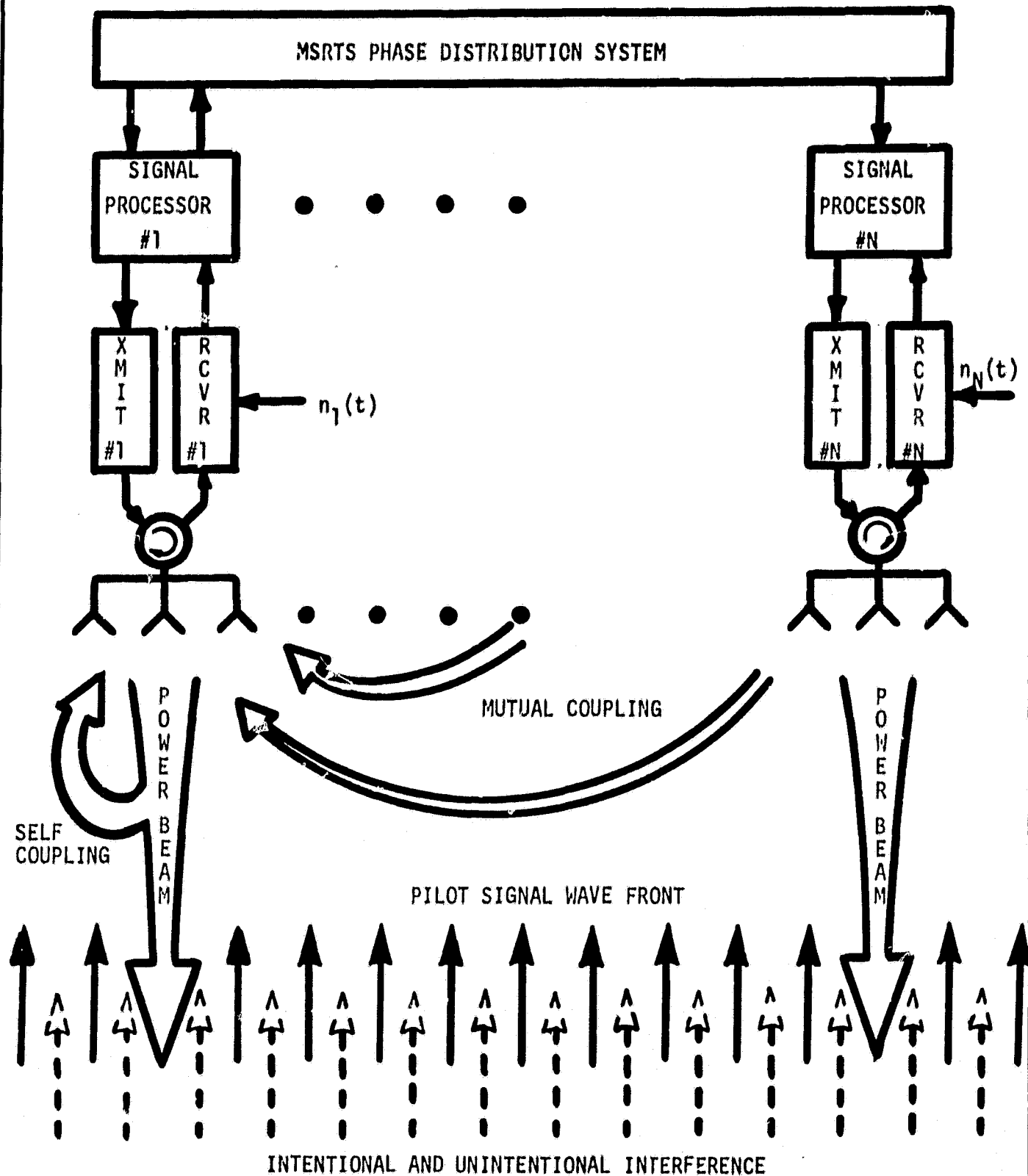
Figure 2.3 Noises Added at a Typical Radiator.

COHERENT PHASE
NOISE INTERFERENCE

NONCOHERENT PHASE
NOISE INTERFERENCE

FRONT END BANDPASS FILTER

UPLINK PILOT
SIGNAL

RECEIVER
NOISE N_0

$2R_c$

2410

2450

2490

FREQUENCY (MHz) ⟶

Fig. 2.4. SIGNAL AND NOISE SPECTRUM INTO MPTX TRANSPONDER

$$\omega_c = 2\pi \times 2450 \times 10^6 \text{ rps}$$

$$\omega_{c_1} = 2\pi \times 40 \times 10^6 \text{ rps}$$

this signal goes through the atmospheric randomness and delay due to the propagation path which will be incorporated as $\tau(u)$ and the pilot signal received at the spacetenna signal processing ports could be modeled as

$$s_p'(t) = Re\{[c(u,t-\tau(u))a(u,t-\tau(u))]e^{j\omega_{c_1}t}e^{j\omega_c t}\} \qquad (2.1-3)$$

The spectrum of the uplink CW pilot tone depicted in Figure 2.2 shows that the subcarrier modulation shifts the spectrum of the NR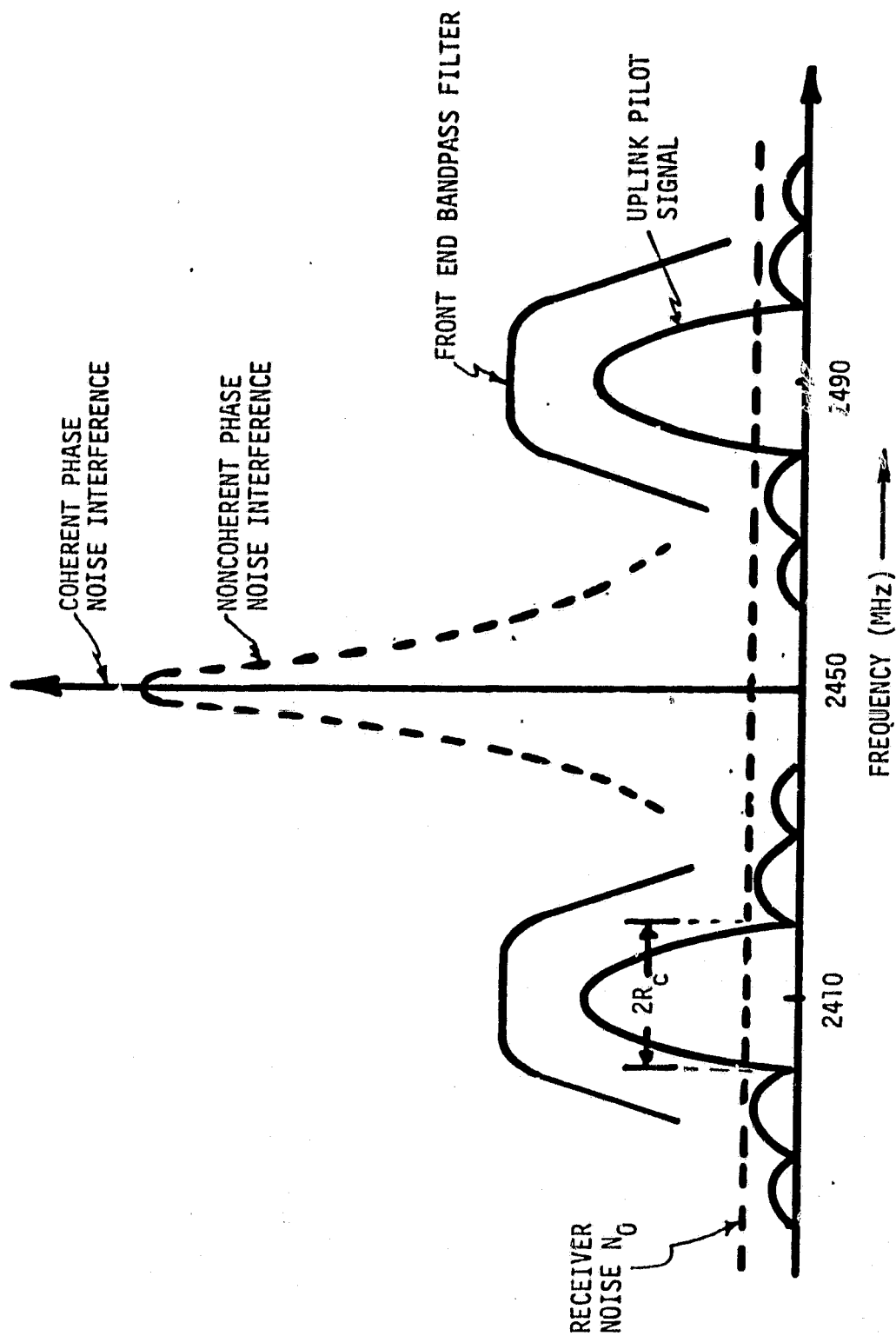Z pseudo noise code by 40 MHz on either side of the uplink carrier frequency of 2.45 GHz suppressing the carrier component. Thus the sidelobes of the uplink pilot signal are separated by a 80 MHz band. This feature of the spectrum is used to effectively reduce the noise which resides at the carrier frequency. The side lobes are used to regenerate the suppressed carrier frequency and later the phase of the carrier is used in the conjugation circuitry to retrodirect the power beam to the rectenna center.

As mentioned before, the pilot signal encounters several types of noises before it illuminates the aperture of the spacetenna Figure 2.3 shows pictorially the basic noises added to the uplink pilot beam at the spacetenna center and Figure 2.4 depicts the spectrum of signal plus noise. As seen from this figure the separation between the pilot signal lobes and the concentration of noise around carrier frequency (the

modeling of this noise is done in later chapters) allows the front end filter of the SPS receivers to reduce the noise effectively.

The signal parameter design values, i.e., the chip rate, EIRP, code period, etc., will be given in a later chapter because these quantities are intimately related with the pilot receiver design to be used.

3.0 IONOSPHERICS

The microwave beam of the SPS is to be formed and focused by the spacetenna using the phase information residing on the uplink pilot beam emanated from the center of the rectenna. Microwave power beam interaction with the ionosphere may have considerable repercussioins on the design of the transmission system, i.e., the uplink pilot beam has to propagate through a heated ionosphere containing natural and probably artificial irregularities inflicting perturbation of the phase of the pilot beam with possible consequence to the beam forming and focusing of the downlink power beam.

3.1 Effect of Ionospheric Irregularities on the Pilot Beam

Ionosphere has naturally generated electron density fluctuations. These small natural density fluctuations cause a variation in the plasma's index of refraction. Due to these variations the incident power beam focuses and defocuses as it passes through these fluctuations. In the region where plasma is relatively less dense, the electric field intensity of the wave is increased slightly. This increased intensity of electric field causes more plasma to drift out from the less dense region. Thus the initial natural perturbation is amplified. This process continues until hydrodynamic equilibrium is reached creating large scale irregularities aligned along the direction of the magnetic field in the plasma. The width of the striation is
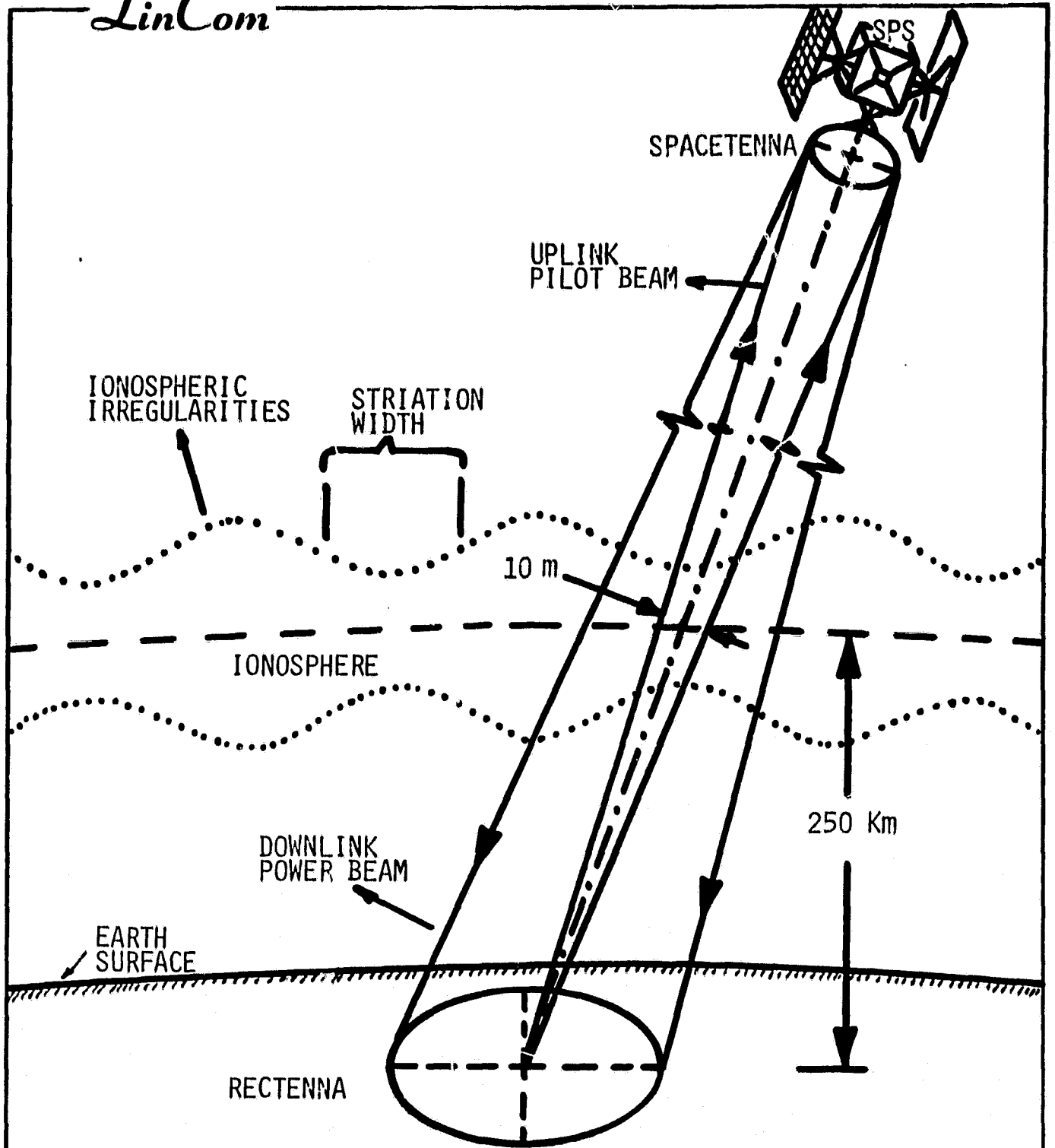
Fig. 3.1.

determined by the ionospheric condition, the power density of the incident downlink beam and upon the angle the electromagnetic wave makes with the magnetic field of the plasma.

The horizontal dimension of the SPS power beam will be of the order of 5 Km in the ionosphere, neglecting striations of width more than 5 Km becomes sensible. To have any significant impact, several striations should be formed inside the heated region. Therefore, it is reasonable to consider striation widths of 1 Km. Figure 3.1 illustrates the concept of ionospheric irregularities.

Scintillation of radio waves propagating through an ionosphere containing irregularities arises from two phenomena: diffractive scattering and refractive scattering. Diffractive scattering is important if the scale T_D of the irregularity normal to the line-of-sight is a Fresnel zone, i.e.,

$$T_D = (\lambda d/2\sqrt{2}\pi)^{1/2}$$

where λ is the radio wavelength and d is the distance of the irregularity to the receiving terminal (for the SPS problem the transmitter can be assumed to be at a very large distance from the ionosphere so that a plane wave impinges on the ionosphere). If the ionospheric irregularities have scales equal to or less than T_D then diffractive scattering is important. If the scales are larger than T_D, diffractive scattering will be dominated by refractive scattering provided the scale associated with refractive scattering T_R is larger than T_D.

The refractive scattering scale T_R is the displacement normal to

the line-of-sight of a scatterer for which the incident angle exceeds the critical angle of optics, θ_c, given by

$$\sin \theta_c = (n-\Delta n)/n$$

where n is the refractive index of the medium and $n-\Delta n$ is the refractive index of the scatterer. The grazing angle α is the complement of the critical angle, and the displacement of the scatterer from the line-of-sight at a distance d from the receiver is $2\alpha d$.

$$\cos \alpha = 1 - (\Delta n/n)$$

$$\alpha^2 = 2(\Delta n/n) \text{ for small angles.}$$

For fluctuations in electron density N,

$$\alpha = \frac{\lambda}{\lambda_N} \{\overline{(\tfrac{\Delta N}{N})^2}\}^{1/4}$$

where λ_N is the wavelength associated with the plasma frequency.

The displacement from the line-of-sight of a scatterer that justifies the critical angle condition is T_R.

$$T_R = 2\alpha d = 2d \frac{\lambda}{\lambda_N} \{\overline{(\tfrac{\Delta N}{N})^2}\}^{1/4}$$

For the SPS case, T_D is about fifty meters and T_R is about 100 meters for 1% fluctuation of electron density ($\Delta N/N = 10^{-2}$), increasing to 300 meters for 10% fluctuations and one kilometer for 100%

fluctuations. One can make a self-consistent argument that a scatterer 100 meters off the line-of-sight having an electron density 1% below ambient will reflect a ray to the receiver. The reflected amplitude will be significant if the reflecting surface is a reasonable fraction of a Fresnel zone, and this is achieved easily in one direction (the reflecting surface should be 50 meters normal to the path), but more difficult in the direction approximately along the path, Ref. 6.

While the outline here is simplified, it suggests (1) that the observed scintillations in the tropics may be accounted for by refractive scattering, (2) that the uplink pilot beam may be subject to refractive scattering and the question can only be answered with certainty by an experimental test.

We first estimate the extra path imposed on a ray passing through an irregularity having an electron density $N-\Delta N$ compared with the ambient N. Adding satistically the effects of a number of irregularities traversed sequentially, we arrive at an extra length, or a phase difference between two rays, and find that the phase difference is about a degree.

The refractive index for a radio wave of angular frequency ω of an ionosphere of plasma frequency ω_N is

$$n = 1 - (\omega_N/\omega)^2$$

and $\qquad \omega_N^2 \alpha N.$

Since the wave travels at a speed c/n through the medium, the extra path can be calculated by comparing the speed in the irregularity and the speed in the ambient medium. For the ray theory approach to theuplink problem, scales of the order of 10 meters are of interest since that is
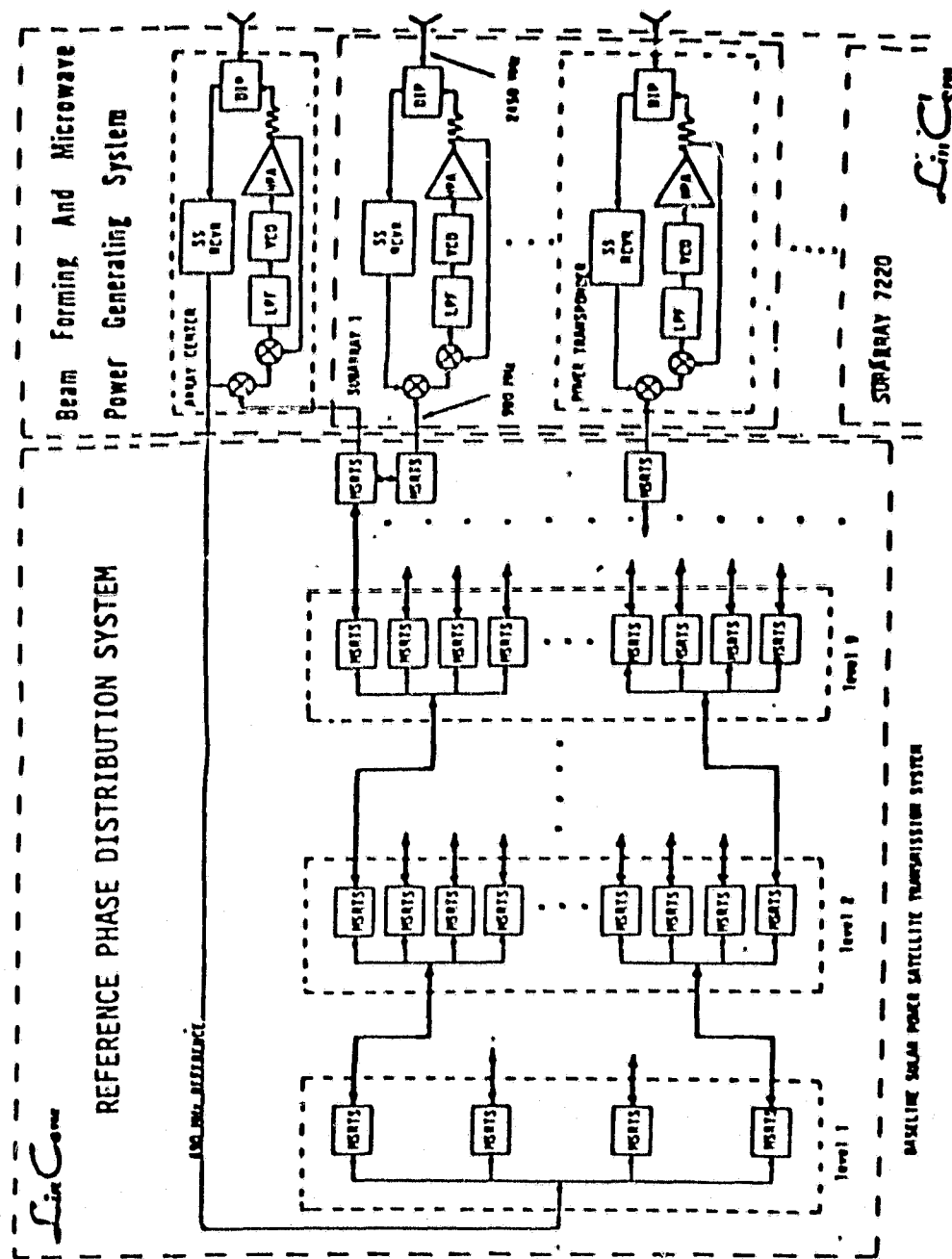
Fig. 4.1. SPS PHASE CONTROL SYSTEM.

the separation in the ionosphere of two rays originating at the uplink transmitter and striking the edges of the SPS transmitting antenna. If one assumes the SPS beam may induce changes of 2% in the electron density then the change in the index refraction is 2×10^{-7} and the change in path length through a 10-meter irregularity 3×10^{-6} meters or 10^{-2} phase degrees at 2.45 GHz. If the ray travels through 200 km of ionosphere, encountering irregularities every 20 meters, then the number of independent samples is 10^4 and the statistical sum is 10^2 times the single irregularity extra path or about one degree. This should provide a phase jitter background of about a degree.

The phase jitter on the pilot signal is thus assumed to be 2^0 to 3^0 and at the same time it is assumed that the power beam is affected only very little due to the ionospheric irregularities. This result is dependent upon the data so far available and should not be taken as the final design number more relevant data is necessary before such a decision is made.

4.0 <u>MSRTS PHASE DISTRIBUTION SYSTEM</u>

To maintain the precise phase distribution accuracy required over the one kilometer aperture of the spacetenna the baseline system uses the MSRTS technique. The MSRTS concept was described in great detail in [4] hence the system will be described only briefly here.

Figure 4.1 describes the entire phase control system of the SPS in block diagram form in which the baselined tree structure format of the phase distribution system is quite apparent. The parameters of the tree to be optimized include:

(1) The number of levels in the tree.
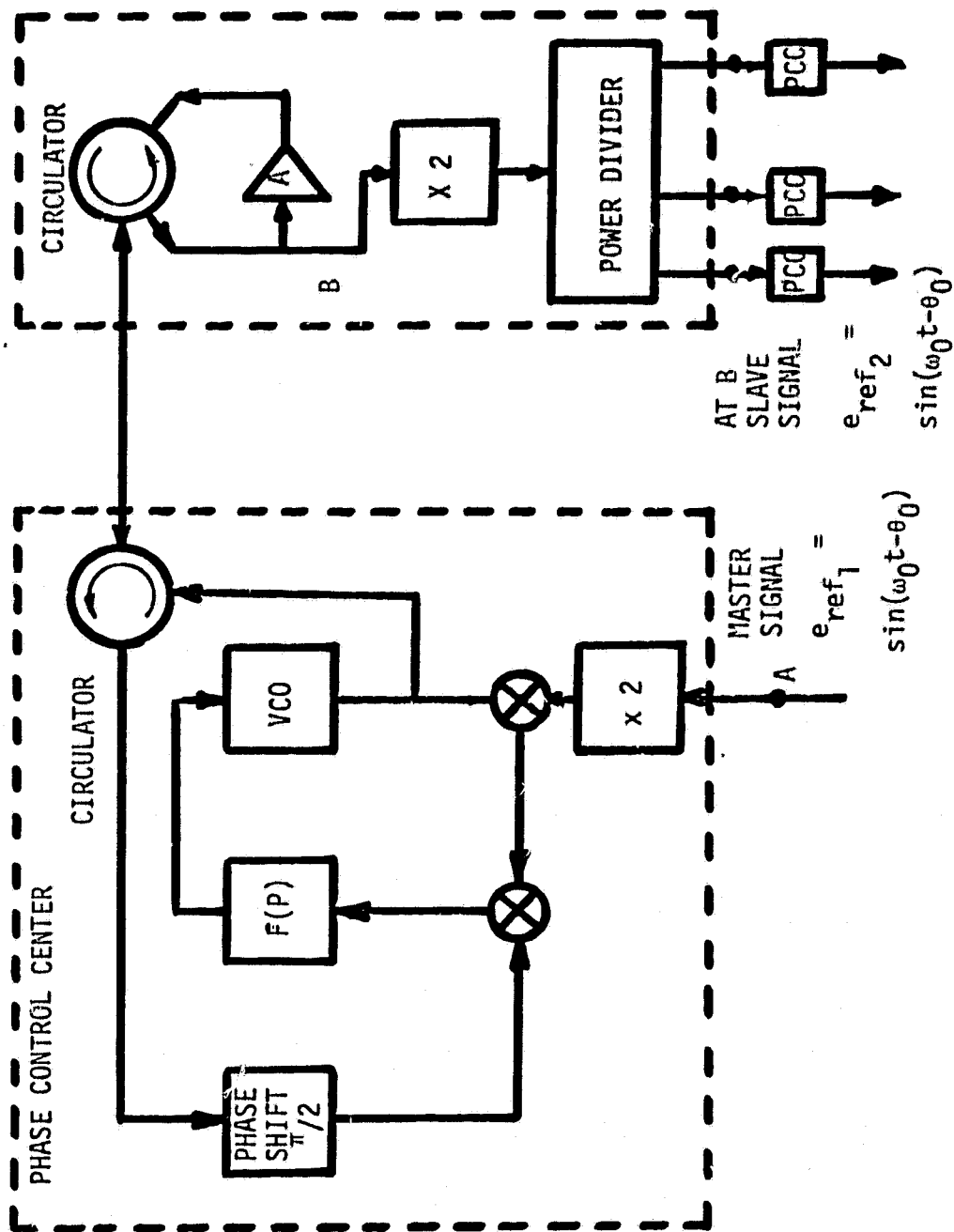
(2) The number of branches per level.

Fig. 4.2. MASTER SLAVE RETURNABLE TIMING SYSTEM

(3) The interconnecting cable length.

In Figure 4.2 we see that a portion of the reference signal at the received location is amplified and coupled back into the phase distribution cable via a circulator. This return signal component is then used for phase locking to the original reference input of the Phase Control Center (PCC). Thus the phase of the VCO in the PCC is advanced by an appropriate amount so that the phase of slave signal $e_2(t)$ equals the phase of the reference signal $e_1(t)$ transmitted via the "cable". Since the same frequency is transmitted both directions over the cable, phase error build up due to frequency dispersion on the cable is eliminated. When phase lock is achieved in the PCC, the resultant phase at point B in Fig. 4.2 equals the phase at point A even if the effective cable delay varies. If the connection cable is cut to within plus or minus one-fourth of an integer number of wavelengths at the distribution signal frequency, the phase can be distributed accurately over various lengths of cable without phase ambiguity. For example, for a frequency of 490 MHz, the cable lengths must be cut to within plus or minus fifteen centimeters to avoid ambiguities.

4.1 Tree Structure Used to Transfer Phase Between PCCs

In general a symmetric tree structure is defined by two parameters, viz., the number of levels, say L and the number of branches per level, say n. For such a tree there would be n^L terminal nodes. If such a tree is used to supply the conjugator reference signal for the spacetenna transponders, one can have n^L transponders supplied by the constant phase. Here the parameter n describes the number of output terminals associated with the power dividers necessary in the implementation.

LEVEL 1

16

LEVEL 2

16 16

LEVEL 3

16 16

25 25 LEVEL 4
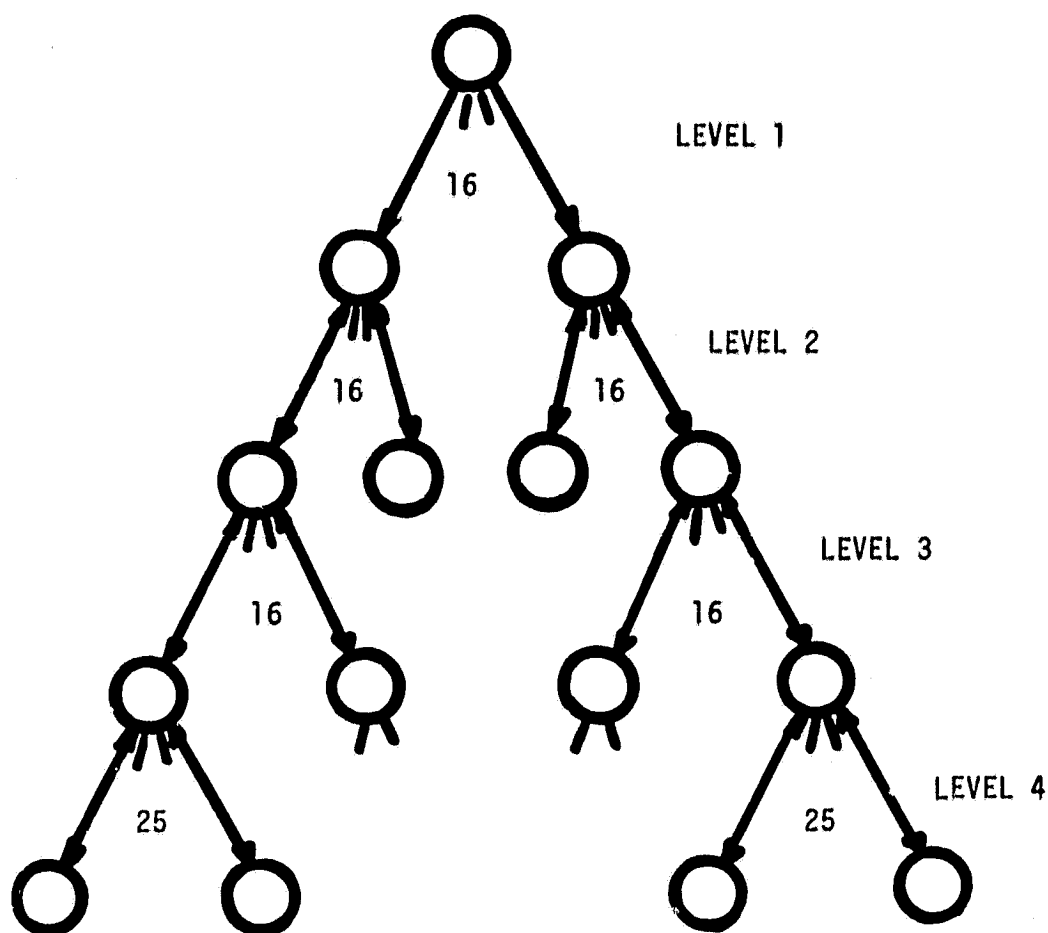
- PHASE NOISES ARE CORRELATED

- POWER SPLITTERS, POWER TRANSPONDERS, PHASE TRACKING PLLS, MULTIPLIERS, MICROWAVE HARDWARE COMPONENTS

Fig. 4.3. FOUR LEVEL PHASE DISTRIBUTION TREE.

The phase transfer between the tree levels will be achieved by the MSRTS technique. In the distribution tree each MSRTS feeds a power splitter each output of which feeds the next level MSRTS. This partitioning continuous until the tree structure is completed. Since there are 101552 power amplifiers then the parameters n and L must be selected to best match the requirements.

In order to evaluate different phasing tree structures, one has to study the effects of tree structure on the spacetenna performance. This has been done in the previous work by LinCom [4]. In particular, the boresight gain reduction and the spacetenna pointing error are two important performance measures for merit comparison. The boresight gain reduction is proportional to the efficiency of the microwave transmission system. The pointing error measures the ability of the spacetenna to focus on the center of the rectenna. SOLARSIM has been developed to investigate these effects. The baseline phase distribution tree has four levels and is shown in Figure 4.3. Note that a total of 102400 terminal nodes are possible out of which 101552 nodes will be used.

As seen earlier, there is a lot of hardware in each MSRTS circuit. In actual practice the hardware is not ideal and hence they introduce phase errors in the system which the MSRTS cannot eliminate there are several such sources which are enumerated below:

(1) Multipliers.

(2) Power splitters.

(3) Directional coupler.

(4) Mismatched terminating impedances.

(5) Phase locked loop imperfections.

Thus each MSRTS circuit located at each node of the four level phase distribution tree adds an irreducible error to the constant phase being handed down from level to level.

The table given below shows the partitioning of phase error build up in the reference phase distribution system for an allowable total rms phase error build up of 7.5^0.

4.2 Effect of Baseline Tree Structure on Main Beam Gain Loss

The main beam gain reduction is a function of the magnitude of and the level where the phase errors are introduced by the phasing tree. It is interesting to see the extent to which the phase errors introduced at each level individually contributes to reduce this gain. In Fig. 4.4, we show the effect of the phase errors introduced at a particular level in the phase distribution tree, while the phase error at the other levels are neglected. A phase jitter of 5^0 is shown for a four level tree. The normal main beam gain loss of gain in dB is plotted in Fig. 4.4

The quantity G_0 is obtained when all the phase errors introduced in the phasing tree are set to zero. From Fig. 4.4, we see that as far as the gain reduction is concerned, hase error introduced in the last level (4th level) results in the worst performance. Intuitively, phase errors introduced at the beginning levels of the tree cause the total phase error build up at the radiating elements to be correlated. As a result, individual patterns all add up in the same general direction. On the contrary, when phase errors are introduced in the last level, radiating elements have uncorrelated phase errors which results in reduced main beam gain. In any case, the differences are small.

PARTITIONING OF PHASE ERROR BUILD-UP IN THE REFERENCE PHASE DISTRIBUTION SYSTEM

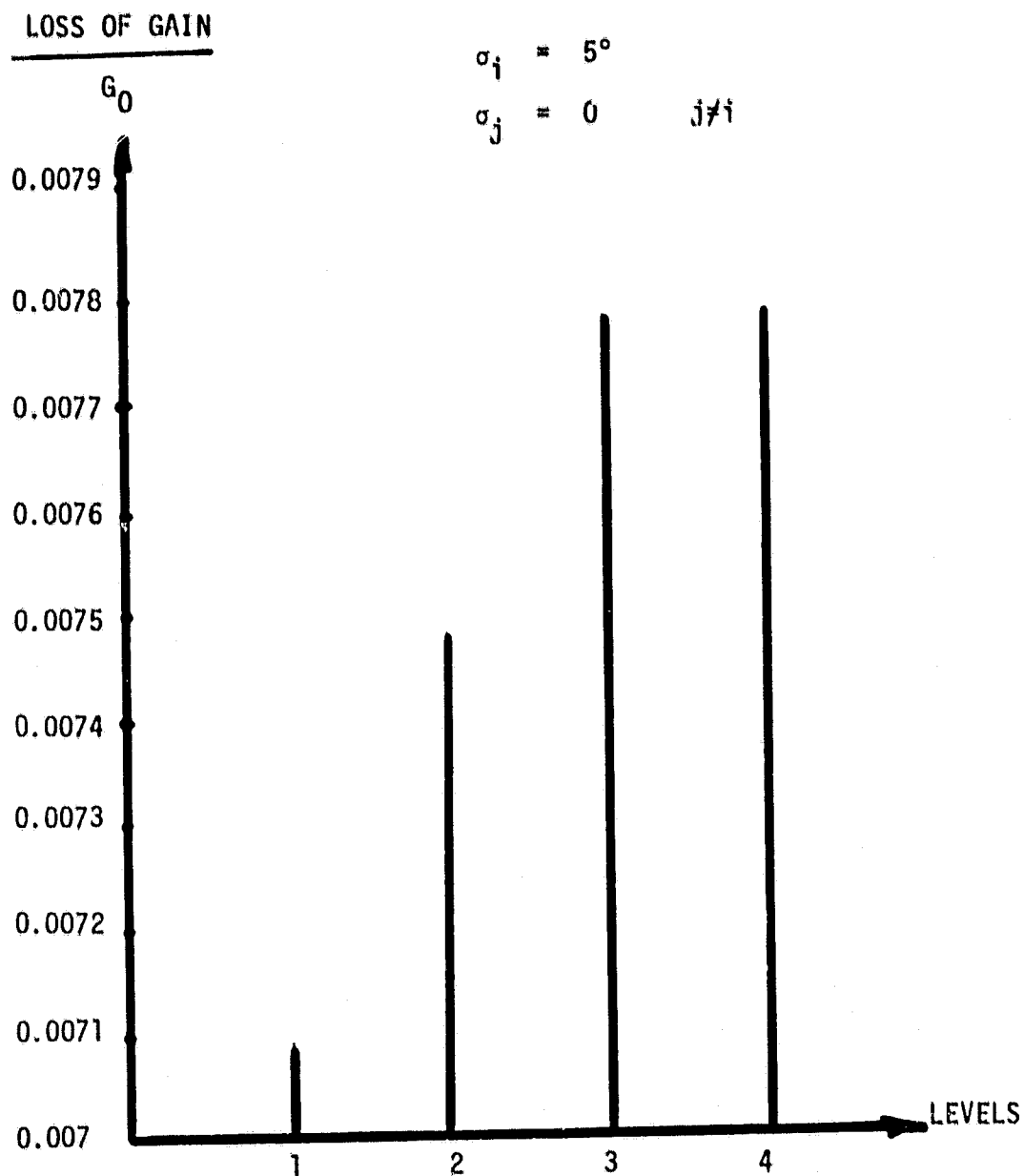| SOURCE	TOTAL RMS PHASE ERROR BUILD UP AT THE END OF THE DISTRIBUTION TREE
PILOT SIGNAL RECEIVER AT THE CENTER OF SPACETENNA	3^0
POWER SPLITTERS IN THE PHASE DISTRIBUTION TREE	6^0
PHASE NOISE OF THE VCO IN THE PHASE DISTRIBUTION TREE	2.4^0
UNCOMPENSATED PATH DELAYS	2.4^0
TOTAL RMS PHASE ERROR BUILD UP	7.5^0

Fig. 4.4. EFFECT OF PHASE JITTER INTRODUCED IN DIFFERENT
LEVELS OF THE 4-LEVEL PHASE REFERENCE TREE.

$\log_{10}(\sigma_{\Delta u})$, dB min

4 LEVEL DISTRIBUTION TREE

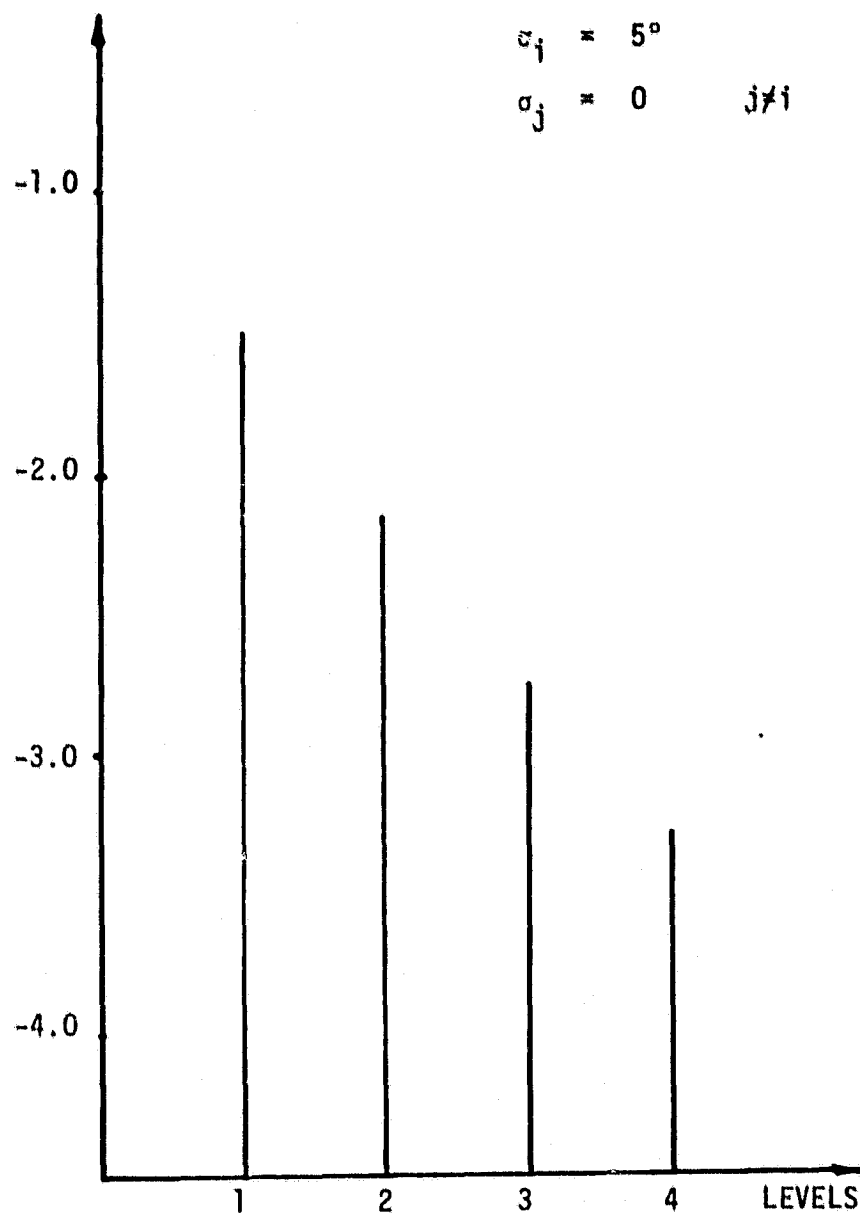$\sigma_i = 5°$

$\sigma_j = 0 \qquad j \neq i$

Fig. 4.5. RMS POINTING ERROR AS A FUNCTION OF THE LEVEL WHEN PHASE ERRORS ARE INTRODUCED FOR A FOUR-LEVEL TREE.

4.3 Effect of the Baseline Tree Structure on RMS Pointing Error

The ideal spacetenna attains its peak power density in the direction of the rectenna center. Under the assumption that the power beam is focused properly, the purpose of the phase control system is to phase its individual radiating elements so that the boresight gain is maximized. When random errors are introduced by the phasing system, the antenna power pattern peaks at some direction other than the boresight. The variance of the direction is specetenna pointing error.

Depending on the level where phase errors are introduced, the resulting pointing error is different. From Fig. 4.5, we can see that the phase error introduced at the first level causes the largest rms pointing error while the phase error from the last level (level four) has the least impact. In essence, if independent phase errors are introduced at the last level, the resultant phase error variance on the beam is reduced roughly by the number of radiating elements (101552). This follows from the law or large numbers. However, if the phase errors are introduced at the first level, the resultant phase error variance on the beam is reduced by the number of nodes in the first level. For the baseline (4-level tree), that number is 25. The square root of the ratio 101552/25 is roughly 18 dB, which can be observed in Fig. 4.5.

Thus the four level phase distribution tree with 16x16x16x25 nodes serves the purpose very well. Candidate trees with 8 and 9 levels and 4 branches per node were also considered but as the number of levels increases, the total accumulated phase error at the end of the tree increases compared to the accumulated phase error of an equivalent tree but with less number of levels.
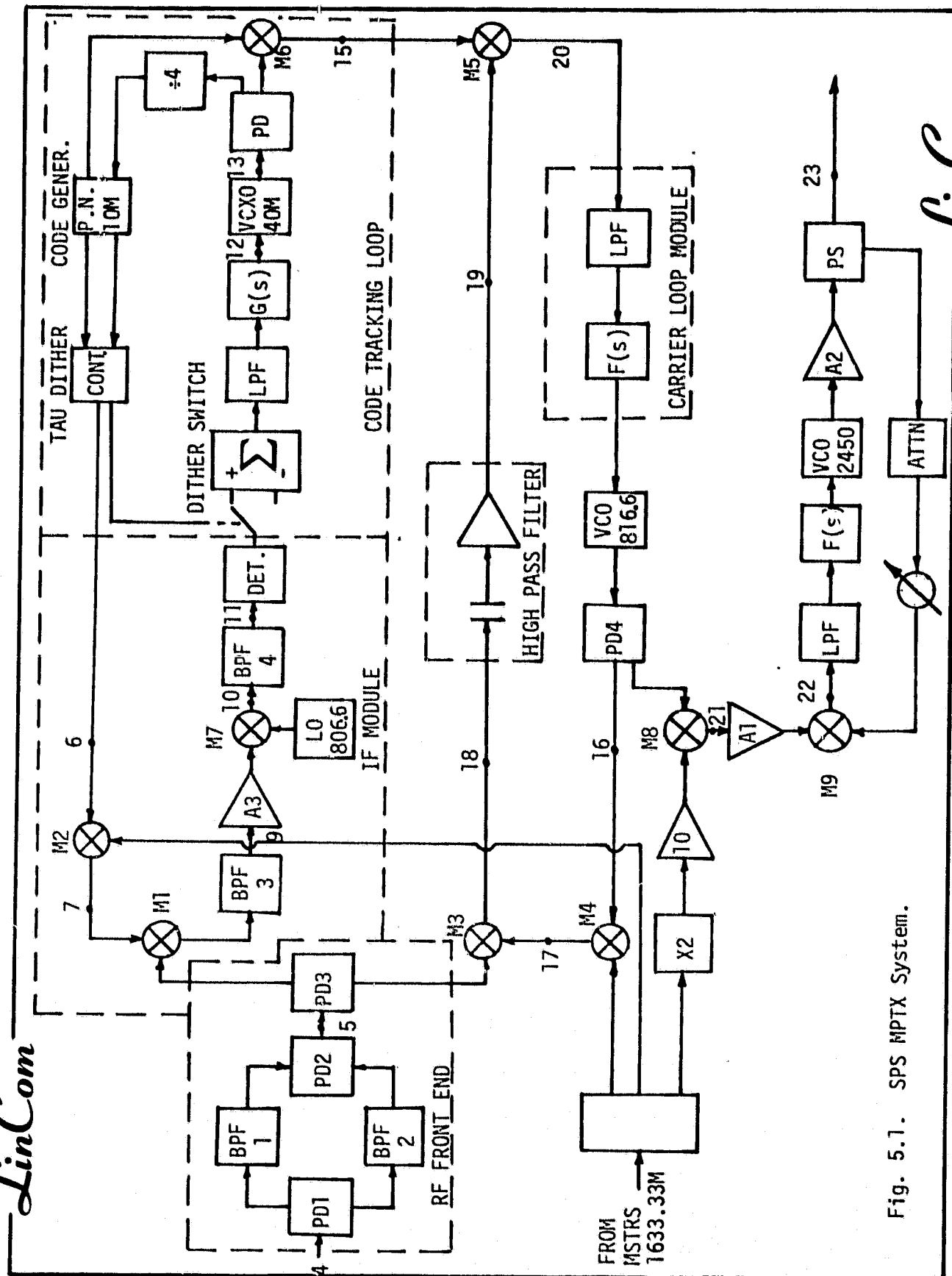
Fig. 5.1. SPS MPTX System.

5.0 SPREAD SPECTRUM TRANSPONDER

In the previous chapter we described MSRTS, a method of distributing the constant phase creating a constant phase reference necessary for successful operation of retrodirective spacetenna. In addition to distributing the constant phase reference signal over the spacetenna a method of recovering the phase of the received uplink pilot signal is required. Figure 5.1 represents the functional diagram of the SPS power transponder. This includes pilot signal receiver, phase conjugation electronics and the high power amplifier phase control system.

In the mechanization of the SPS power transponders, two receiver "types" will be required; however, most of the hardware will be common between two receivers. One receiver, the Pilot Spread Spectrum Receiver, is located at the center of the spacetenna or the reference subarray. It serves two major functions: (1) acquires the SS code, the carrier and demodulates the command signal, (2) provides the main input signal to the Reference Phase Distribution System.

The second receiver "type" will be located in the Beam Forming and Microwave Power Generating System. Its main purpose is to phase conjugate the received pilot signal and transpond power via the j-th spacetenna element, $j = 1,2,\ldots,101,552$.

The spacetenna is composed of 101552 variable size square subarrays which range from 1.73m x 1.73m to 5.2m x 5.2m operating at a frequency of 2450 MHz.
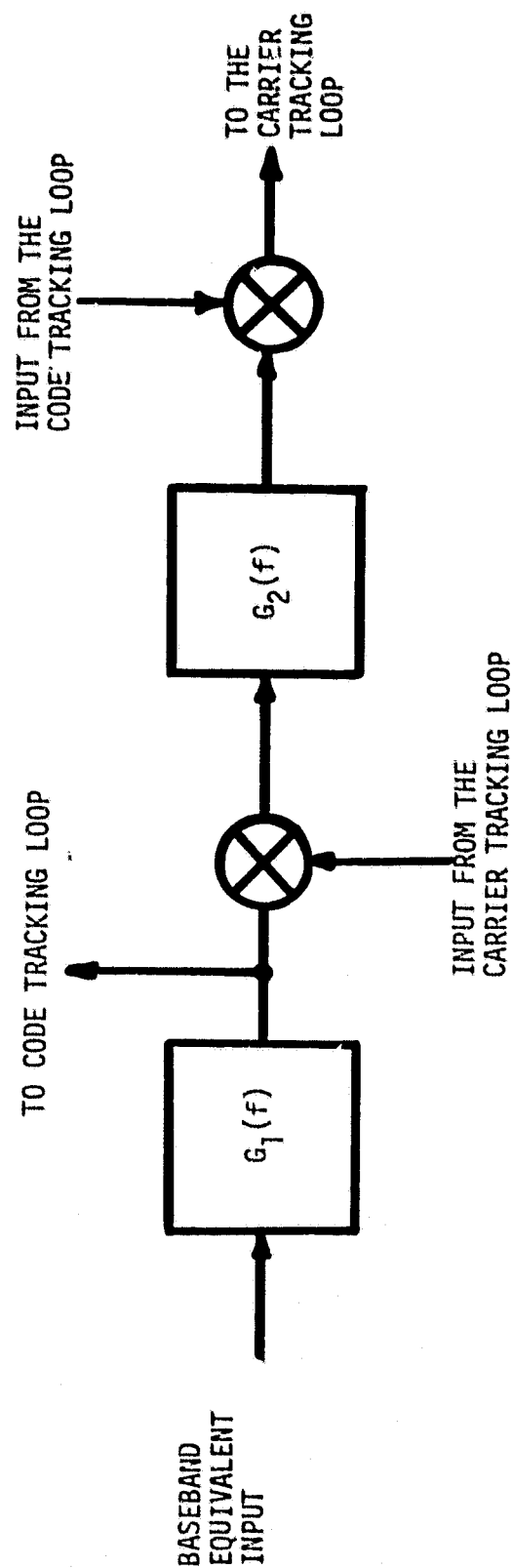
The uplink pilot beam encounters various kinds of noises which we have enumerated before there being the downlink power beam, noise in the spacetenna, receivers, intentional and unintentional RFI, and last,

intelligent beam stealing signals. The spectrum of the incident pilot plus noise at the spacetenna receiver ports is shown in Figure 2.3.

The power beam signal contributed by the $i\underline{th}$ subarray is denoted by $s_i(t)$ for $i=1,2,\ldots,N$, measured at the output port of the $i\underline{th}$ transmitter. The signal at the output of the $j\underline{th}$ subarray's RF receiver is given by $r_j(t)$ and possesses components due to the power beam signals $s_i(t)$, $i=1,\ldots,N$, the receiver noise $n_j(t)$, the RFI $s_{RFI}(t)$, and a possible beam-stealing signal $s_{BS}(t)$, in addition to the desired pilot signal $s_p(t)$. If we knew all of these input signals to the scenario, we could develop a representation for $r_j(t)$, once we have the following additional information:

(a) The system function $H_{ij}(f)$ describing the coupling of the $i\underline{th}$ power beam signal to the $j\underline{th}$ receiver's RF output signal $r_j(t)$. This includes the effects of all waveguides, circulators, RF receiver filters, antennas, etc. This must be known for all values of i.

(b) The system function $H_{RF}(f)$ from the $j\underline{th}$ subarray's antenna terminal to the $j\underline{th}$ receiver's RF output signal $r_j(t)$. This also includes the effects of waveguides, circulator, RF filters, etc.

(c) Atmospheric and ionospheric channel models for the paths from the pilot signal transmitter, the RFI source, and the beam stealer to the antenna terminal of the $j\underline{th}$ subarray.

(d) A "threat model" indicating the capabilities and level of sophistication of the beam stealing processor.

Knowledge of the above quantities would make the analyses to follow more precise.

BASEBAND
EQUIVALENT
INPUT

TO CODE TRACKING LOOP

INPUT FROM THE
CARRIER TRACKING LOOP

$G_1(f)$

$G_2(f)$

INPUT FROM THE
CODE TRACKING LOOP

TO THE
CARRIER
TRACKING
LOOP

$G_1(f)$ Baseband Equivalent of the RF Front End Filter

$G_2(f)$ Baseband Equivalent of the High Pass Filter

Fig. 5.2.   Baseband Equivalent System.

$\mathcal{L}in\mathcal{C}om$

From Figure 5.2 we know that there are four parts of the transponder (1) front end filter, (2) carrier tracking loop, (3) code tracking loop and (4) conjugator and power amplifier stabilization circuit. In what follows, these will be described one by one.

5.1 Power Spectral Density Computation

Figure 5.2 shows the circuit diagram of the MPTX system. In Chapter 2 the form of pilot signal was given in (2.1-3). The RF and IF sections of the subarray receivers can be modeled under weak narrowband assumptions to an equivalent complex baseband signal processing model shown in Figure 5.2. The signal passes through the first filter and then gets multiplied by the reference phase. The output of this multiplier (M3) is modeled by

$$= \text{Re}\{c(u,t-\tau(u))a(u,t-\tau(u))e^{j\omega_{IF}t}e^{j\theta(u,t)}\} \qquad (5.2-1)$$

The output of M3 has the code in it, but due to the passage of the signal through the filters, the shape of the code pulse is changed, i.e., the pulse gets reshaped. Thus a realistic output of the multiplier would be

$$\text{Re}\{c'(u_1,t-\tau(u))a(u,t-\tau(u))e^{j\omega_{IF}t}e^{j\theta(u,t)}\} \qquad (5.2-2)$$

where

$$c'(u,t-\tau(u)) = \sum_i a_i Q(t-iT_c-\delta(u))$$

with

$\mathcal{L}in\mathcal{C}om$

$$Q(t) = P(t) * g_1(t).$$

This then passes through the second IF filtering which shapes the pulse a little more and hence

$$Q(t) = P(t) * g_1(t) * g_2(t) \qquad (5.2\text{-}3)$$

Now the despreading operation is carried out. This is simply multiplication by the local estimate of the code. After PN code reference multiplication the baseband equivalent to the carrier tracking loop module becomes

$$\text{Re}\{c(u,t-\tau(u))a(u,t-\tau(u))e^{j\theta(u,t)}\}c(u,t-\hat{\tau}(u)) \qquad (5.2\text{-}4)$$

This is the error driving the code tracking loop

$$c(u,t-\tau(u))c(u,t-\hat{\tau}(u)) = \sum_i a_i Q(u,t-\tau(u)) \times \sum_j a_j P(u,t-\hat{\tau}(u)) \qquad (5.2\text{-}5)$$

Note that if there is no distortion of pulse then $Q(t) = p(t)$ and the PN synch subsystem would eliminate the tracking error, i.e., $\hat{\tau}(u) = \tau(u)+\delta(u)$. Hence

$$c(u,t-\tau(u))c(u,t-\hat{\tau}(u)) = 1 \qquad (5.2\text{-}6)$$

But this would rarely be the case and so the multiplication of $c(u,t-\tau(u))$ and $c(u,t-\hat{\tau}(u))$ would be a periodic function and the period would be T_c secs. This function can be expanded in a Fourier series and we can pick up only those compnoents which are near the signal specturm

Other components will not be considered because they would be away from the signal (code) frequency and the bandpass filters would not allow them to exist. The nonzero term is then

$$\frac{1}{T_c} \int_{-\infty}^{\infty} |p(t)|^2 G_1(f) G_2(f) e^{j2\pi fc(u)} df \qquad (2.7)$$

where $p(f)$ is the Fourier transform of $p(t)$.

The interference spectral density at the output of the multiplier is given by

$$S_{c_k}(f) * \{ |G_2(f)|^2 |G_1(f)|^2 \lfloor (2N_0 + S_{m_{RFI}}(f)) + \sum_i^N \sum_k^N S_{m_k}(f) G_{ij}(f) G_{ij}^*(f) \rfloor \} \qquad (2.8)$$

The above two equations define the signal and noise powers at the input of the carrier tracking loop module.

The forms given in the above equations will be used to evaluate and improve the breadboard system performance. We do need some additional quantities described below.

5.2 Design Parameters and Constants

The previous sections developed mathematical tools necessary to study the noise rejection problem. The following constants and values will be used to the actual computations of the results.

(a) Thermal Noise Density:

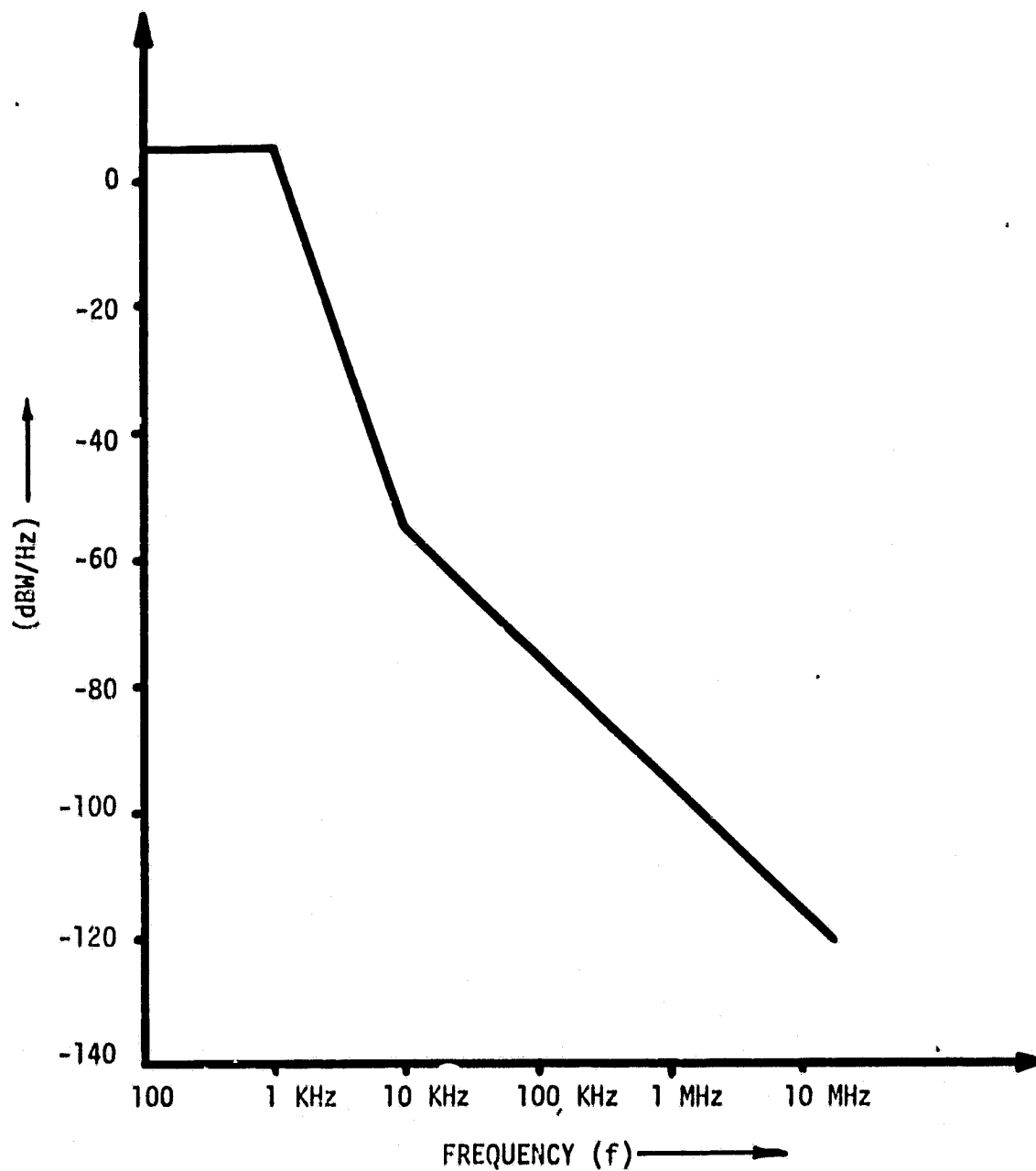Fig. 5.3. SUBARRAY NOISE CHARACTERISTICS.

$$N_0 = kT = .69 \times 10^{-20} \text{ watts/Hz}$$

Here k is Boltzmann's Constant and T is $500°K$.

(b) Spacetenna Subarray Transmitter Noise Characteristics:

$$\overline{A} = \sqrt{2P} \, e^{-\sigma_\theta^2}$$

$$S_A(f) = 4Pe^{-2\sigma_\theta^2} \alpha S_0(f)$$

where

P = Transmitter Power = 65 kw

σ_θ^2 = Transmitter Power Error Variance

= $.0305 \text{ rad}^2 \sim (10° \text{ rms})$

α = Variance-to-squared-mean ratio of the angular modulation

$\approx \sigma_\theta^2$

$S_0^2(f)$ = normalized phase error spectral density defined by

$$S_0(f) = \begin{cases} c, & |f| < 1 \text{ KHz} \\ c(f/10^3)^{-6}, & 1 \text{ KHz} < |f| < 10 \text{ KHz} \\ c \, 10^{-6}(f/10^4)^{-2}, & 10 \text{ KHz} < |f| \; . \end{cases}$$

c = normalizing constant = $(2.4 \times 10^3)^{-1}$

$S_A(f)$ in dB above 1 W/Hz is shown in Figure 5.3.

The basis for this spectral density comes from a Varian X-13 klystron tube phase noise sideband pwoer. The normalized phase noise sideband power spectral density (dBc/Hz) is shown in Figure
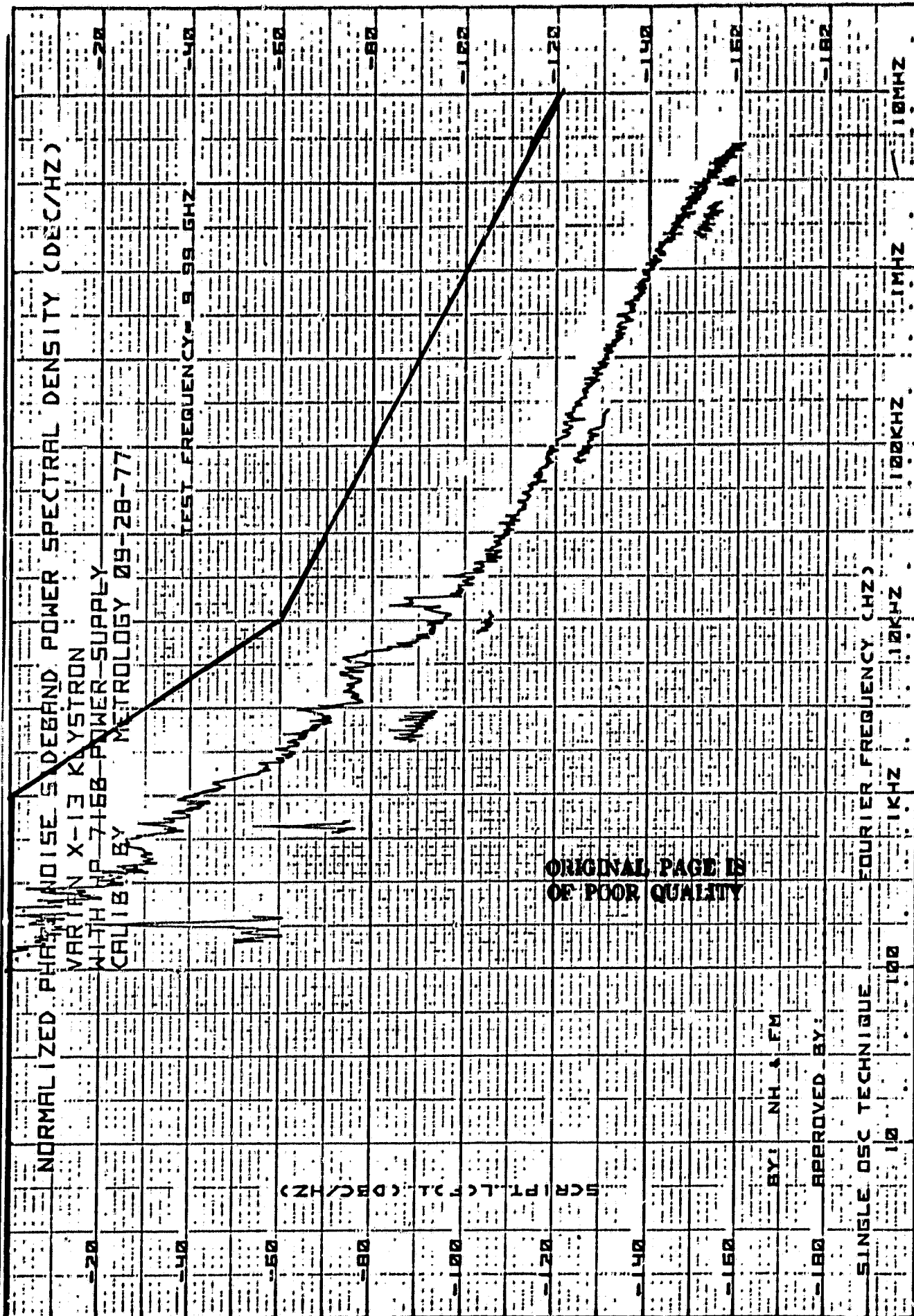
Fig. 5.4. Model for $S_\phi(f)/C$ Based on Varian X-13 Klystron.

LinCom

5.4 and the approximation to the actual sideband power is shown in the same figure which will be used as our basis for designing the system.

(c) Spectral density of spurious phase modulation on the uplink signal:

$$S_\phi(f) = \delta_D(f) \text{ (Dirac Delta Function)}$$

This is a reasonable approximation for interference computations.

(d) Chip rate:

$$T_c = 10^{-7} \text{ sec}$$

(e) The noncoherent-interference-coupling equivalent-baseband system function:

$$\sum_k |G_{kj}(f)|^2 < K_1 \text{ (constant)}$$

Here K_1 is an array design parameter.

(f) The coherent-interference-coupling equivalent-based system function:

$$|\sum_k G_{kj}(f)e^{j2\pi d_k(f_c-f)}|^2 < K_2 \text{ (A constant)}$$

Here K_2 is an array design parameter.
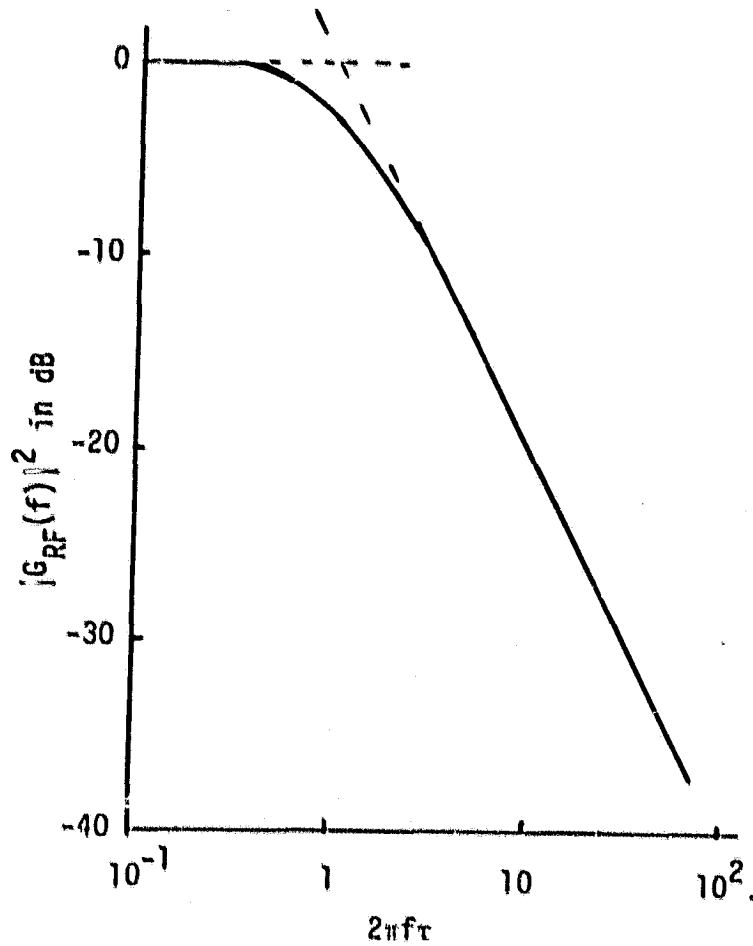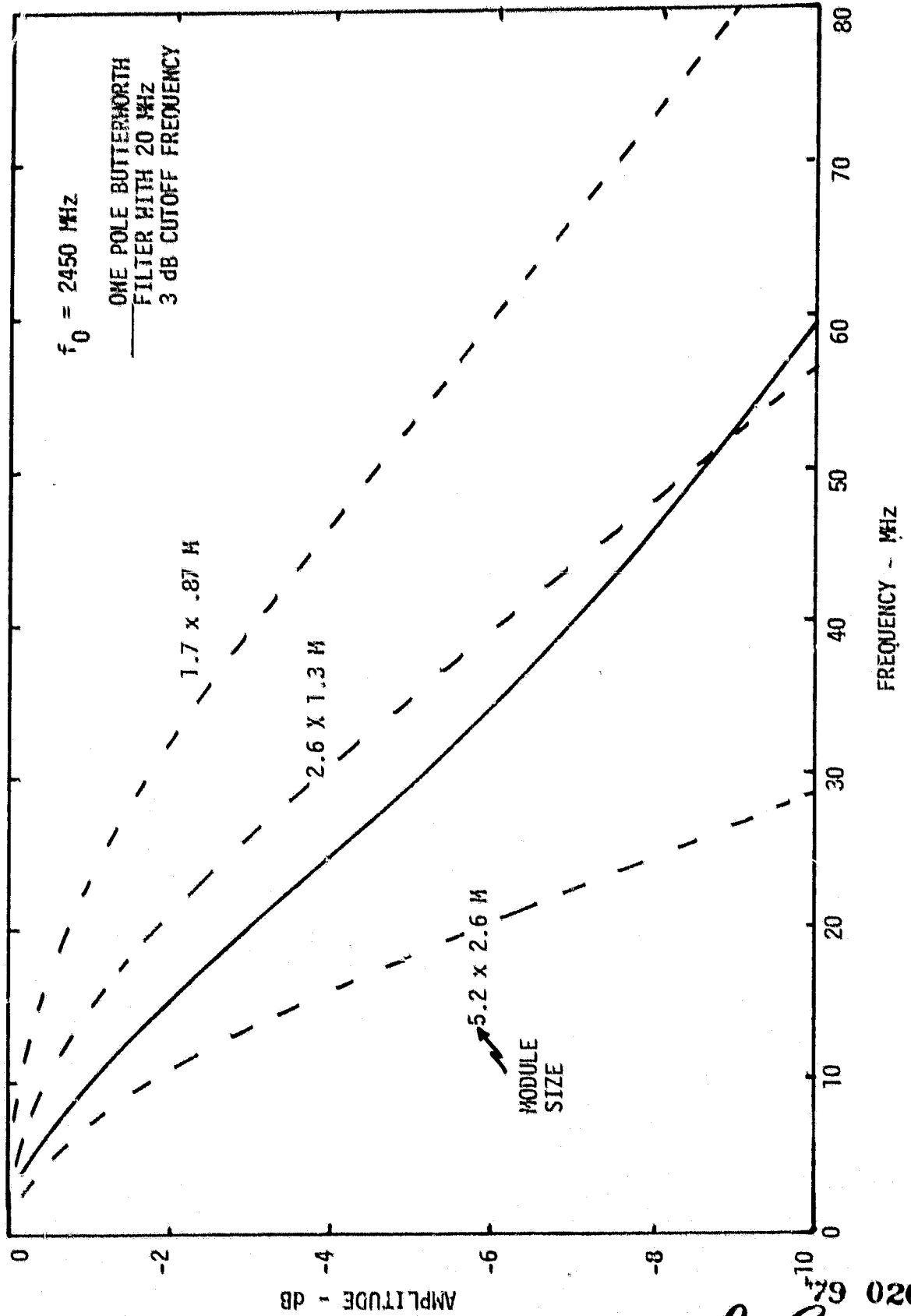
(f) The PN apparent tracking offset e is normalized in terms of chip times.

Fig: 5.5. -- The Assumed Power Response of the RF Filter.

Fig. 5.6.. Frequency Response of Half Module Radiator.

f_0 = 2450 MHz

ONE POLE BUTTERWORTH
—— FILTER WITH 20 MHz
3 dB CUTOFF FREQUENCY

1.7 x .87 M

2.6 X 1.3 M

5.2 x 2.6 M

MODULE
SIZE

FREQUENCY — MHz

AMPLITUDE — dB

$$\beta \triangleq \frac{e}{T_c}$$

The last parameter to be described is the filtering effect introduced by the subarray onto the impinging pilot signal. The baseband equivalent RF filter describing this effect would be

$$G_{RF}(f) = \frac{1}{1+j2\pi f\tau}$$

The time constant τ of this filter is normalized in terms of chip times to

$$\alpha \triangleq \frac{\tau}{T_c}$$

Note the 3 dB cut-off point for $G_{RF}(f)$ is $\frac{1}{2\pi\tau}$. Figure 5.5 is a sketch of $|G_{RF}(f)|^2$. The one-pole Butterworth filter characteristic has been chosen to conform with frequency response of half module radiator supplied by Boeing. A comparison is given in FIg. 5.6.

The above defines the RF filter necessary to predict the performance of the MPTX system accurately, however, for the performance of the breadboard system we may assume that the low pass filter does not exist, i.e., $G_{RF}(f) = 1$.

5.3 Design of the RF Front End Filter

In Chapter 2 we had enumerated all the interferences and noises degrading the performance of the MPTX system. Figure 5.7 shows the spectral density of the signal plus noise. This figure also shows the desired amplitude response of the front end filter. The filter is designed to pass the main lobe of the code modulation spectrum and

Fig. 5.7. SIGNAL AND NOISE SPECTRUM INTO MPTX TRANSPONDER

HALF 3 dB BANDWIDTH OF BASEBAND
EQUIVLANET NOTCH, F_0 = 30 MHz

CENTER FREQUENCY OF THE BANDPASS
FILTER IN THE BASEBAND-EQUIVALENT
SYSTEM, F_c = 40 MHz

3 dB BANDWIDTH OF THE FILTER = 20 MHz
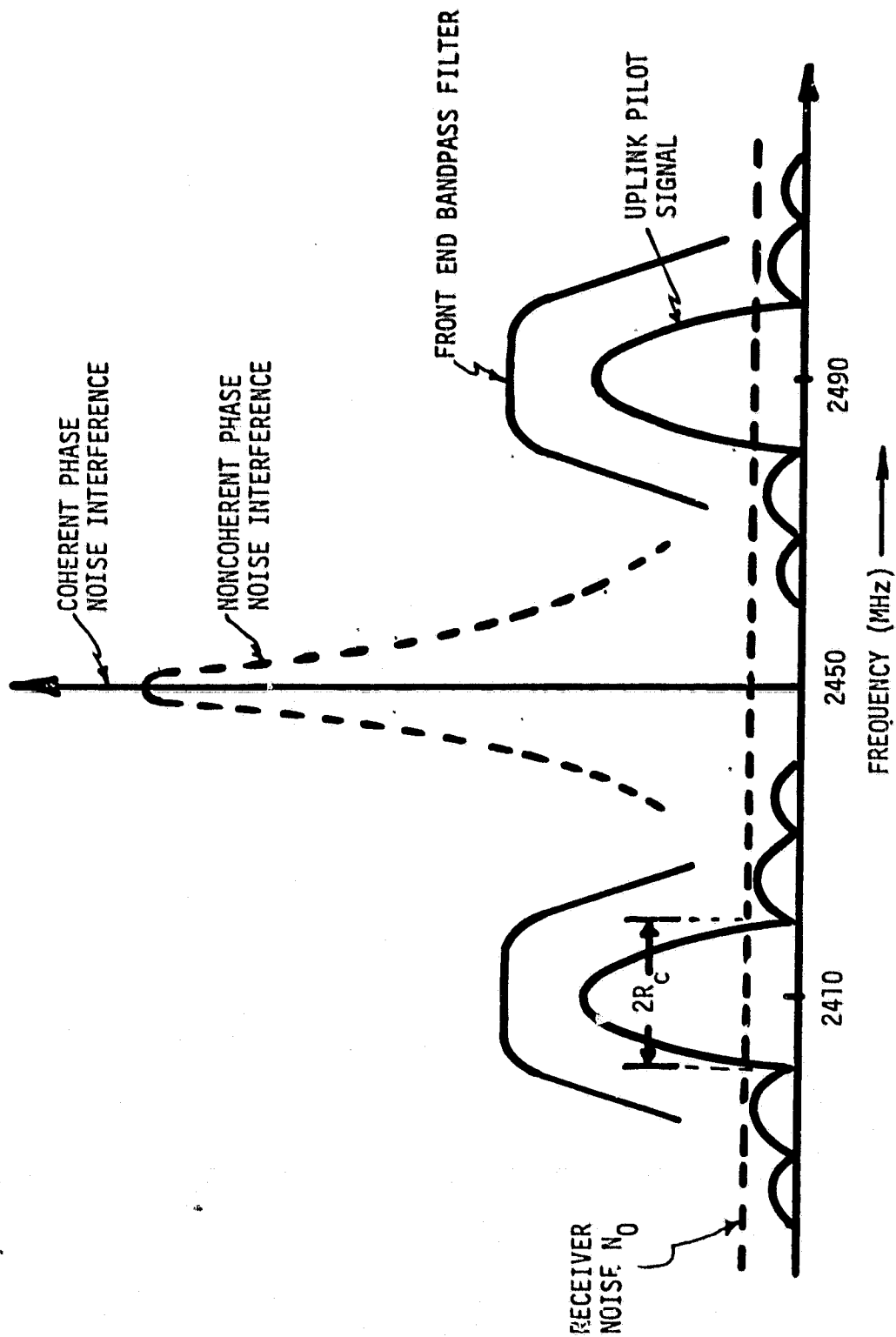
$$10 \log_{10}\left\{\frac{|H(f)|^2}{|H(f)|^2_{max}}\right\} dB$$
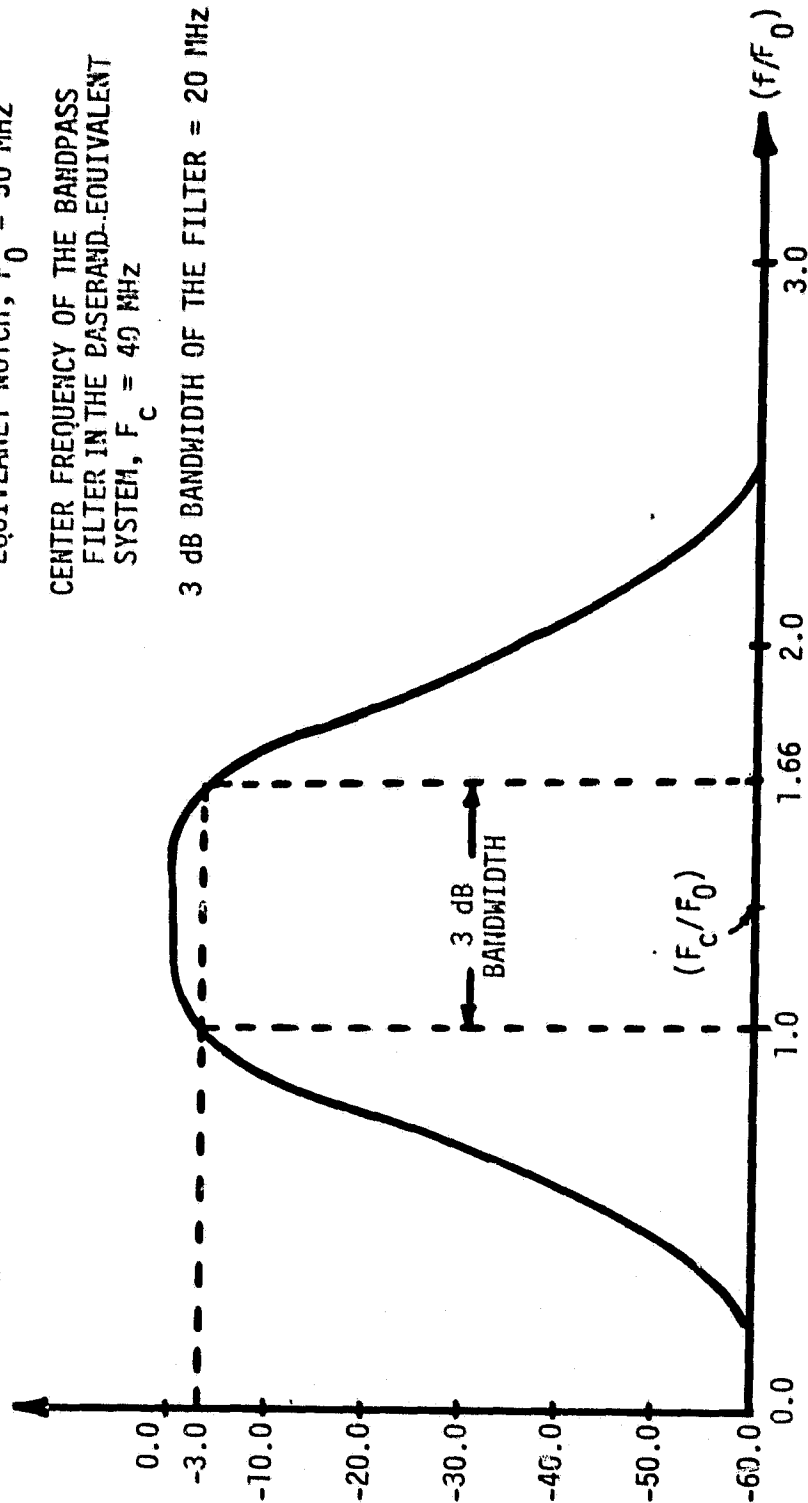
Fig. 5.8. BASEBAND EQUIVALENT OF THE BANDPASS FILTER

$$10 \log_{10} \left[\frac{\text{OUTPUT NOISE POWER}}{\text{OUTPUT NOISE POWER WITH NOTCH 3 dB BANDWIDTH} = 6\times10^7} \right] \text{dB}$$
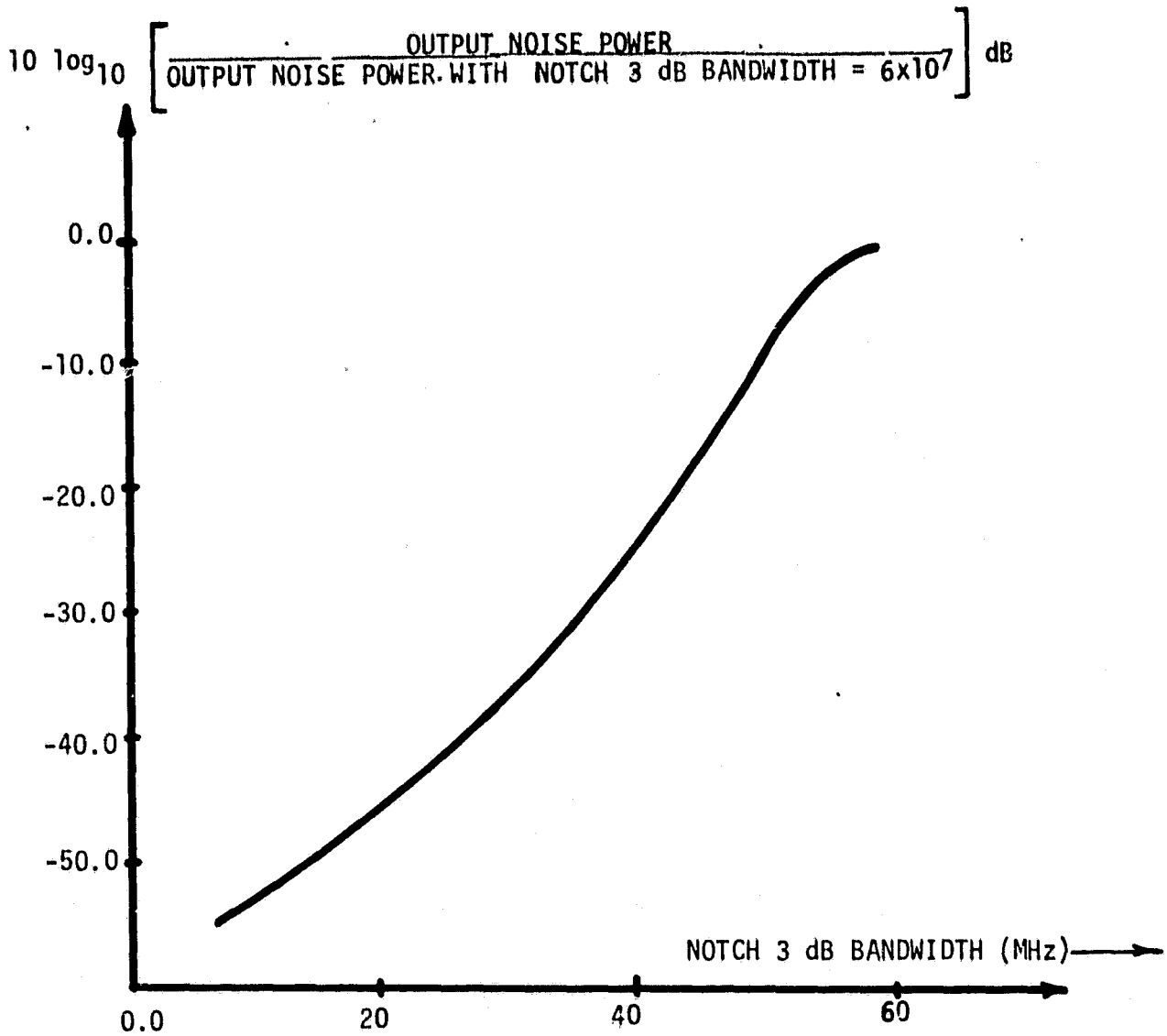

Fig 5.8b NOISE REDUCTION BY THE FRONT END FILTER

reject the coherent as well as noncoherent noises. Ideally the output of the front end filter would be the code modulation.

The baseband and equivalent of the RF front end filter is given by

$$G_1(f) = \gamma + \prod_{n=3}^{8} \left\{ \frac{1}{j\left[\frac{f-(F_c/F_0)}{(F_c/F_0)-1}\right] - e^{j[(2n+1)\pi/12]}} \right\} \quad (5.4-1)$$

This is a 6 pole Butterworth bandpass filter shifted to a frequency F_c = 40 MHz. (The subcarrier frequency.) Where F_0 is the half of the notch width. This notch is produced by the two bandpass filters around the subcarriers. A sketch of $|G_1(f)|^2$ against (f/F_0) is shown in Fig. 5.8. From the figure one can see that the three dB bandwidth of the filter is 20 MHz for a half gap width of 30 MHz. Thus the filter appears suitable for filtering the code modulation from the noise. Figure 5.8b shows the noise reduction due to the front end filter.

5.4 Carrier Tracking Loop Performance Measure

The main purpose of the carrier tracking loop is to track the carrier phase from the suppressed carrier pilot signal format and supply it to the phase conjugation circuit. The phase conjugation is a key issue in the retrodirective antenna scenario, hence it is just logical to assume the phase error of the tracking loop to be the performance measure of the carrier tracking operation. It is already known due to previous efforts that a total phase jitter of 10^0 can be allowed with no appreciable loss in the power transfer efficiency of the spacetenna, hence it would be desirable to know how much phase error is added by every possible source of phase error in the system towards the rms value of 10^0 of allowable phase error.

At the input to the carrier tracking loop the signal has three components: a term due to the carrier, a term due to the interference and a term due to the white noise. Both the noise terms introduce a phase error at the output of the carrier tracking loop. We will assume a worst case analysis, i.e., the carrier and the interference are in quadrature with each other. This would make the phase error to be

$$\sigma_\phi^2 = \frac{N_{eq}B_L}{P_R \cdot L_f} + \frac{J}{P_R \cdot 4}$$

N_{eq} is the equivalent noise entering the carrier tracking loop

B_L is the bandwidth of the carrier tracking loop

P_R is the received power in the uplink pilot

L_f is the loss factor introduced due to filtering

J is the power in the interference.

It should be noted that due to the passage of signal through nonperfect filters, the bit shape gets distorted and hence the code tracking loop output has to follow the distorted pulse shape to have maximum energy flow to the code tracking loop. In other words the 'S-curve' of the PN tracking loop will not be generally symmetric about zero. This fact has some design consideration attached to it for the code tracking loop. But as far as the carrier tracking loop is concerned, since the code rides on the amplitude of the carrier, phase tracking operation is relatively free of the errors in code tracking performance of the code loop.

Keeping the phase error as the performance measure, the following performance of the carrier tracking loop using the SOLARSIM is obtained.

Fig. 5.9. CARRIER TRACKING LOOP PHASE JITTER VS THE CHIP RATE.

CODE REPEATS AFTER 10,000 BITS

NULL OF THE FRONT END FILTERS = -60 dB

$$\frac{\text{FRONT END FILTER 3 dB BANDWIDTH}}{\text{CHIP RATE}} = 2$$

CHIP RATE (MHz) ⟶

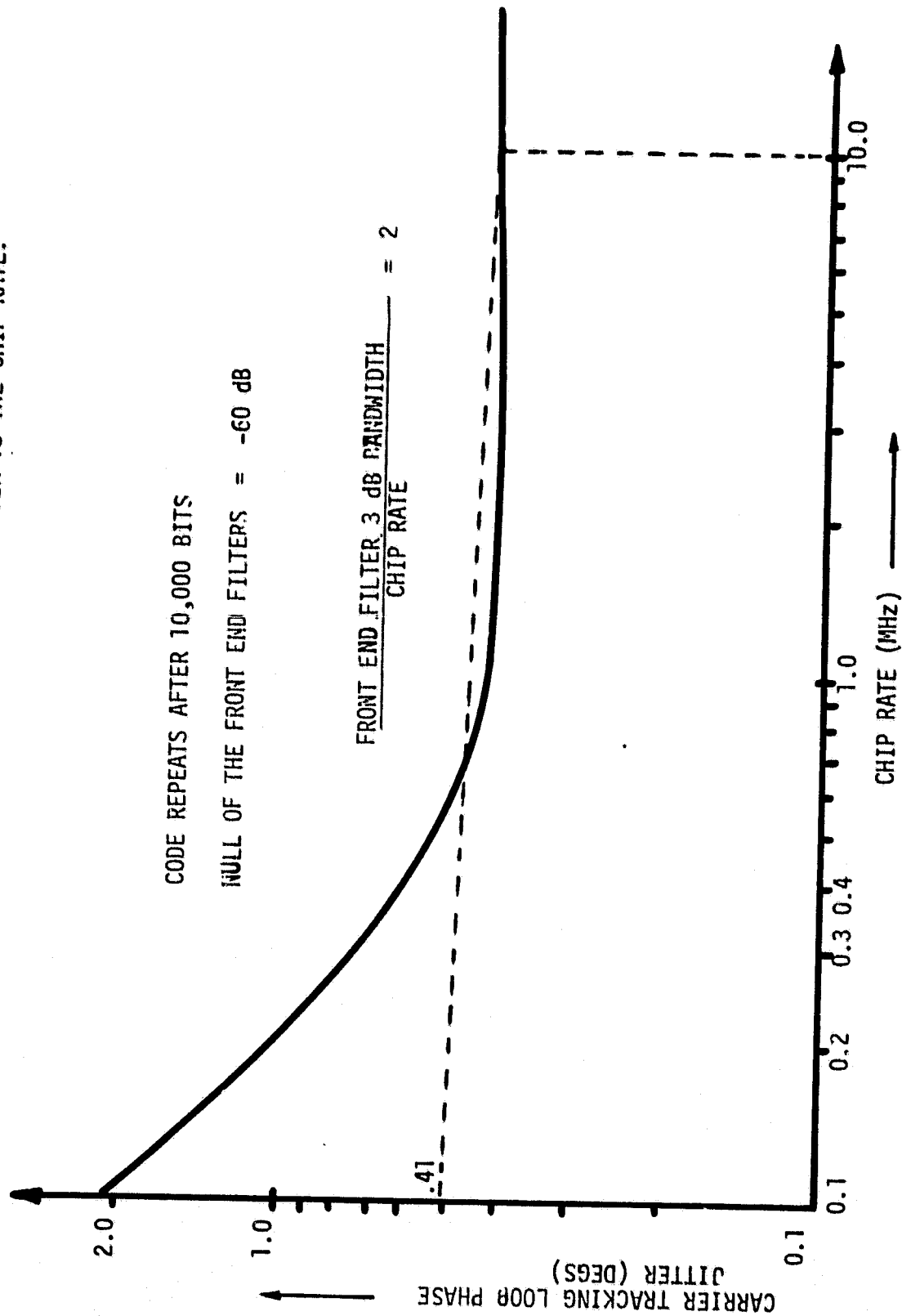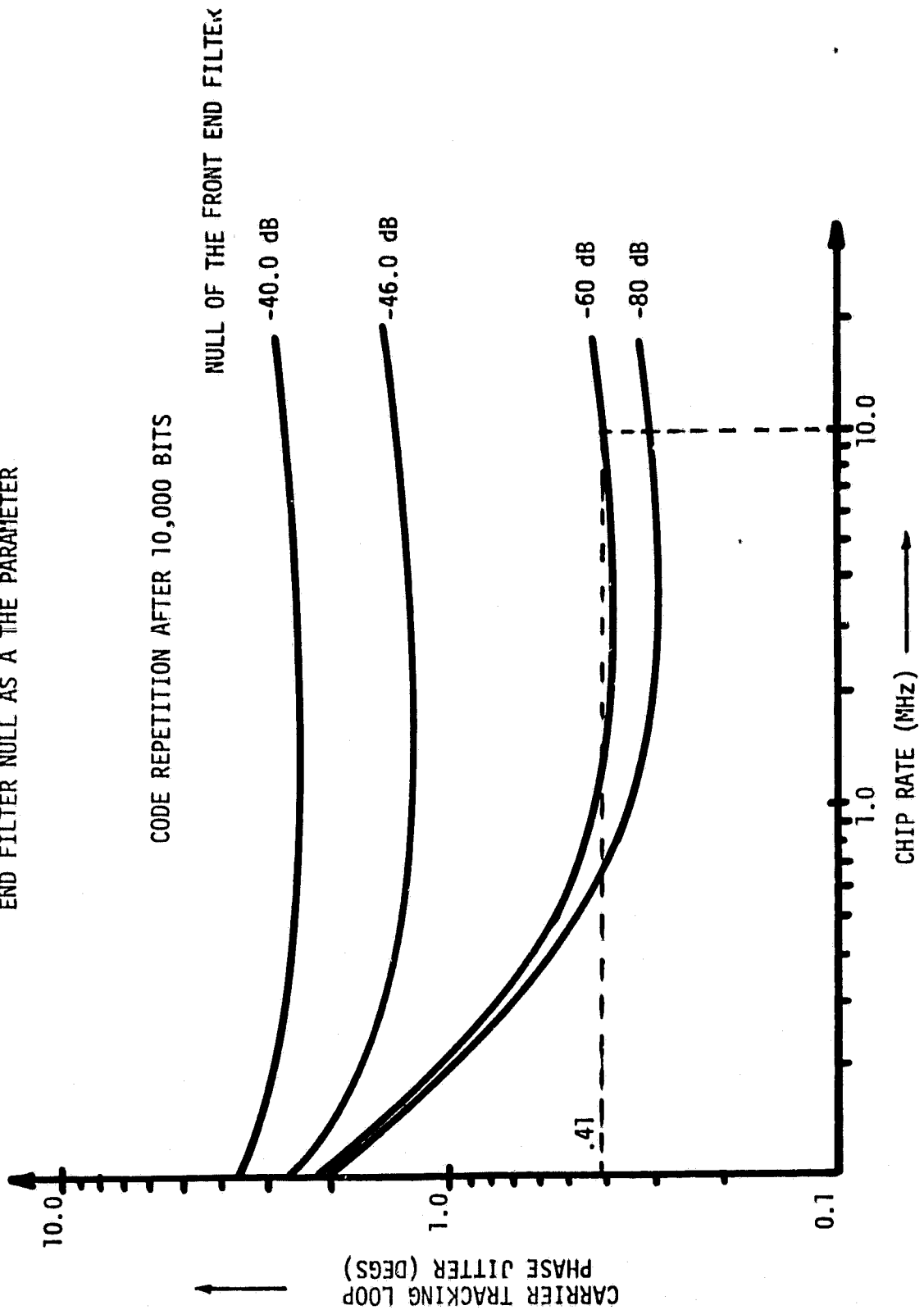CARRIER TRACKING LOOP PHASE
JITTER (DEGS)

LinCom

LinCom

Fig. 5.10. CARRIER TRACKING LOOP PHASE JITTER VS CHIP RATE WITH FRONT END FILTER NULL AS A THE PARAMETER

5.5 Performance Evaluation of Carrier Tracking Loop via SOLARSIM

A computer simulation of the MPTX system is developed to support the breadboard development of the system. This simulation is termed SOLARJIM. It has various inputs described below the effect of these parameter variations on the carrier tracking loop phase error characterizes the output of SOLARSIM. The various input parameters are:

- PN Chip Rate
- PN Code Period
- Uplink EIRP
- Notch filter (RF Front End Filter) Stop Band and Attenuation
- Carrier Tracking Loop Bandwidth

The following section describes the effect of the parameter variations on the carrier tracking loop phase error. Even though some parameters have a fixed value on the breadboard system, they are assumed to be variables and the values selected represent the operating point on the curves that follow.

Figure 5.9 is a plot of the carrier tracking loop phase jitter (the output parameter) vs the chip rate with the code repetition after 10,000 bits and the front-end filter set at -60 dB with the ratio of its 3 dB bandwidth to the chip rate equal to 2. (These are the design parameters of the breadboard system.) As the curve shows, the phase jitter of the tracking loop reduces or the chip rate increases and at 10 MHz, the operating point of the system, this becomes 0.4 degrees. As can be seen from this figure, the performance of the system starts degrading for higher values of the chip rate.

Figure 5.10 is a plot of the output parameter vs the chip rate with the null of the front-end filter as a parameter while it is assumed that
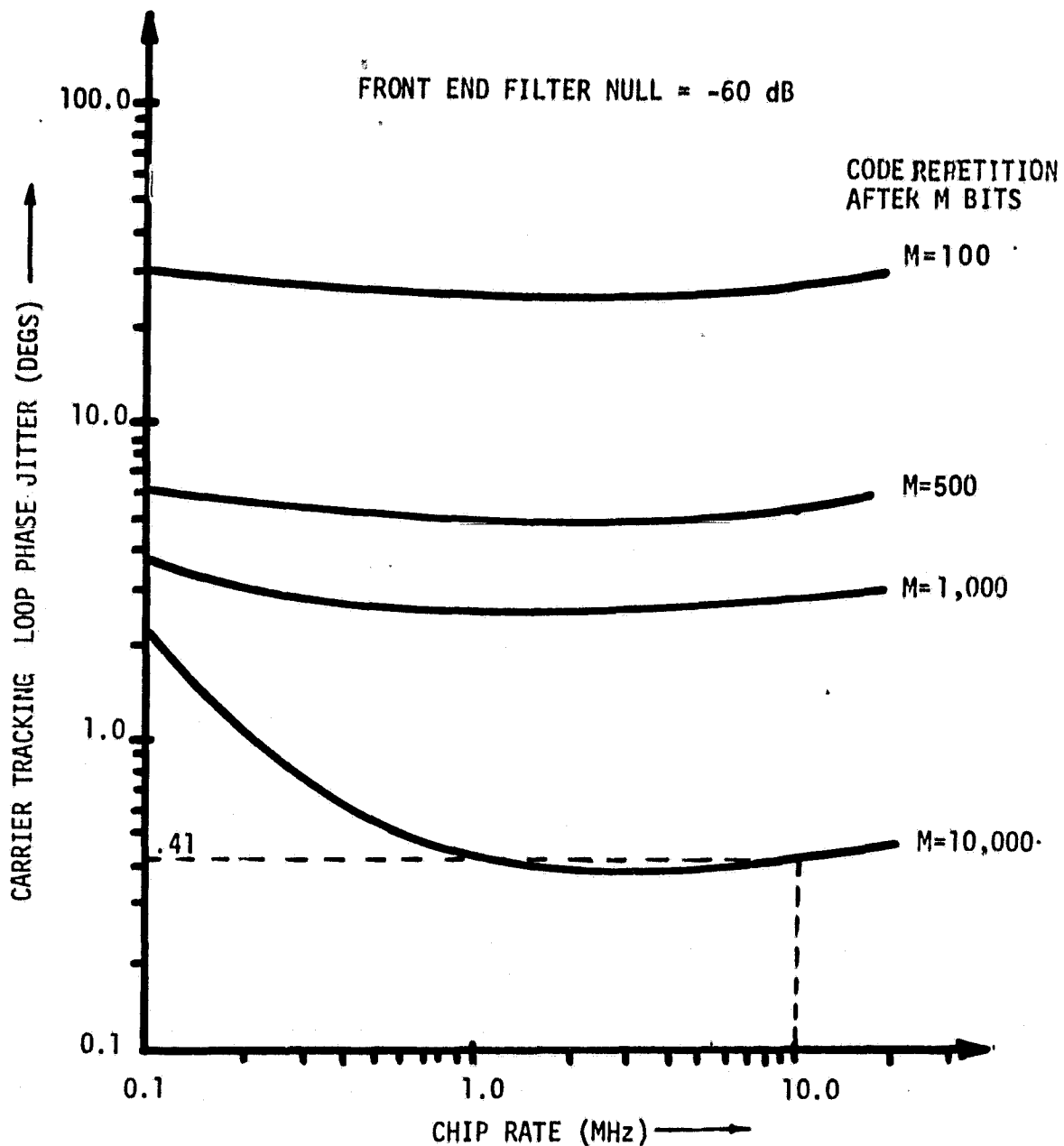
Fig. 5.11.   CARRIER TRACKING LOOP PHASE JITTER VS CHIP RATE
WITH CODE REPETITION FREQUENCY AS THE PARAMETER.

CHIP RATE = 10 Mbps

3 dB BANDWIDTH OF FRONT END FILTER = 20 MHz

CODE REPEATS AFTER 10,000 BITS
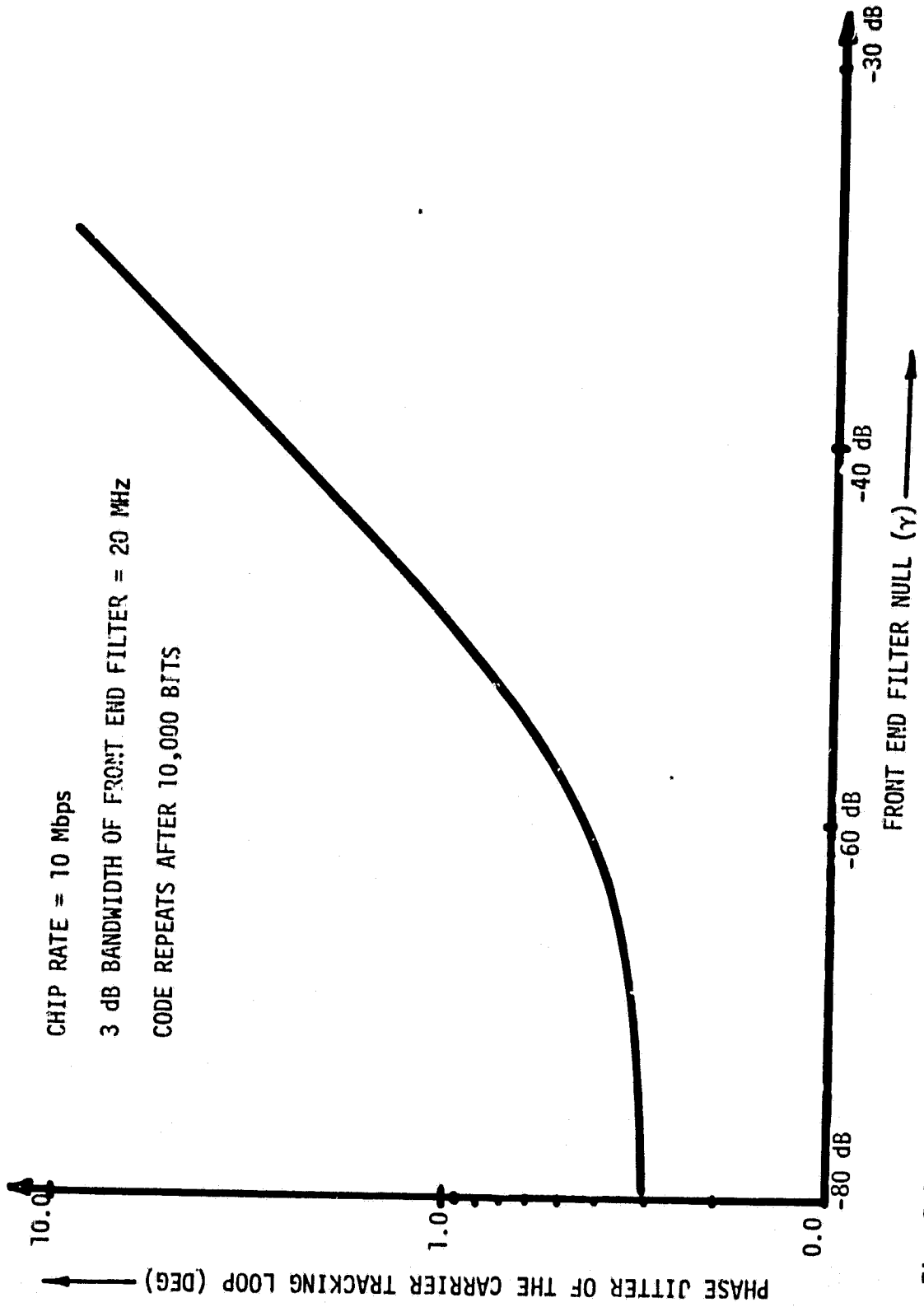
Fig. 5.12. PHASE JITTER OF THE CARRIER TRACKING LOOP VS FRONT END FILTER NULL.

FRONT END FILTER NULL (γ) ——►

PHASE JITTER OF THE CARRIER TRACKING LOOP (DEG)

LinCom

PHASE JITTER OF THE CARRIER TRACKING LOOP (DEG) ⟶

CHIP RATE = 10 Mbps

FRONT END FILTER NULL = -60 dB

CODE REPEAT AFTER 10,000 BITS

1.0

0.5
0.4
0.3
0.2
0.1
0.0

10   20   30   40 50   100

3 dB BANDWIDTH OF THE FRONT END FILTER (MHz) ⟶

Fig. 5.13.   EFFECT OF 3 dB BANDWIDTH ON THE CARRIER TRACKING
LOOP PHASE ERROR.

the code repeats after 10,000 bits. The curves indicate that as the filter attenuation increases, the phase jitter performance is improved. For the chip rate of 10 MHz the 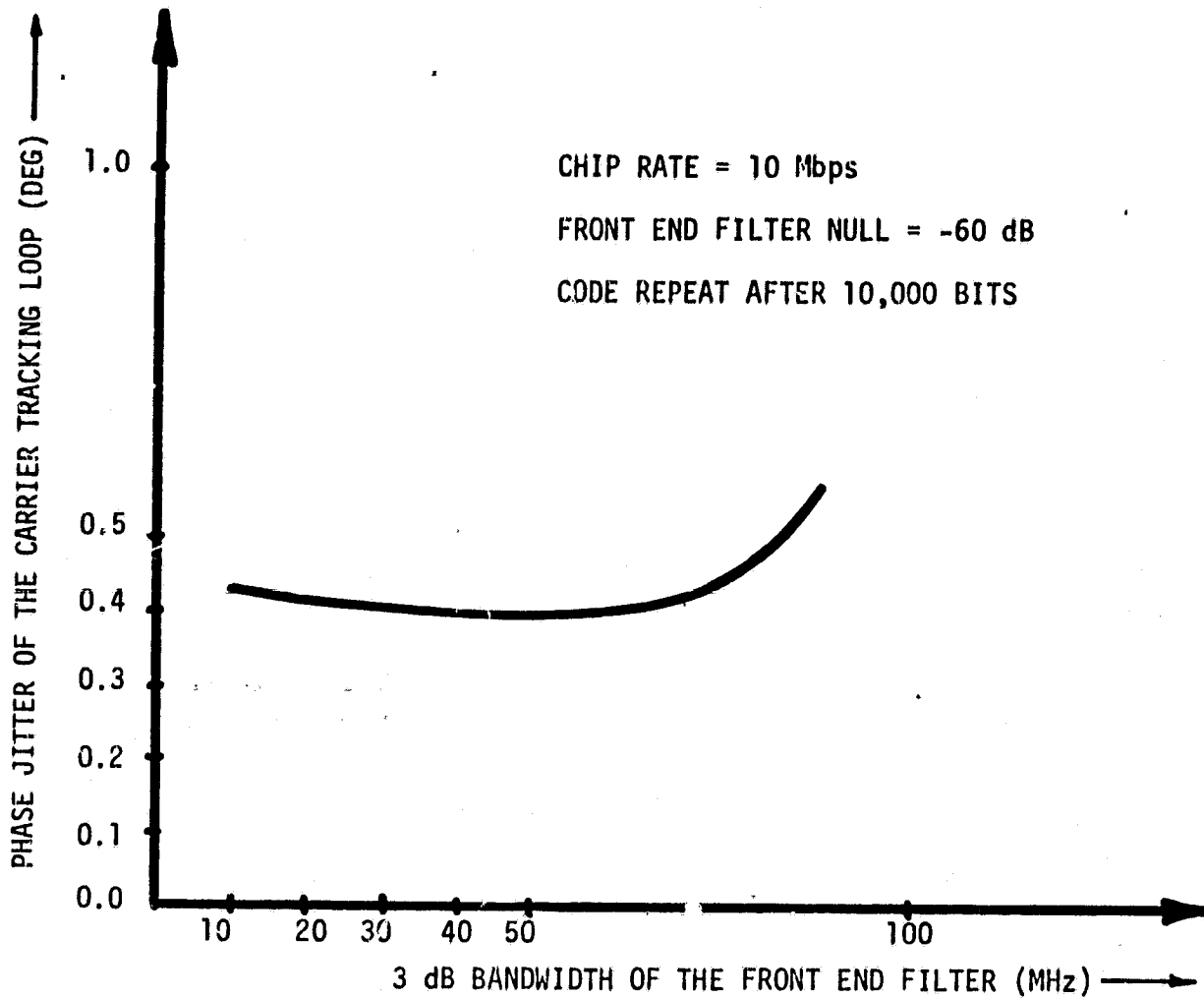noise contribution to the output parameter becomes negligible hence the performance does not increase appreciable with increasing the filter null. For the operating point we see that the phase jitter becomes 0.4 degrees.

The next figure, Figure 5.11, shows that the phase jitter performance improves as the PN code period M is increased. Here the value of the null is assumed to be -60 dB at the operating point, i.e., chip rate of 10 MHz, the phase jitter is 0.4 degrees as expected.

Thus we see that the front-end filter null plays an important role in the minimization of the tracking loop phase error. Fig. 5.12 plots the output parameter vs the front-end filter null with the rest of the parameters fixed at design values of the breadboard system. As expected, higher attenuation means better performance of the system but after the null of 60 dB the increase in the performance of the system is not appreciable with the increase in filter null, besides a greater null means an expensive filter; thus, it is logical to choose a null value which is cost effective yet meeting the performance requirement.

Figure 5.13 shows the effect of the 3 dB bandwidth of the front end filter on the phase jitter of the carrier tracking loop. From the figure one can see that 3 dB bandwidth of 20 MHz is pretty nearly optimal because any reduction in bandwidth loses the signal power and increase in the the bandwidth allows more noise to pass through the filter. Thus a 60 dB null, 6 pole Butterworth filter with 3 dB bandwidth of 20 MHz is quite adequate for the purpose.
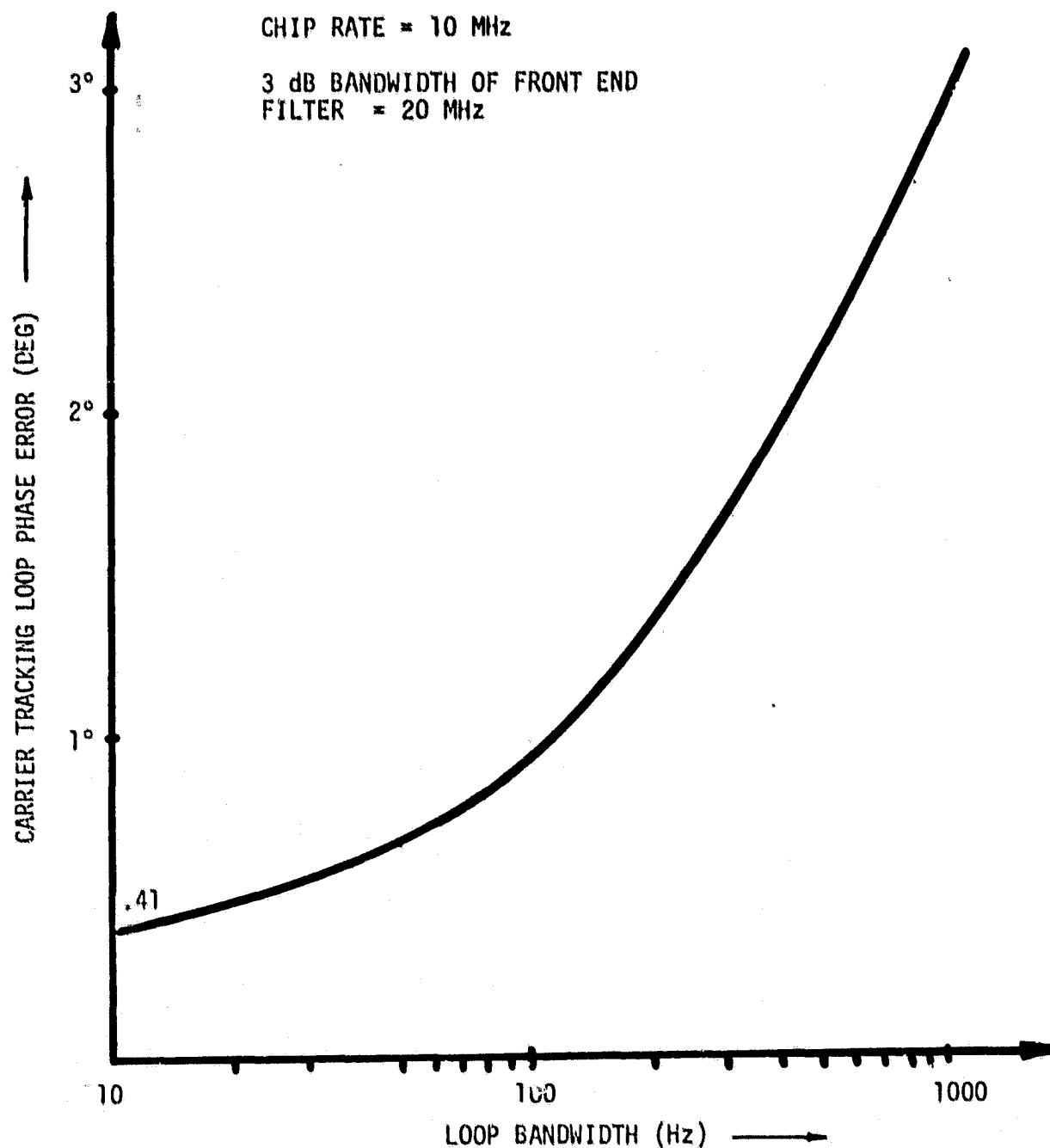
Fig. 5.14. PHASE JITTER OF CARRIER TRACKING LOOP VS THE PHASE TRACKING LOOP BANDWIDTH.

One more important carrier loop parameter is the loop bandwidth
Figure 5.14 shows the effect of the loop bandwidth on the carrier
tracking loop phase jitter. From this figure it seems that reducing
bandwidth is to our advantage, i.e., less phase jitter is passed by the
loop. This conclusion needs a little change when the phase noise added
by the VCO is considered. Larger fraction of this noise is passed by
the loop as the loop bandwidth is reduced. Thus the loop bandwidth of
10 Hz is picked as the design parameter and the VCO is assumed to
produce noise of 3° on the phase.

5.6 PN Tracking Loop

As mentioned earlier, there are two different sources of noise for
the MPTX system. The thermal noise and the coherent and noncoherent
noise due to the downlink power beam. At any typical pilot receiving
point these noises are assumed to be additive to the incoming pilot
signal. The signal plus noise passes through the front end filter
assembly which reduces the noise level by about 60 dB. The output of
the front end filter containing the signal and the passband noise is
then fed to the PN code tracking loop. The code tracking loop is a
tau-dither loop. Analysis for the theory of performance of the
tau-dither loop is well developed and documented in Ref. [5].

The main purpose of the PN tracking loop is to despread the
incoming pilot signal containing the PN code on the amplitude. It is
not designed for Doppler or range measurement. As such the tracking
error requirement is not very critical as long as it is limited to a few
percent of chip time.

PN acquisition will take time from a "cold start," i.e., when the
local PN clock is not running. This can occur, for example, when the

system is powered on initially. In that case, the local clock has to step over all possible code states during acquisition. However, once the local clock starts running, it should be almost synchronous with the ground code due to the almost nonexistent channel Doppler. If the local clock is left running when the system is brought down for whatever reasons, the latter can be brought back up using the local clock. No additional acquisition algorithm is required.

Since all power transponders are experiencing the same Doppler for all practical purposes, a way to cut down the acquisition time and individual acquisition hardware requirement is to include a separate telemetry receiver that tracks the uplink pilot. This pilot signal is constantly tracked by the telemetry receiver and the state of the PN clock can be transferred to the individual transponders to start the PN loops. In this case, no acquisition aid on the transponders are required. However, data links between the telemetry receiver and the transponders must be established.

In the reference system, a τ-dither loop is used to avoid the gain imbalance problem commonly found in the standard delay-lock loop implementation. The various noises are described in the previous chapters. These noises after passing through the front end filter has the form

$$S_N(f) = [N_0 + K_1 S_A(f) + K_2 \overline{A}^2 \delta(f)]|H_1(j2\pi f)|^2 \quad (5.7-1)$$

where

N_0 = the white noise added to the system

$S_A(f)$ = The power spectral density of the noncoherent

noise due to the downlink power beam

$\overline{A}^2$ = the magnitude of the coherent noise due to the power beam

K_1, K_2 = array design parameters affecting the noncoherent and

coherent noise inputs to the system respectively

$|H_1(j2\pi f)|$ = the amplitude response of the front end filter

assembly

one can develop an expression after considerable manipulation for the

normalized tracking error σ_t/Δ. Where Δ is the PN chip time

$$\left[\frac{1}{2} S \cdot S_n(0)|H_\ell(0)|^4 + f_{3dB} \int_{-B_i/2}^{B_i/2} S_n^2(xf_{3dB})|H_\ell(x)|^4 df \right.$$

$$+ 2f_{3dB} \sum_{\substack{n=1 \\ n=odd}}^{2T_d f_{3dB}} \left(\frac{2}{n\pi}\right)^2 \int_{-1+\frac{n/T_d}{f_{3dB}}}^{1} S_n(xf_{3dB}) S_n(-xf_{3dB}+\frac{n}{T_d})|H_\ell(-x+\frac{n}{T_d})|^2 dx$$

$$+ \frac{1}{2} S \cdot 2 \sum_{\substack{n=1 \\ n=odd}}^{2T_d f_{3dB}} \left(\frac{2}{n\pi}\right)^2 S_n(\frac{n}{T_d})|H_\ell(\frac{nT_d}{f_{3dB}})|^2 |H_\ell(0)|^2 \Big]$$

$$\overline{\left[\frac{S^2}{B_L} - \frac{1}{2} \cdot S \cdot S_n(0)|H_\ell(0)|^2 - \frac{1}{2} \cdot S \cdot \sum_{n=1}^{2T_d f_{3dB}} \left(\frac{2}{n\pi}\right)^2 S(\frac{n}{T_d}) \cdot |H_\ell(\frac{n/T_d}{f_{3dB}})|^2 |H_\ell(0)|^2\right]}$$

where

$|H_\ell(x)|^2$ = the amplitude response of the low pass equivalent
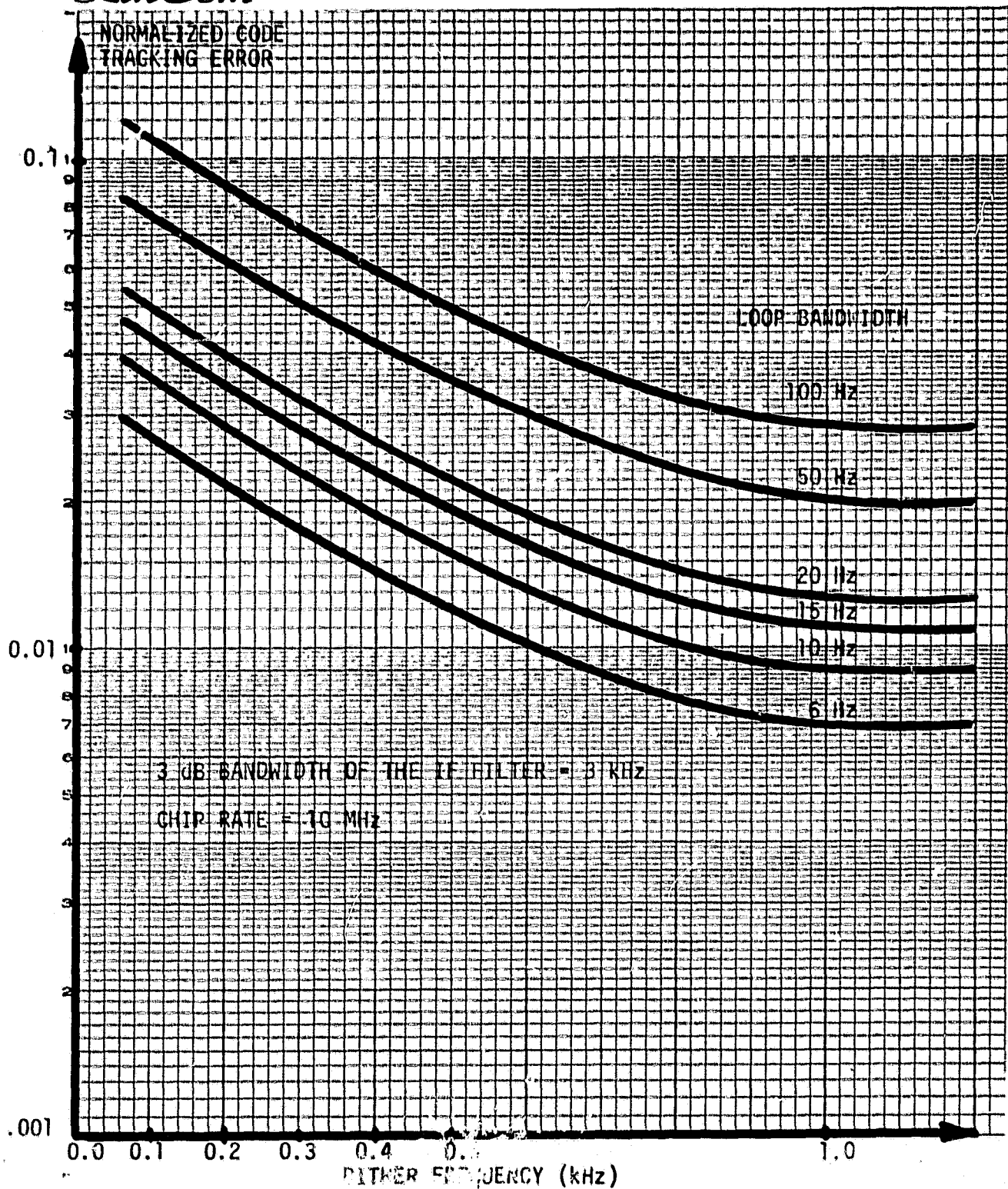
of the arm filter

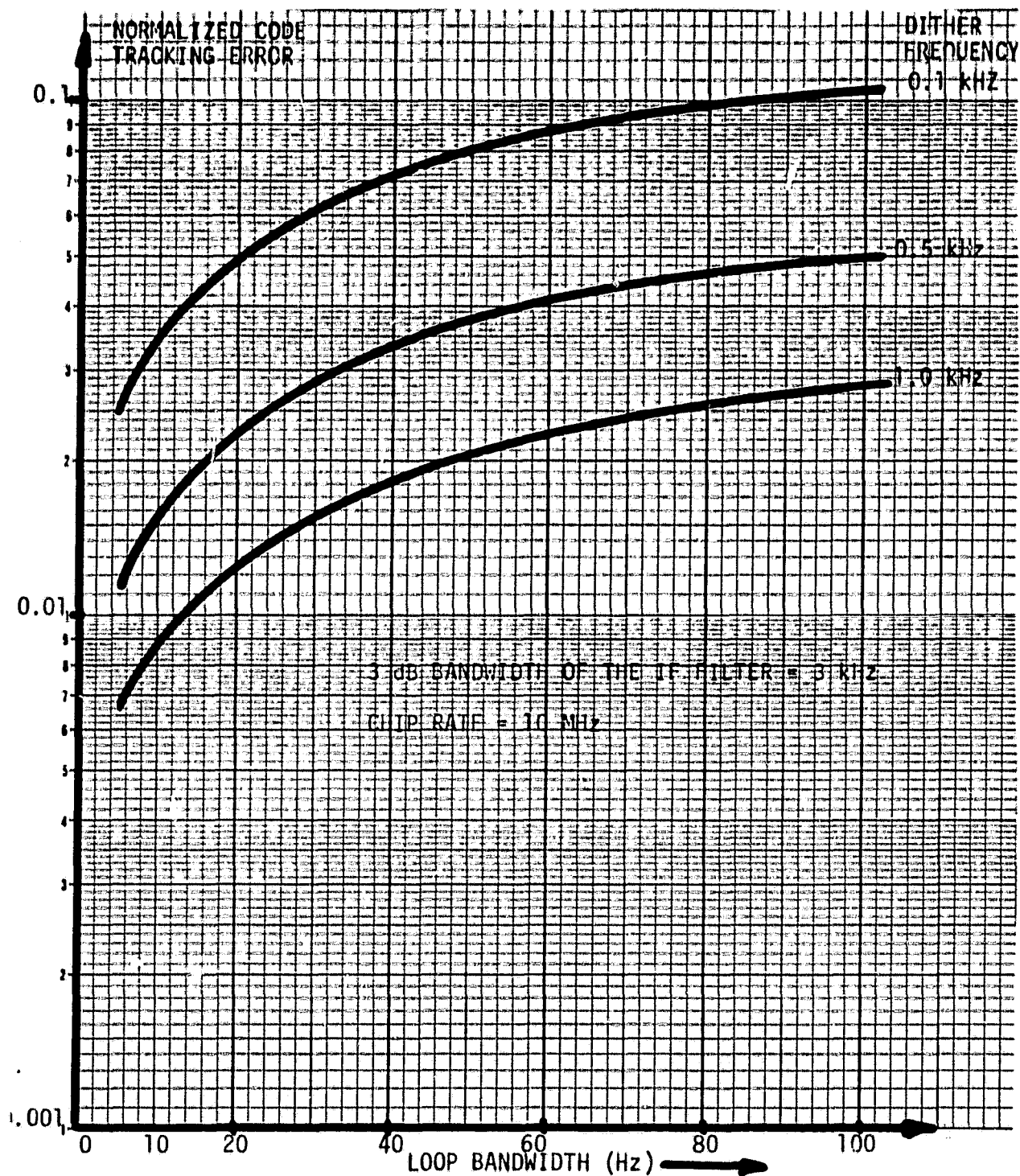Fig. 5.15. EFFECT OF DITHER FREQUENCY ON THE CODE TRACKING LOOP ERROR.

Fig. 5.16. EFFECT OF LOOP BANDWIDTH ON THE CODE TRACKING LOOP ERROR.

T_d = the dither chip time

f_{3dB} = the 3 dB frequency of the $H_\ell(x)$

B_L = the loop bandwidth of the code loop

5.7 Performance Evaluation of the PN Code Tracking Loop

The PN code tracking loop is simulated, on the JSC Univac computer and is a part of a computer package called SOLARSIM. There are two parameters in the loop which hae paramount importance as far as the performance of the code loop is concerned. These are the loop bandwidth and the dither frequency. The output parameter is the code tracking error normalized by the code chip time.

Figure 5.15 shows the effect of changing the dither frequency on the code tracking error. As can be seen from the figure, with a tracking loop bandwidth of 10 Hz and the dither frequency of 1 kHz the tracking error is less than 1% of the chip time provided that the 3 dB bandwidth of the arm filter is 3 kHz. Figure 5.18 shows the variation of the normalized tracking error with respect to the loop bandwidth and the dither frequency being the parameter. Here too, the same IF filter characteristic was used.

It should be noted that the code modulation resides on the amplitude of the carrier signal hence any small error in code tracking does not affect the phase tracking operation of the carrier tracking loop directly. In other words, error in despreading the carrier does not affect the phase of the carrier as long as the error is small. The front end filter reduces the incoming disturbing noise by about 60dB. This allows the code tracking loop to operate very efficiently by effectively reducing the code tracking error to a small quantity.

6.0 THE POWER AMPLIFIER

Even though each ocmponet in the SPS transponder is liable to introduce noise to the downlink power beam phase, the noise added by the klystron amplifier is by far the greatest. Hence some special noise reduction technique is needed for the power amplifier. Figure 5.4 shows the normalized phase noise sideband power spectral density of a Varian X-13 klystron tube which we have deemed appropriate to be our klystron model.

The components of the Klystron phase noise around the carrier frequency of 2.45 GHz can be tracked by the phase locked loop around the klystron amplifier. With the loop around the klystron, the relevant tracking equations for he PA phase control loop become

$$\phi_A = (1-H)\theta_0 - (1-H)(\psi_A + N_A) \tag{6.1}$$

$$\theta_{out} = H\theta_0 + (1-H)(\psi_A + N_A) \tag{6.2}$$

Where ϕ_A is the amplifier loop phase error, ψ_A is the PA (klystron) phase noise, ψ_A models the VCO/mixer phase noise input to the loop. θ_{out} is the single most important quantity modeling the phase error process at the output of the transponder and it directly affects the efficiency performance of the SPS transponder.

As mentioned before, the components of PA phase noise can be tracked by the VCO. With the loop around the klystron, only phase noise components which have Fourier frequencies greater than the loop bandwidth B_L will be transmitted. Noise components below this frequency will be suppressed by a factor of $1-H(s)$ where $H(s)$ is as defined in the
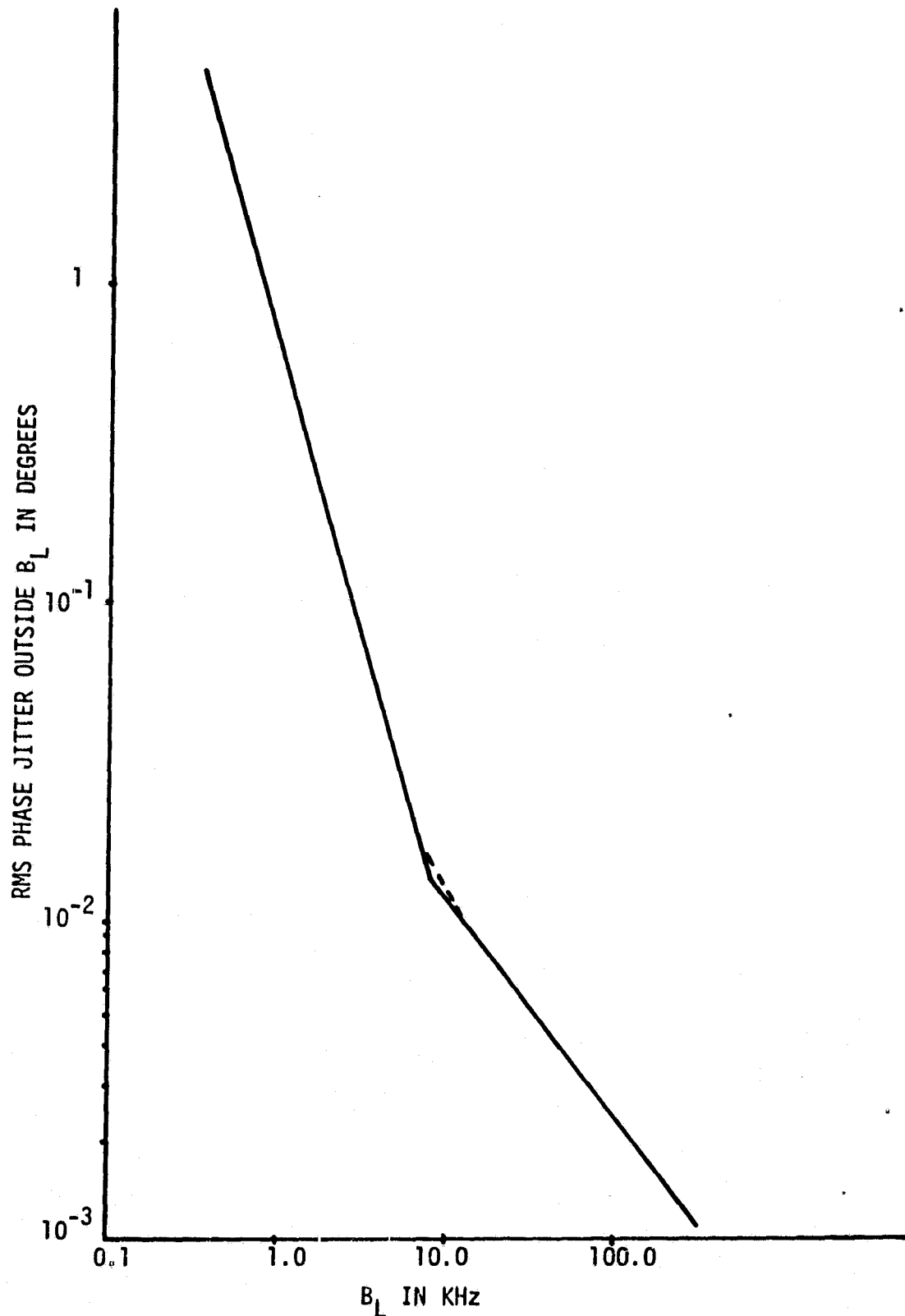
Fig. 6.1.   A PLOT OF RMS KLYSTRON PHASE NOISE OUTSIDE A
BANDWIDTH B_L.

above equations. Assuming an ideal loop transfer function, i.e.,

$$H(f) = 1 \qquad |f| < B_L$$

$$= 0 \qquad elsewhere$$

We can predict the amount of phase noise leakage through the transmitter. Figure 5.3 shows the noise profile (spectral density) for the klystron and the noise passing through the amplifier tube is depicted in Figure 6.1. It should be noted that for this diagram no other noise inputs to the amplifier are considered. From Figure one can see that for a B_L = 10 kHz, the phase jitter of the output phase due to noise leakage is about 0.1^O and with B_L = 0.5 kHz the phase jitter becomes 5°.

Since the amplifier is not operating in solitude, i.e., there are other noise inputs present from various sources such as the carrier tracking loop, hence opening up B_L will not reduce the phase jitter after some point. Thus the loop bandwidth for the power amplifier loop will be selected such that the output phase error does not exceed a maximum of 5°. Error in excess of 5° will degrade the power transfer efficiency of the SPS considerably.

7.0 PHASE ERROR BUILD UP BUDGET AND POWER TRANSFER EFFICIENCY

The topic of SPS Power Transfer has been dealt within great details in our previous report, hence here we will only mention it briefly stressing these areas where more results are found. The spacetenna is assumed to be a stepped approximation to a circle of diameter 1 Km, having an area of 0.76×10^6 mt^2. This area is subdivided into what are
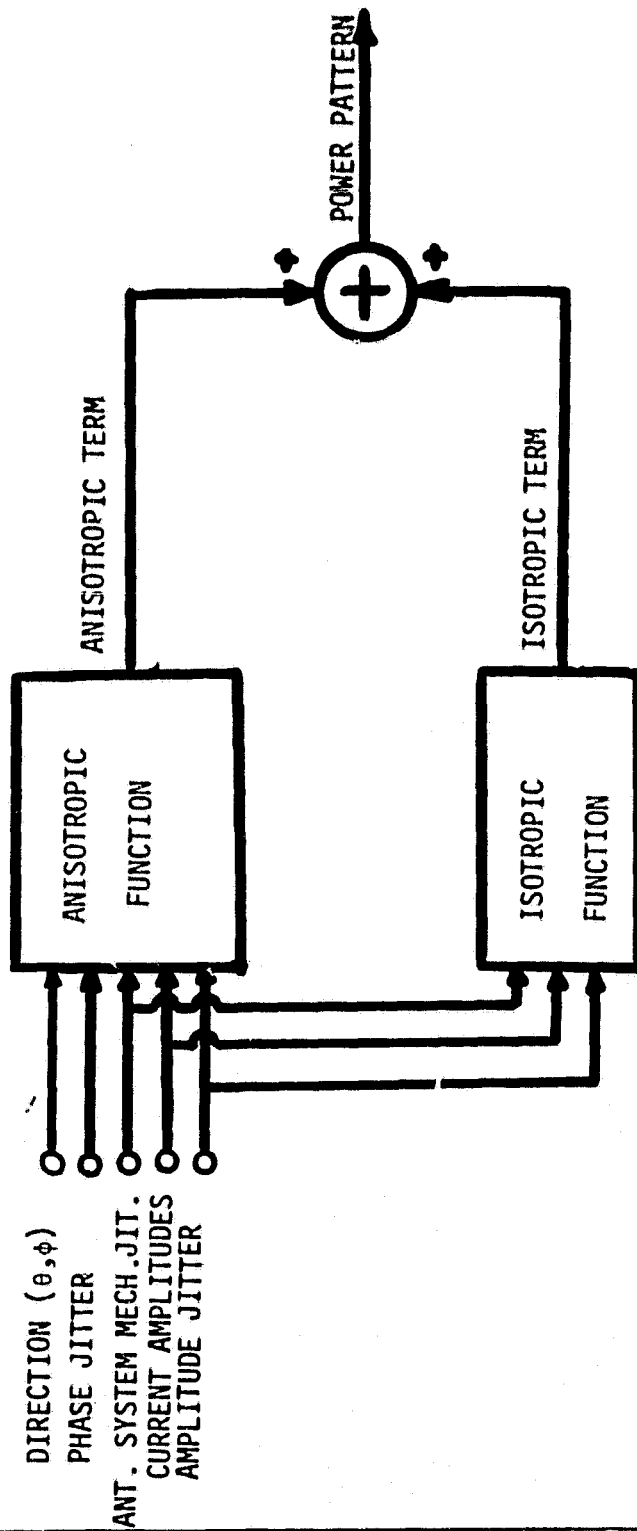
Figure 7-1. Components of the Average Power Pattern.

called the subarrays. These subarrays are not of the same size. Each subarray is fed by a single power amplifier and actual radiating elements in the subarrays are the slotted waveguides. Conjugation of the received pilot phase is done at each power amplifier tube with the help of a constant phase supplied by the phase distribution system. This conjugated phase is used to produce retrodirective power wave.

The actual radiating elements are the slots cut in the waveguides (slots are separated from each other by a distance of $\lambda/2$, where λ is the wavelength of the waves in the waveguide). The pattern multiplication principles tells us that the radiation pattern of spacetenna is the multiplication of the element pattern of the radiating elements and the array factor (based on the location of the radiating slots) of the antenna. Array factor of the antenna remains the same regardless of the nature of the radiating elements. The array factor of the spacetenna has a very highly peaked mainlobe having a 3 dB beamwidth of a few tenths of a minute of arc which is comparable to the angle subtended by the rectenna at the spacetenna center. The element factor of the slot is so flat around the boresight for several minutes of arc that the region of interest (the 3 dB beamwidith region) this factor could be approximated by a constant. Hence the radiation pattern of the spacetenna in the region of interest, could be approximated by considering isotropically radiating elements instead of the slots. The spacetenna power pattern using the above approximation has two main parts comprising it. One part depends on the direction (θ, ϕ) which will be called the anisotropic term and the other part independent of (θ, ϕ) will be termed the isotropic part, i.e., (see Figure 7.1)
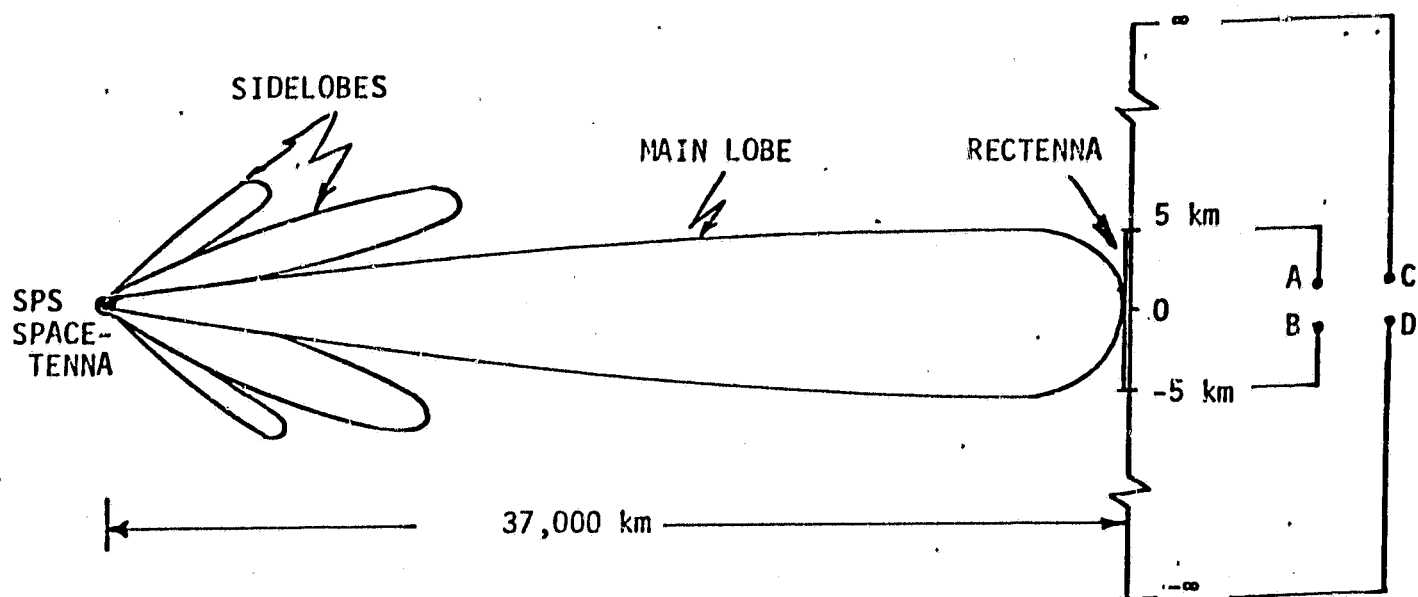
SIDELOBES

MAIN LOBE

RECTENNA

SPS
SPACE-
TENNA

5 km

0

-5 km

A

B

C

D

37,000 km

Figure 7.2. Geometry of the Power Pattern.

Averaged
Power $\triangleq$ $E(f\ f^*)$ = Anisotropic Term + Isotropic Term
Pattern

The spacetenna averaged power pattern takes into account all the system imperfections in the form of jitters. The isotropic term is a function of independent phase disturbances at the slot level. It should be noted that the isotropic term comes into existence only if the phase disturbances at the slot level are statistically independent, e.g., the location jitter on the radiating slots this does not include, for example, the phase disturbance added by the phase distribution system because all the slots in the subarray are affected by the same phase disturbance. One more fact may be pointed out that if the slot element pattern used in the computation, the only change is that the isotropic term becomes directional due to the element pattern and the total power due to this term reduces by the gain factor (of the slot) from the total power radiated by the isotropic term.

The power transfer efficiency of SPS is defined as follows

$$\text{POWER TRANSFER EFFICIENCY} = \frac{\text{Power Received by the 10 Km Diameter Rectenna}}{\text{Total Power Radiated by the Spacetenna}} \tag{7.1-1}$$

Figure 7.2 makes the idea clear. The power transfer efficiency can be redefined as

$$\text{POWER TRANSFER EFFICIENCY} = \frac{\text{Power Output at Terminals A \& B}}{\text{Power Output at Terminals C \& D}} \tag{7.1-2}$$

This definition is convenient because the multiplying constants due to one can show that

$$\text{RECEIVED POWER} = \iint\limits_{\theta,\phi \in R} \text{(anisotropic term)} \sin\theta \, d\theta \, d\phi$$

$$\text{(7.1-3)}$$

$$+ \text{(isotropic term)} \iint\limits_{\theta,\phi \in R} \sin\theta \, d\theta \, d\phi$$

where R is the region of the rectenna (see Fig. 7.1), and

$$\text{THE TOTAL RADIATED POWER} = \iint\limits_{H} \text{(anisotropic term)} \sin\theta \, d\theta \, d\phi$$

$$\text{(7.1-4)}$$

$$+ \iint\limits_{H} \text{(isotropic term)} \sin\theta \, d\theta \, d\phi$$

substituting these two equations in (7.1-2) yields the power transfer efficiency of the SPS.

7.1 Effect of System Imperfections and the Phase Error Budget

As discussed in pervious reports, the power transfer efficiency has to contend with two types of errors which are: (1) errors arising due to spacetenna electrical components and (2) errors arising due to mechanical constructional faults of the spacetenna. These two categories are tabulated in the sections below.

Errors (jitters) due to Electrical Components

1) Phase jitters produced by the spread spectrum receiver.

2) Phase jitters due to the reference phase distribution system (MSRTS).

3) Phase jitters and amplitude jitters due to power amplifier circuitry.

As mentioned in the earlier chapters, the spread spectrum receiver has two major areas of phase errors they being (1) the code tracking
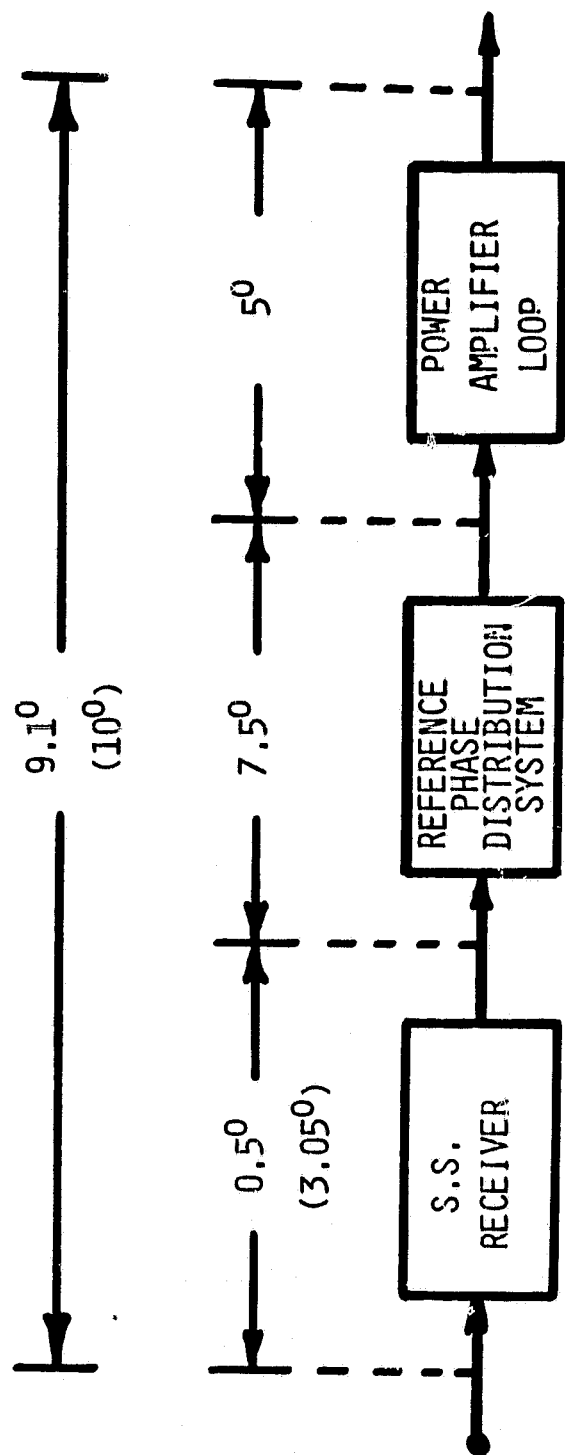
Fig. 7.3. PHASE ERROR DISTRIBUTION OF THE ENTIRE SYSTEM

PILOT TRANSMITTER	IONOSPHERE	PHASE DISTRIBUTION SYSTEM (MSRTS)	SPREAD SPECTRUM RECEIVER	HIGH POWER AMPLIFIER	IONOSPHERE
•PILOT TRANS- MITTER VCO JITTER = 1°	•REFRACTIVE SCATTERING •REFLECTIVE SCATTERING •UNDERDENSE HEATING	•PILOT RCVR VCO JITTER (3°) •POWER SPLITTER IN PHASE DISTRIBUTION TREE (6°) •PHASE JITTER OF VCO's IN THE PHASE DISTRIBU- TION TREE (2.4°) •UNCOMPENSATED PATH DELAY (2.4°)	•PHASE JITTER DUE TO CARRIER TRACKING LOOP 0.5° •PHASE JITTER DUE TO CODE TRACKING LOOP DUE TO NOISE •PHASE JITTER DUE TO VCO IN THE LOOPS (3.0°)	•PHASE JITTER DUE TO THE HPA STABILIZATION LOOP (5°)	•IONOSPHERE OF DOWNLINK POWER BEAM
PHASE JITTER 1°	PHASE JITTER 3°	RMS PHASE JITTER = 7.5°	RMS PHASE JITTER = 3°	PHASE JITTER 5°	PHASE JITTER 0°

TOTAL RMS PHASE JITTER = 10°

POWER TRANSFER EFFICIENCY = 93°

Fig. 7.4. PHASE ERROR BUDGET FOR THE SPS SUBSYSTEMS.

-70-

loop and (2) the carrier tracking loop. The rms phase error in addition to the phase of the output of the carrier tracking loop is 3.05^o. This assumes a 3° jitter due to the imperfections of VCO and the remaining phase jitter is due to the carrier phase tracking loop. Here we have assumed that the code tracking loop was locked, i.e., perfect despreading operation is obtained. Figure 7.3 shows this.

Next in addition to the phase error (jitter) comes from the reference phase distribution system. We will not dwell too much on the subject here because this was covered in details in Chapter 4. As the table in Chapter 4 shows, the allowable total rms error at the end of the phase distribution tree is 7.5^o which includes all major sources of error in the phase distribution system.

The last source of phase error in the spread spectrum receiver is the power amplifier. As one can see from the figure the maximum allowable phase error (jitter) is 5°. From the power transfer studies we know that the phase jitter in the phase of the radiated wave has to be held down below 10°. The above numbers for phase jitters for various sources when combined together in rms way yields a phase jitter smaller than 10°.

There is one more source of phase jitter which is not depicted in the figure and that is the ionospheric scintillation of the pilot wave as it proceeds towards the spacetenna from the rectenna center. This topic was covered in Chapter 3 and the phase jitter due to this source was determined to be 2°. Thus when rms together with the 10°, does not deviate appreciably from 10°.

Figure 7.4 table indicates the phase error (jitter) budget for the entire SPS system starting from the pilot transmitter to the power beam

Fig. 7.5. KEY BANDWIDTHS AND PHASE JITTERS OF SUBSYSTEMS OF THE SPS.

- INPUT SNR = 96.0 dB (WITH 20 MHz BANDWIDTH OF THE RF FILTER)
- CODING GAIN = 20 dB
- INPUT SNR TO CARRIER TRACKING LOOP AFTER DESPREADING 48 dB

S = -34.5 dBM   S=-34.5dBm
N = 61.5 dBm   N=2dBm

RF FRONT END
B_{3dB}=20MHz

CODE TRACKING LOOP:

B_{IF} = 6.5kHz

$1 \text{kHz} \leq F_d \leq 2\text{kHz}$

$10 \text{ Hz} < B_L < 50$ Hz

$0.1 \text{chip} \leq \sigma_\tau \leq 0.15$ chip

CARRIER TRACKING LOOP:

S=-40dBm
N=-88dBm

$10 \text{Hz} < B_L \leq 1000 \text{Hz}$

$0.5° \leq \sigma_\phi° < 3°$

POWER AMPLIFIER STABILIZATION LOOP:

B_L	σ_ϕ
0.5 kHz	5°
10 kHz	0.1°

DOWNLINK POWER BEAM

HIGH PASS FILTER

REFERENCE SIGNAL FROM MSRTS

$0° \leq \sigma_\phi \leq 7.5°$

OUTPUT POWER BEAM

$7.5° \leq \sigma_\phi \leq 9.5°$

LinCom

reaching the rectenna. The pilot VCO is allowed 1° jitter this is because there is only one transmitter and hence the oscillator is expected to be relatively free of jitter or drift. Each oscillator on board SPS is allowed 3° of phase jitter. The table gives the total allowable rms phase jitter for each subsystem in the SPS system including the pilot transmitter and the ionosphere. Each subsystem is subdivided into components and their respective addition to the phase jitter. On adding all the phase jitters in the root mean square sense one gets the total rms phase jitter of the entire SPS system. This is the most important quantity for it largely determines the efficiency of the SPS system.

Figure 7.5 shows the important quantities of the subsystems. The RF front end has a 3 dB bandwidth of 20 MHz which will reduce the noise level by about 60 dB in that bandwidth output of the RF front end feeds the code tracking loop which has the two arm filters in the τ-dither loop of 3 dB bandwidth = 3 kHz and the code loop bandwidth of 10 Hz which produces an error of less than one percent of the chip time in tracking the code. After despreading the SNR is about 48 dB. The despread signal then is fed to the carrier tracking loop. This loop is deemed to have a loop bandwidth of 10 Hz and assuming 3° VCO phase noise, the total phase noise output of the carrier tracking loop is 3.05^o. The last box shows the effect of the loop bandwidth on the phase jitter. The bandwidth for the loop is selected to be 10 kHz giving the phase jitter to be 0.1^o.

This takes care of the electrical imperfections (jitters). The following paragraph briefly mentions the effect of the electrical system imperfection on the efficiency.

Fig. 7.6. SPS POWER TRANSFER EFFICIENCY.

CURRENT TAPER = 10 dB
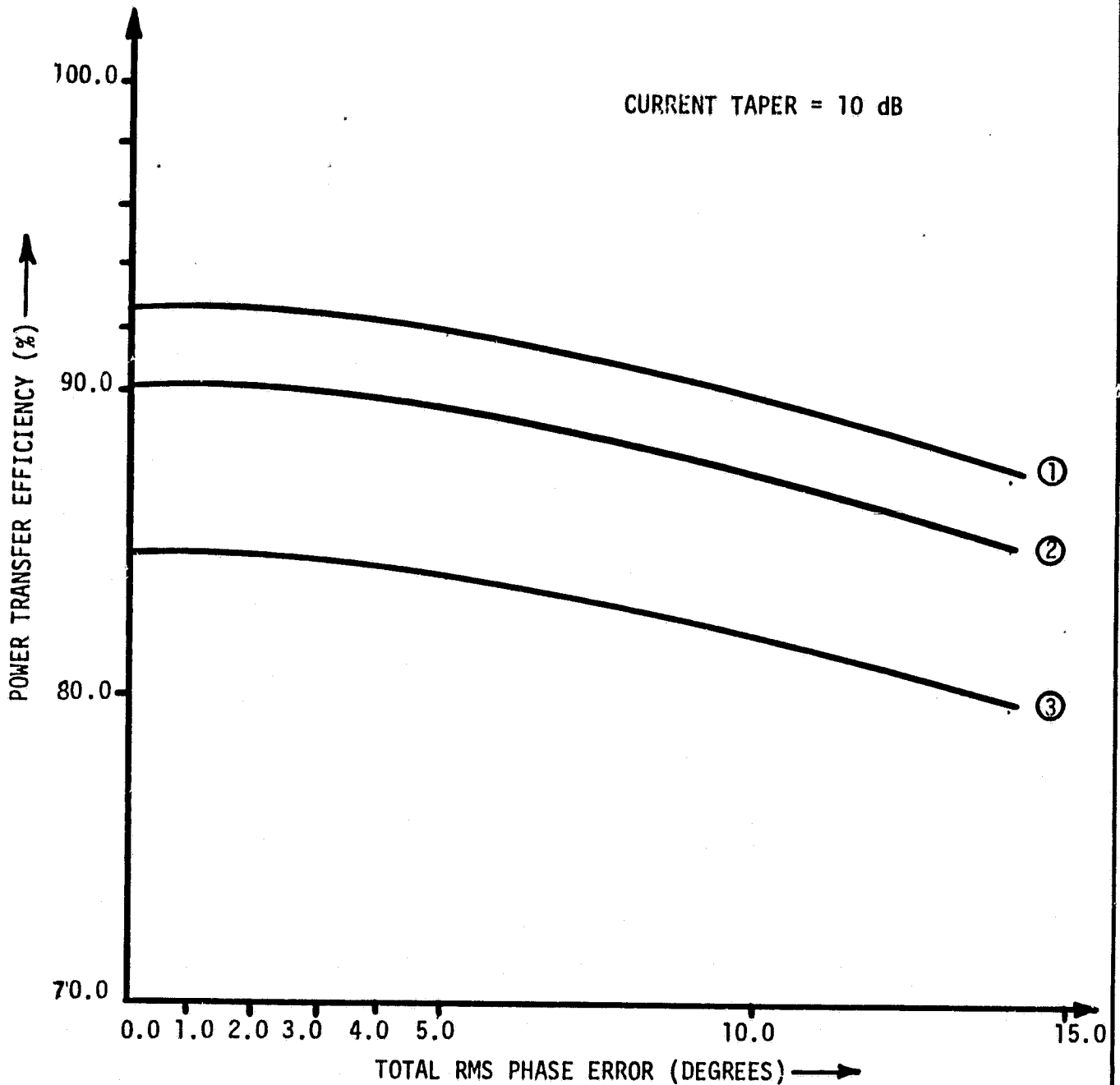
LEGEND

① MECHANICAL POINTING ERROR (MPE) = 0, LOCATION JITTERS (LJ) = 0
  JITTER ON MECHANICAL POINTING = 0

② MPE = 10', LJ = 0, JITTER ON MPE = 2'

③ MPE = 10', LJ = 2% of λ, JITTER ON MPE = 2'

80 0083

In a previous section the power transfer efficiency was defined. That definition is used to generate results given below. The computer program evaluates the received power as given above, i.e., $\phi\epsilon(0,2\pi)$ and $\theta\epsilon(0,0.464')$. The total radiated power is computed in two parts. For the following results, the first part integrated the anisotropic part of the power pattern over the main lobe and 5 side lobes, i.e. the whole space is approximated by $\phi\epsilon(0,2\pi)$ and $\theta\epsilon(0,$ mainlobe + 5 sidelobes). The loss of power resulting by not considering all the side lobes of the pattern is taken care of by multiplying a correction factor. The second part computed the power radiated by the isotropic part of the power pattern. The addition of the two parts produced the total radiated power. The ratio of received power and the total radiated power produced the power transfer efficiency. The systems jitters are the inputs to the program and thus it is possible to investigate the effects of each of the jitters on the power transfer efficiency.

The set of curves shown in Figure 7.6 are indicative of the effect of total phase error (jitter) added by the entire phase control system on the power transfer efficiency of the SPS. This phase error includes contributions from all the sources described above such as the code tracking loop, the carrier tracking loop, the power amplifier, etc. The parameters of the curve being the input from the mechanical system of the SPS, mainly the location jitter of transmitting and receiving elements of the antenna and the mechanical pointing errors and jitters of the subarrays. The first curve in the set is for a mechanically perfect system. From this curve we see that to have a power transfer efficiency of the SPS above 90%, the total rms phase error cannot be allowed to be more than 10°. The rest of the curves are as a result of

CURRENT TAPER = 10 dB

MECHANICAL POINTING ERROR (MPE) = 0

JITTER ON MECHANICAL POINTING =0

LOCATION JITTER = 0
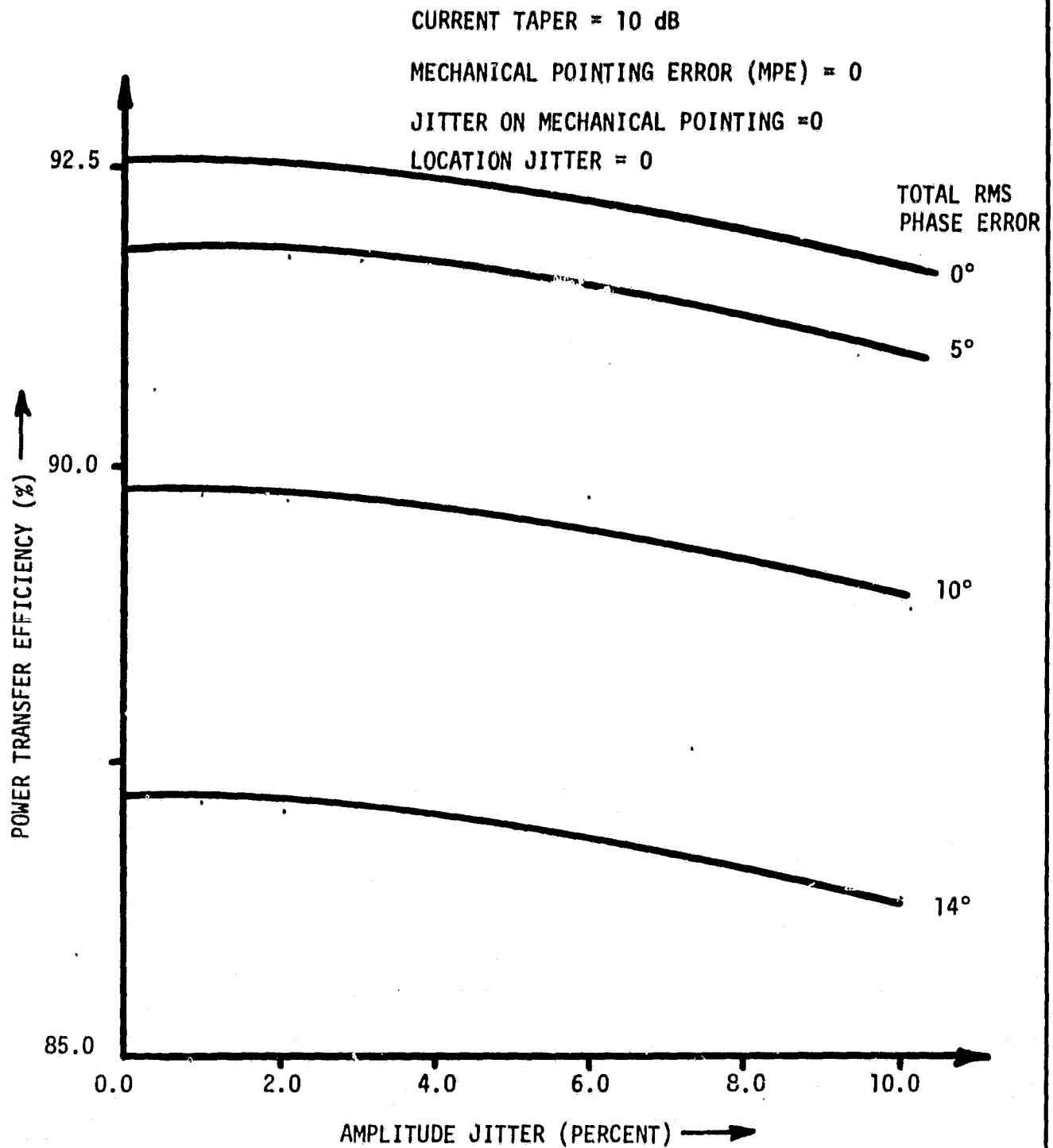
TOTAL RMS
PHASE ERROR

0°

5°

10°

14°

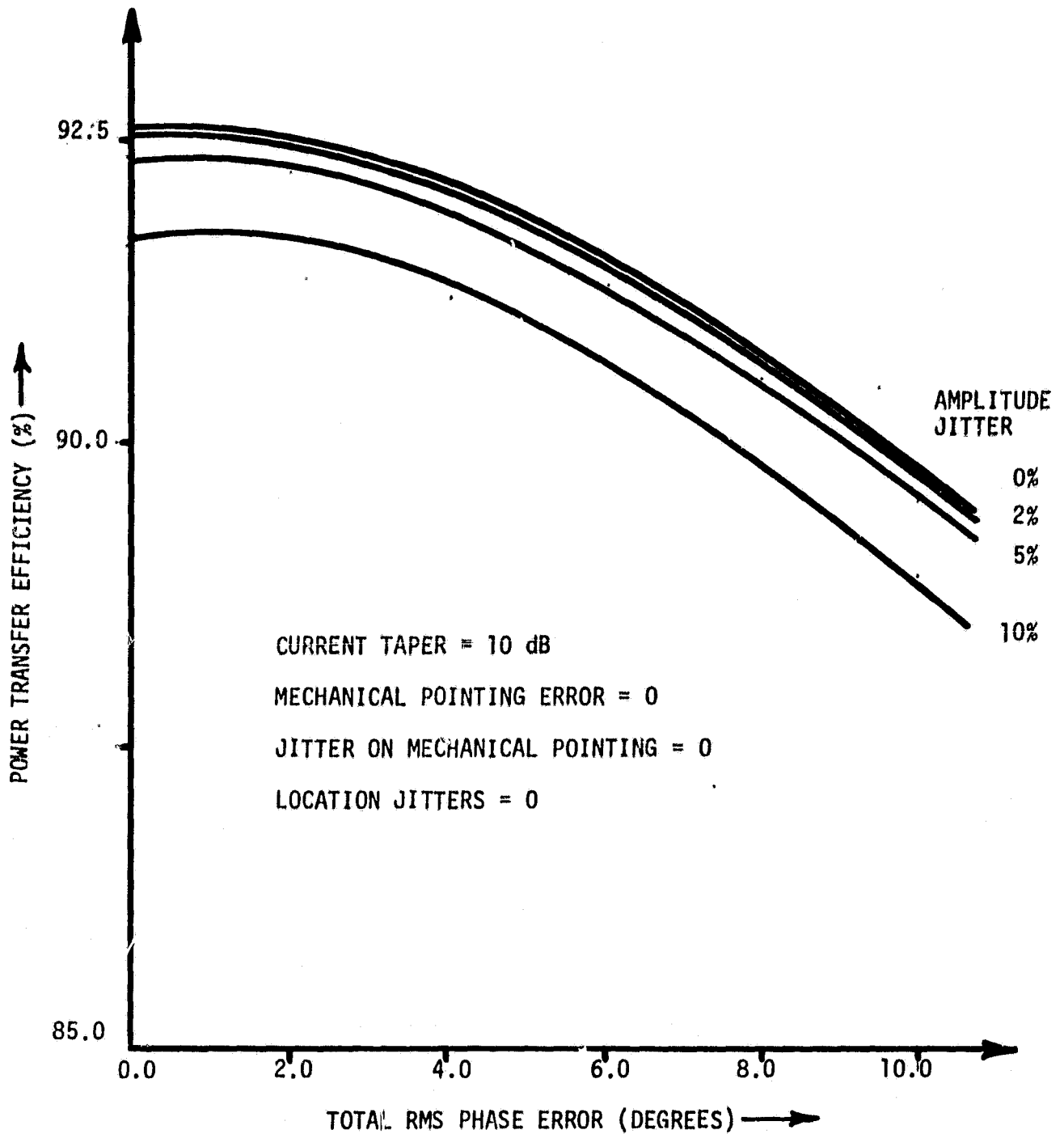Fig. 7.7. EFFECT OF AMPLITUDE JITTER ON SPS POWER TRANSFER EFFICIENCY.

80 0084

Fig. 7.8. EFFECT OF AMPLITUDE JITTER ON POWER TRANSFER
           EFFICIENCY.

mechanical system being imperfect and will be covered in the next section. There is one more type of electrical system imperfection which cannot be classified as a phase jitter and that is the amplitude jitter produced by the high power amplifier (klystron tube). The set of curves in Figure 7.7 show the effect of amplitude jitter on the power transfer efficiency of the SPS.

The set of curves in Figure 7.7 is drawn form a perfect mechanical system, i.e., the mechanical system errors and the associated jitters are held to zero. The power transfer is plotted against the current amplitude jitter while the total rms phase error introduced by the entire phase control system is the parameter. The current amplitude jitter on the x axis is measured in terms of percent of the nominal value of the current amplitude. As can be seen from the figure, for an amplitude jitter of 5%, the power transfer efficiency of the mechanically perfect spacetenna with the current phase jitter of 0° is 92.3%. This value drops to 91.63 or the total phase error of 5° and to 89.57% for a total phase error of 10°. Fig. 7.8 is plot for a mechanically perfect system with power transfer efficiency versus the total accumulated phase error due to the phase control system.
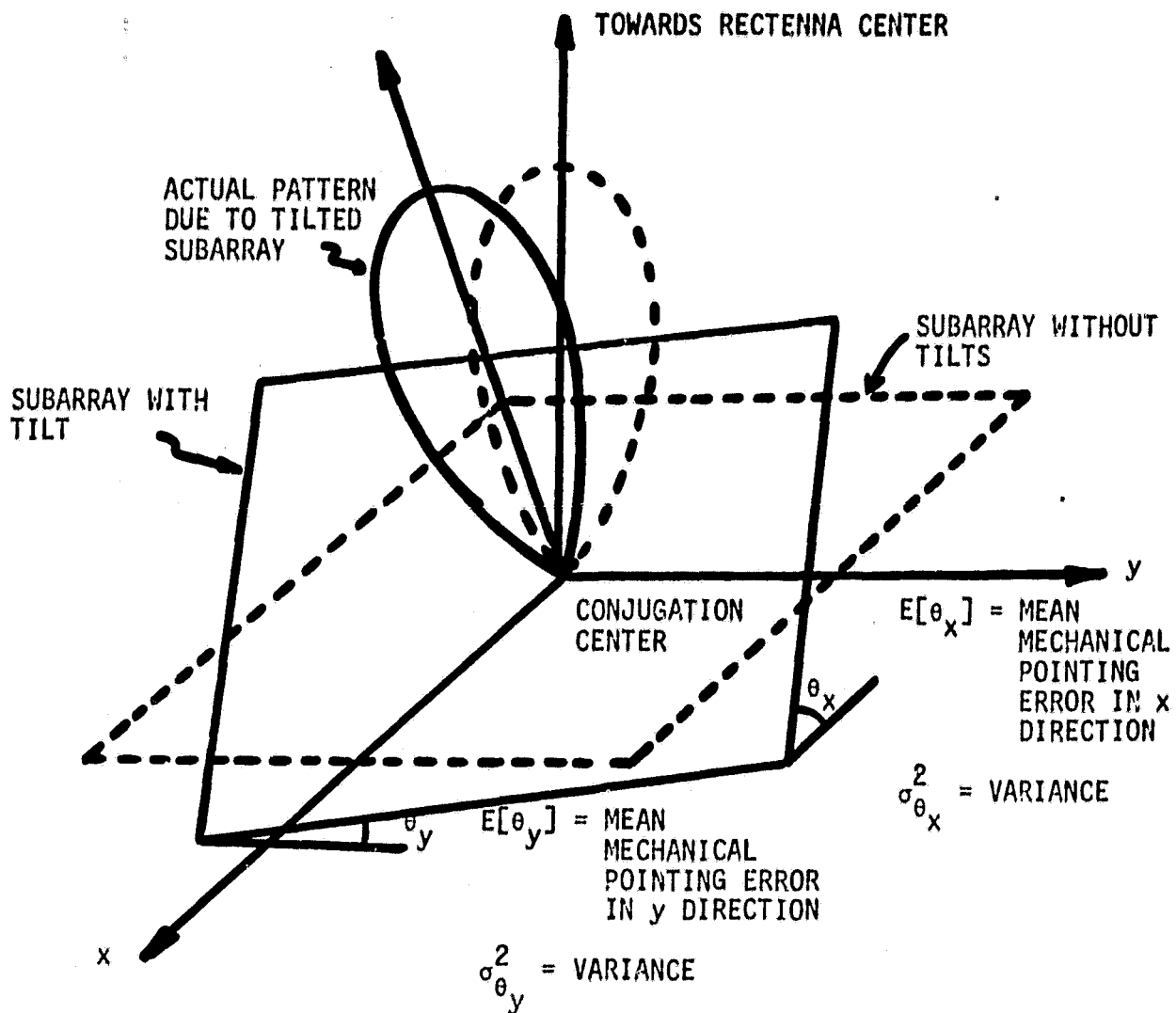
7.2 Mechanical System Imperfections and Their Effects on the Power Transfer Efficiency

This topic has been dealt within great detail in our previous report hence we will dwell upon it only briefly.

Errors due to mechanical system imperfections:

1) Subarray Tilts (Mechanical Pointing Error)

2) Subarray Tilt Jitters (Spatial Jitters of Subarrays)

3) Radiation Element Location Jitters

4) Pilot Receiving Element Location Jitters

Fig. 7.9. EFFECTS OF SUBARRAY MEAN TILTS AND JITTER

TOWARDS RECTENNA CENTER

ACTUAL PATTERN DUE TO TILTED SUBARRAY

SUBARRAY WITHOUT TILTS

SUBARRAY WITH TILT

CONJUGATION CENTER

$E[\theta_x]$ = MEAN MECHANICAL POINTING ERROR IN x DIRECTION

$\sigma^2_{\theta_x}$ = VARIANCE

$E[\theta_y]$ = MEAN MECHANICAL POINTING ERROR IN y DIRECTION

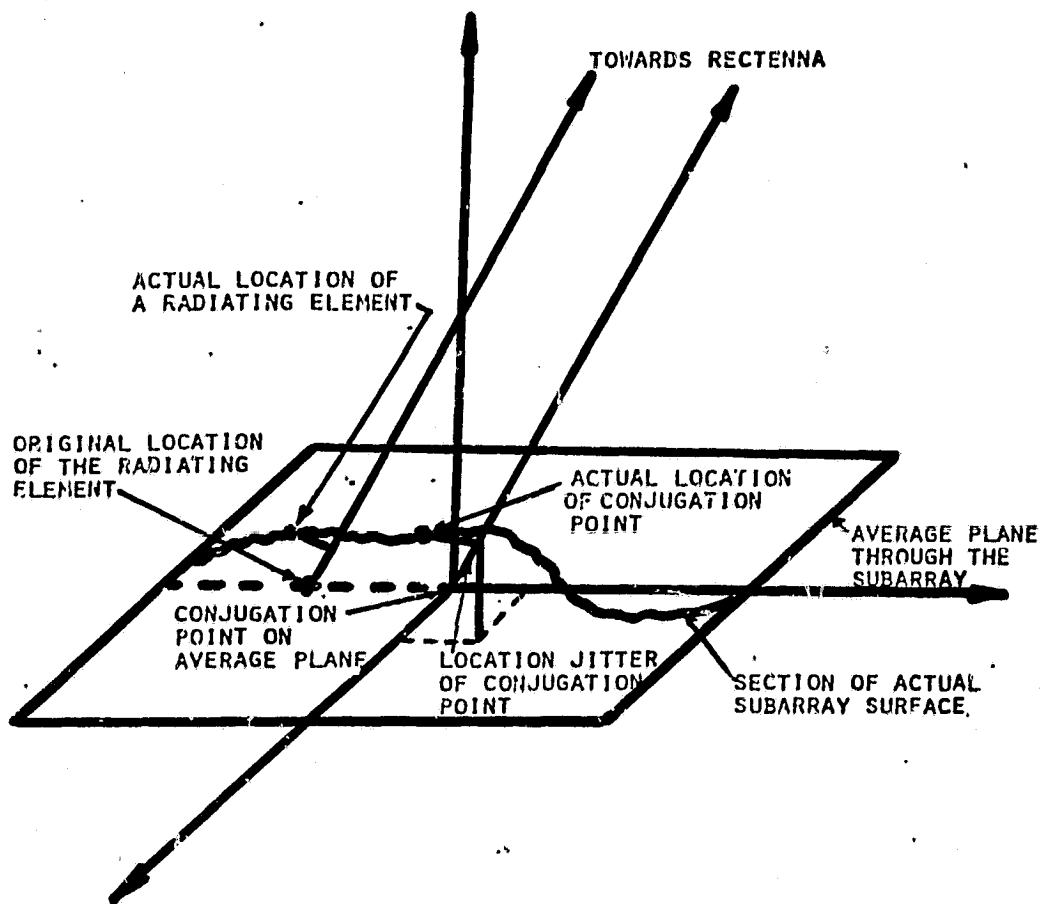$\sigma^2_{\theta_y}$ = VARIANCE

LinCom

Fig. 7.10. JITTERS ADDED DUE TO LOCATION UNCERTAINTY OF
RADIATING AND CONJUGATION POINTS.

The last two errors come from the mechanical constructional faults of the system. Figure 7.9 illustrates the mechanical imperfection introduced due to the subarray tilts and jitter while Figure 7.10 shows the mechanical constructional defects combined with the irregular temperature expansion effects which moves the actual desired location of the radiating element (slot) and the receiving element (the conjugator). It should be noted that even though the antenna is retrodirective in nature, the error introduced due to the mechanical defect is not cancelled by the retrodirective operation. This is so because there is only one conjugator feeding several radiators which are spatially separate from the conjugator location. The second curve in Figure 7.6 helps to depict the influence of the mechanical pointing error (it is assumed to be 10' with a jitter of 2') the location jitters are zero in this case. As can be seen from the figure for a total phase error of 10^0 the power transfer efficiency of the spacetenna drops down to 87.3% and when the location jitters of 2% of lambda is added for the transmiting and receiving elements, this number drops down to 82.0%. One may notice from these curves that the power transfer efficiency of the perfect system is about 92.6%. The prime reason for this being that the rectenna intercepts only a part of the mainlobe, i.e., the power in the part of the mainlobe not intercepted by the rectenna and the power in side lobes is lost. This is significant because at the edge of the rectenna the power density is only about 14 dB lower than the power density at the center of the rectenna.

The curves in Fig. 7.11 and Fig. 7.12 are for the investigation of effects of location jitters on the power transfer efficiency. Fig. 7.11 is drawn for the perfect electrical system, i.e. no phsae errors and no

CURRENT TAPER = 10 dB

MECHANICAL POINTING ERROR = 0

JITTER ON MECHANICAL POINTING = 0

LOCATION JITTER ON RECEIVING ELEMENT = 0

PHASE JITTER = 0

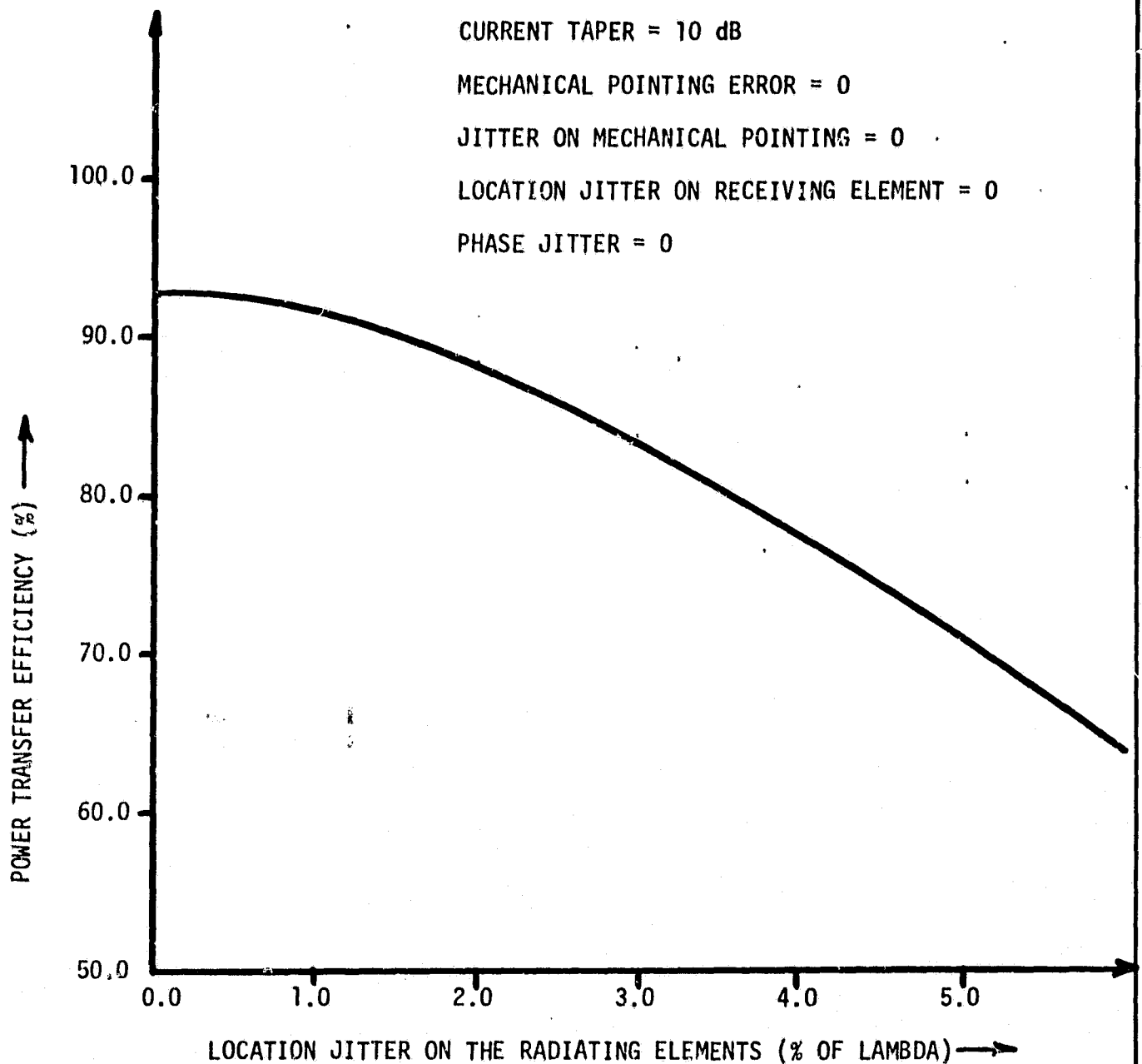LOCATION JITTER ON THE RADIATING ELEMENTS (% OF LAMBDA)———➤

Fig. 7.11. EFFECT OF LOCATION JITTER ON SPS POWER TRANSFER EFFICIENCY.

80 0.086

CURRENT TAPER = 10 dB

MECHANICAL POINTING ERROR = 0

JITTER ON MECHANICAL POINTING = 0

LOCATION JITTER ON RADIATING ELEMENTS = 0
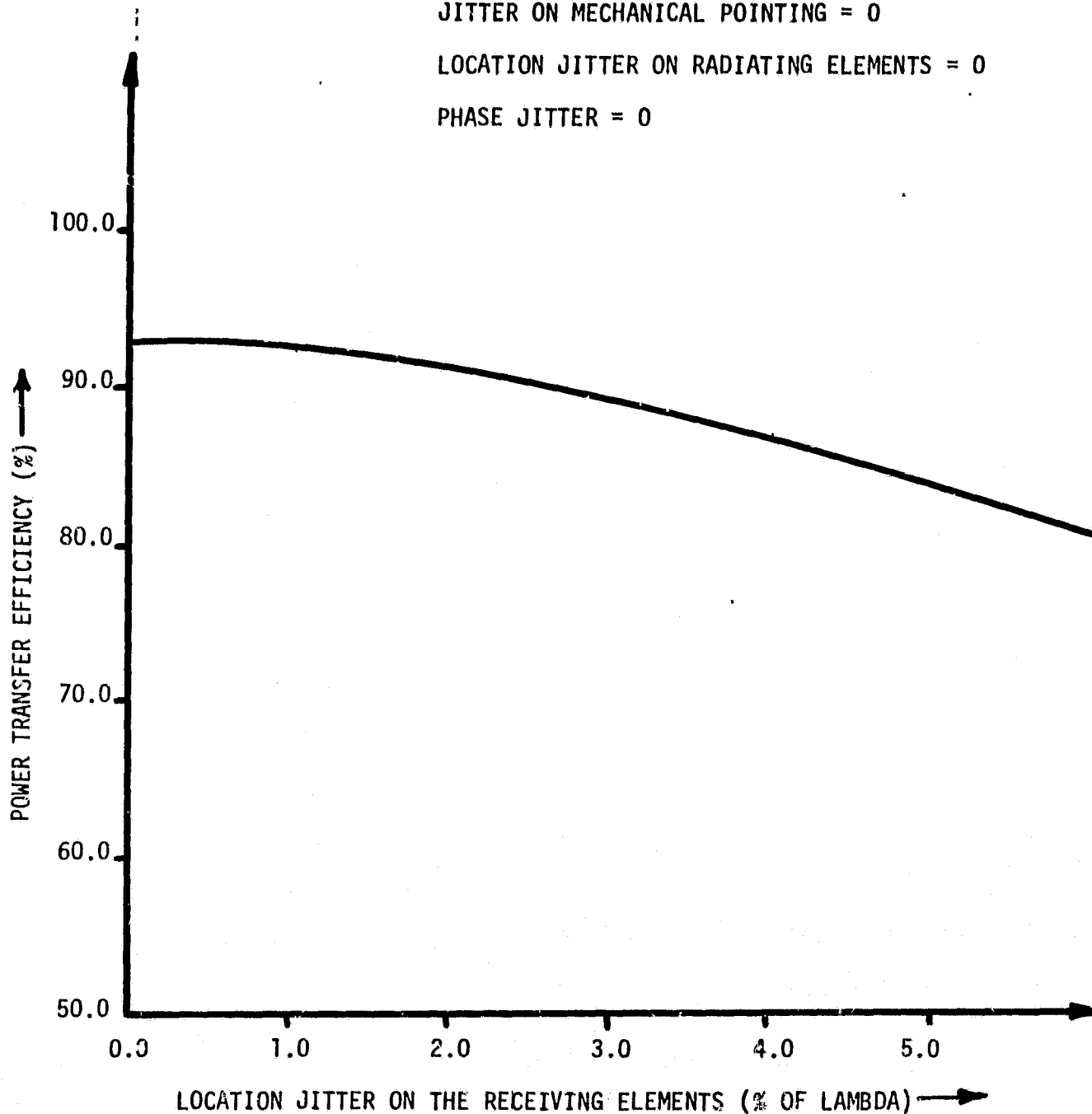
PHASE JITTER = 0

Fig. 7.12. EFFECT OF LOCATION JITTER ON SPS POWER TRANSFER EFFICIENCY.

80 0087

amplitude jitter also the location jitter of the receiving elements is held to zero. As can be seen from the figure, the degradation of efficiency is rapid. For a location jitter on each radiating element to be 2% λ (in the direction of line joining the element and the center of rectenna) the power transfer efficiency drops to 88.3%. As a comparison, the Fig. 7.6 shows that for a phase error of 7° (2% λ = 7.2^o) the efficiency is down to 91.2%. Fig. 7.12 is drawn for the perfect electrical system and the location jitter on the radiating elements held to zero. It is noticeable that the effect produced by location jitters on the receiving (conjugating) elements is comparable to the effect produced by the phase error. This is true because both these effects enter into the transmission system at the same physical point, i.e., the center of the subarray. One can also say that the location jitter on the receiving elements produce less severe effect on the radiating elements. These two curves can be used to determine the allowable mechanical tolerances for the construction of the spacetenna.

It should be noted that all the power transfer efficiency curves were obtained for the SPS system at a radial distance of 37,000 Km from the rectenna center. Should this distance change, the power transfer efficiency would change also. As an example, if the height of SPS system is reduced to 36,000 km, there would be a proportional increase in the power transfer efficiency as seen below. Figure 7.13 is a plot of power transfer efficiency versus the total rms phase error for a mechanically perfect spacetenna with 0 feed current amplitude jitter. The power transfer efficiency for a 0 rms phase error is about 93.5% as compared to 92.6% for the SPS at 37,000 km height. The main reason for the increase in the power transfer efficiency is that from the hieght of
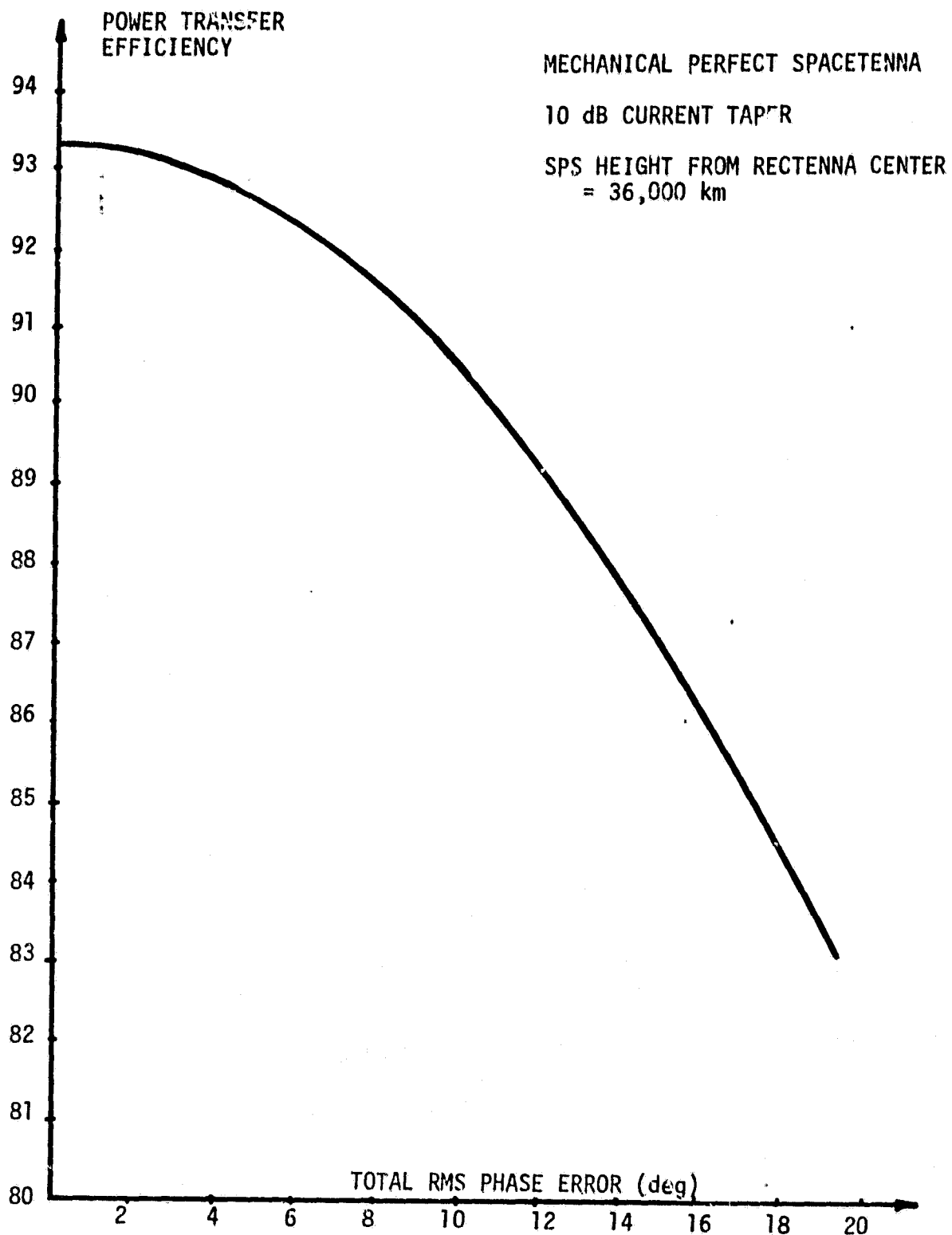
Fig. 7.13. SPS Power Transfer Efficiency vs the Total rms Phase Error.

36,000 km, more of the main lobe of the antenna pattern is intercepted by the rectenna thus reducing the power loss.

8.0 SPS SYSTEM PARAMETER VALUES AND PERFORMANCE

The following pages show design parameter values and the associated performance values of the subsystems of the SPS.

Pilot Transmitter

EIRP	=	93.3 dBW
Maximum Pilot Phase Jitter due to VCO Instabilities	=	3^0
PN Chip Rate	=	10 MHz
Code Separation	=	after 10,000 bits

Ionospherics

Maximum Pilot Phase Jitter During its Passage through Ionosphere	=	3^0

MSRTS Reference Phase Distribution System

Baseline Tree Structure Branching	=	16x16x16x25
Pilot Receiver VCO Jitter (Master Jitter)	=	3^0
Phase Errors due to the Power Splitters in the Phase Distribution Tree	=	6^0
Phase Jitter of the VCO in the Phase Distribution Tree	=	2.5^0
Maximum Allowable Uncompensated Delay Error	=	2.5^0
Total RMS Phase Distribution System Jitter	=	7.5^0

Front End of the MPTX System

Arm Filter Selction	=	6 pole Butterworth filter
Filter Null	=	60 dB
3 dB Bandwidth of the Front End Filter	=	20 MHz

Half 3 dB Bandwidth of the
Created by the Front End Filter = 30 MHz

Center Frequency of the Low Pass
Equivalent of the Front End Filter = 40 MHz

Noise Reduction due to the
Front End Filter = 60 dB

Coherent Noise Coupling Coefficient = 0.01

Noncoherent Noise Coupling Coefficient = 0.01

Carrier Tracking Loop

Carrier Tracking Loop Bandwidth = 10 Hz

Carrier Trackingn Loop VCO Phase
Jitter = 3^0

Carrier Tracking Loop Phase Jitter due
to Coherent and Noncoherent Noises = 0.5^0

Total RMS Phase Error of the Carrier
Tracking Loop = 3.05^0

Code Tracking Loop

Arm Filter 3 dB Bandwith = 3 kHz

Code Loop Bandwidth = 10 Hz

Dither Frequency = 1 kHz

Loop Filiter 3 dB Bandwidth = 3 kHz

Code Tracking Loop Error = < 1% of chip time

Power Amplifier Loop

3 dB Bandwidth of the Loop Filter = $1 \text{ kHz} \leq B_L \leq 10 \text{ kHz}$

Phase Jitter of the VCO in the Loop = 3^0

Phase Jitter of the Power Amplifier = $0.5 \leq \sigma_\phi \leq 5^0$

Total RMS Phase Jitter (maximum) = $3.05^0 \leq \sigma_\phi \leq 5.16^0$

SPS System

Total Phase Jitter at the
Radiating Point $\quad\quad\quad\quad\quad\quad = 10.5^{\mathrm{o}}$

Power Transfer Efficiency of
the Solar Power Satellite $\quad\quad\quad = 93.5\%$

REFERENCES

1. Lindsey, W. C., "A Solar Power Satellite Transmission System Incorporating Automatic Beam Forming, Steering and Phase Control," prepared for NASA/JSC, June, 1978, LinCom Corporation, Pasadena, CA.

2. Hansen, R. C., Microwave Scanning Antennas, Part II and Part III, Academic Press, New York, 1966.

3. Chernoff, Ralph C., "Large Active Retrodirective Arrays for Space Applications," Jet Propulsion Laboratory Report, October 31, 1977.

4. Lindsey, W. C., Kantak, A. V., Chie, C. M., Booth, R. W. D., "SPS Phase Control System Performance via Analytical Simulation," prepared for NASA/JSC, March 1979.

5. Simon, M. K., "Noncoherent Pseudonoise Code Tracking Performance of Spread Spectrum Receivers," IEEE Transactions on Communications, Vol. COM-25, No. 3, March 1977, pp. 327-344.

6. Gordon, W. E., and Duncan, L. M., "Ionosphere/Microwave Beam Interaction Study," prepared for NASA by William Marsh Rice University, July 1978.